LBNL-41797

ERNEST ORLANDO LAWRENCE BERKELEY NATIONAL LABORATORY

High-Resolution Structural Studies of Ultra-Thin Magnetic, Transition Metal Overlayers and Two-Dimensional Transition Metal Oxides using Synchrotron Radiation

Scot A. Kellar

Advanced Light Source Division

May 1997

Ph.D. Thesis

REFERENCE COPY
Does Not
Circulate
Bldg. 50 Library - Ref.
Lawrence Berkeley National Laboratory
LBNL-41797
Copy 1

DISCLAIMER

This document was prepared as an account of work sponsored by the United States Government. While this document is believed to contain correct information, neither the United States Government nor any agency thereof, nor the Regents of the University of California, nor any of their employees, makes any warranty, express or implied, or assumes any legal responsibility for the accuracy, completeness, or usefulness of any information, apparatus, product, or process disclosed, or represents that its use would not infringe privately owned rights. Reference herein to any specific commercial product, process, or service by its trade name, trademark, manufacturer, or otherwise, does not necessarily constitute or imply its endorsement, recommendation, or favoring by the United States Government or any agency thereof, or the Regents of the University of California. The views and opinions of authors expressed herein do not necessarily state or reflect those of the United States Government or any agency thereof or the Regents of the University of California.

LBNL-41797

High-Resolution Structural Studies of Ultra-Thin Magnetic, Transition Metal Overlayers and Two-Dimensional Transition Metal Oxides using Synchrotron Radiation

Scot Arthur Kellar
Ph.D. Thesis

Department of Chemistry
University of California, Berkeley

and

Advanced Light Source Division
Ernest Orlando Lawrence Berkeley National Laboratory
University of California
Berkeley, CA 94720

May 1997

This work was supported by the Director, Office of Energy Research, Office of Basic Energy Sciences, Chemical Sciences Division, of the U.S. Department of Energy under Contract No. DE-AC03-76SF00098.

LSBL- 457 EC

Light Source Note:
Author(s) Initials SAK
Group Leader's initials DAP 4/27/98
Date
Date

ABSTRACT

HIGH-RESOLUTION STRUCTURAL STUDIES OF ULTRA-THIN MAGNETIC, TRANSITION METAL OVERLAYERS AND TWO-DIMENSIONAL TRANSITION METAL OXIDES USING SYNCHROTRON RADIATION

by

Scot Arthur Kellar

Doctor of Philosophy in Chemistry

University of California, Berkeley

Professor David A. Shirley, Co-Chair

Professor Armand P. Alivisatos, Co-Chair

This thesis reports the surface-structure determination of three, ultra-thin magnetic transition-metal films, Fe/Au(100), Mn/Ni(100), and Mn/Cu(100) using Angle-Resolved Photoemission Extended Fine Structure (ARPEFS) and photoelectron holography. These structural studies are the first to use non-s initial states in the ARPEFS procedure. This thesis also reports an ARPEFS surface-structure determination of a two-dimensional transition-metal oxide, [(1x1)O/W(110)]x12.

We have analyzed the ARPFES signal from the Au $4f_{7/5}$ core level of the Au(1 ML)/Fe(15 ML)/Au(100) system. Our analysis shows that the Fe grows layer by layer with one monolayer of gold, acting as a surfactant, remaining on top of the growing Fe layers. These surface gold atoms sit in the four-fold hollow site, 1.67 ± 0.02 Å above the iron surface. The grown Fe layer is very much like the bulk, bcc iron, with an interlayer spacing of 1.43 ± 0.03 Å.

Analysis of the Mn 3p ARPEFS signals from c(2x2)Mn/Ni(100) and c(2x2)Mn/Cu(100) shows that the Mn forms highly corrugated surface alloys. The corrugation of the Mn/Ni(100) and Mn/Cu(100) systems are 0.24 ± 0.02 Å and 0.30 ± 0.04 Å

respectively. In both cases the Mn is sticking above the plane of the surface substrate atoms. For the Mn/Ni(100) system the first layer Ni is contracted 4% from the bulk value. The Mn/Cu(100) system shows bulk spacing for the substrate Cu. Photoelectron holography shows that the Mn/Ni interface is very abrupt with very little Mn leaking into the second layer, while the Mn/Cu(100) case has a significant amount of Mn leaking into the second layer.

A new, five-element electrostatic electron lens was developed for hemispherical electron-energy analyzers. This lens system can be operated at constant transverse or constants angular magnification, and has been optimized for use with the very small photon-spot sizes. Improvements to the hemispherical electron-energy analyzer are also discussed.

High-Resolution Structural Studies of Ultra-Thin Magnetic, Transition Metal Overlayers and Two-Dimensional Transition Metal Oxides using Synchrotron Radiation

by

Scot Arthur Kellar

B.S. Physics (University of Oregon) 1988
B.S. Chemistry (University of Oregon) 1988

A dissertation submitted in partial satisfaction
of the requirements for the degree of
Doctor of Philosophy

in

Chemistry

in the

GRADUATE DIVISION

of the

UNIVERSITY OF CALIFORNIA, BERKELEY

Committe in charge:

Professor David A. Shirley, Co-Chair
Professor Armand P. Alivasatos, Co-Chair
Professor Gabor A. Somorjai
Professor Ronald Gronsky
Professor Zahid Hussain

Spring, 1997

For Gramps, I wish he were still here to see it.

ACKNOWLEDGEMENTS

It's hard for me to believe that this time is actually here. So many times when I couldn't really imagine that I would finally finish, I thought about writing 'my acknowledgements'. It's the one part of most other theses that I always read. Now that it is my turn, I'm at a bit of a loss. I'm at a loss because even more than most dissertations this work would never be possible without the help of so many people. First I should acknowledge my advisor, Dave Shirley. I've learned a lot about science from Dave in the last few months, what questions are really important and how to scrutinize a mass of information for the crucial bits. Dave has such a keen mind and is such an accomplished scientist, I wish he could have been around more during my time in graduate school. I feel I could have been a much better scientist for the experience.

Zahid Hussain was around for all my graduate career. What I feel I may have missed with Dave being gone is more than made up by the honor of working with Zahid during that time. Zahid is one of the finest people I've ever known. He tried to teach me many things other than science. Though it may not seem like it I did listen. Thank you Zahid.

Eddie Moler and Tony Huff were the other parts of Zahid's little army and my constant companions while we built the beamline and during all these experiments . We shared lots of 'coffee' and many donuts—too many sometimes! Their help was invaluable, though I will never forgive Tony for breaking the police lights!

Most of this thesis would not be possible without the excellent work done by Yufeng Chen on the scattering code. He spent a lot of time explaining it to me. His patience is only matched by Zahid's.

Xin Zhou helped with the tungsten oxide data collection and Ramon Ynzunza helped with the sample preparation, not to mention his Herculean effort to make the Scienta system work.

Jonathan Denlinger and Eli Rotenberg took the data on the Mn surface alloys and suffered my many questions about it.

Javier Palomares gave me the idea for the excellent iron evaporator.

Pat McKean was indispensable to the moving and reconstruction of the beamline from Stanford to LBL. Bob Gassaway and Randy Candilario ran the wiring for the beamlines and did numerous other wiring jobs for us above the call of duty.

Ted Lauritzen originally designed the important bits of the beamline and Curtis Cummings made all the pieces fit together when we moved the beamline from Stanford to LBL. The surveying crew helped to put the beamline where it was supposed to go.

Wayne-O and Dennis Hull are the maestros with the forklifts that took our chambers down and put them back up and took them down and put them back up.... you get the idea. Charlie Knopf ran all the waterlines and provided plenty of humor.

The vacuum group, especially Bruce Rude, was always there to help with hardware, and baking supplies, just about whatever we need.

Cheryl, Orland and the rest of the control room staff which runs the ALS are obviously instrumental in this work.

The EM shop taught me about three-phase power and wiring, especially Serge Rogoff. Jim Bishop and Mel Photos were always willing to help fix electrical problems (They are especially important for keeping the ring running). Jim also runs what I call 'Jim's Diner' which many nights kept me from a hypoglycemic stupor, and Mel tells the best stories on the hill. Many nights he kept me from terminal boredom. I hope he makes a full recovery and gets back to work. The place isn't the same without him, and he owes me a tour of the Bevalac.

Joe Katz and Jure Zaninovich taught me everything I know about electronics, which may not be much, but they didn't have much to work with. They are also very patient people. Mike Press taught me to clean the soldering iron with my tongue. Mike is a dangerous person.

Neal Hartman, postponed his graduation, I don't know how many times, to make technical drawings for me at the last minute. I'll miss him now that he has to work with the real engineers, but I wish he would clean-up his office. And I really wish he would graduate SOON. Gregory Andronaco taught me to use ME10 and ME30, though I'm not sure that this was a blessing. Greg also helped with beamline and instrument design.

If this work looks somewhat professionally done, the credit is due to Greg Vierra, who explained the intricacies of typesetting to me.

There are many others, Jeff Cruzan, C.C. Morton, Chris Mundy, Eric Peterson, Dawn Eggert and Nancy Schmaus, John Sterling, John Nangle, Karl Anderson, the

whole Gutmann clan: I would have finished this thesis and graduated had they not been around, but what would have been the point?

The end would be worthless if the journey had not been worthwhile. They made the journey very worthwhile, actually more worthwhile than the degree.

I would not have graduated, however, had it not been for the Sierra. The Sierra Nevada are the reason I stayed in Grad school. My love–hate relationship with Berkeley is that I hate Berkeley, but I love the Sierra. To see its further destruction physically pains me, and gives me possibly the direction for life after graduate school. While I have never been to the Florida Keys, my favorite Calypso poet sums up my feelings about the disrespectful destruction of what I feel is my home.

> ...And mobile homes are smootherin' my Keys
> I hate those bastards so much.
> I wish a summer squall would blow them
> All the way up to fantasy land.
> They're ugly and square, they don't belong there
> They looked a lot better as beer cans.
>
> Jimmy Buffet

I'd also like to acknowledge my parents beyond the obvious, like without them none of this would have come to be. Dad started me doing math problems in the car on the way to play squash when I was very little. The perfect balance between mind and body. Oat put me through college. I hope in the future, his generous investment works out as well for him as it did for me. More importantly, Oat propped up my sister and sent her on her way with a regained sense of self-respect. For that I am truly grateful. Mom always thinks I'll win the Nobel Prize, and though I've tried to explain to her that I never will, it's still nice to know that somewhere, someone thinks that I am the smartest guy around. It is humbling to think about how Mom sacrificed everything for her kids.

I've been married now for nearly seven months, not long compared with the 12 years that Caroline and I dated. Yet, every day I am more aware of how lucky I am to have married my Best Friend, and what a great Best Friend she is. There is no better feeling than coming home to see that big, sweet grin and hear that goofy, "Hi Honey!". Fletcher is simply the Best. I wish we could have three more of him. I still promise we'll live somewhere where you can play in the snow all the time.

... You shall know the night - its space, its light, its music.
You shall see earth sink in darkness and the universe appear.
No roof shall shut you from the presence of the moon.
You shall see mountains rise in the transparent shadow
before dawn.
You shall see - and feel! - first light, and hear a ripple in the
stillness.
You shall enter the living shelter of the forest.
You shall walk where only the wind has walked before.
You shall know immensity, and see continuing
the primeval forces of the world.
You shall know not one small segment but the whole of
life, strange, miraculous, living, dying, changing.
You shall face immortal challenges; you shall dare,
delighting, to pit your skill, courage, and wisdom
against colossal facts.
You shall live lifted up in light;
You shall move among clouds.
You shall see storms arise, and drenched and deafened,
shall exult in them.
You shall top a rise and behold creation.
And you shall need the tongues of angels
to tell what you have seen.
Were all learning lost, all music stilled,
Man, if these resources still remained to him,
could again hear singing in himself
and rebuild anew the habitations of his thought.

. . . Tenderly now
let all men
Turn to the earth . . .

Nancy Newhall
Ansel Adams

Contents

CHAPTER 1
INTRODUCTION

I. General Overview 3
Figure 1. Photoelectron scattering 8
II. Scattering Theory 9
Figure 2.. Ni scattering factors 10
III. Contents 12
References 12

CHAPTER 2
SURFACE STRUCTURE DETERMINATION OF AU(1 ML)/FE(15 ML)/AU(100) USING ANGLE-RESOLVED PHOTOEMISSION EXTENDED FINE STRUCTURE

I. Introduction: 15
II. Experimental 16
Figure 1. Fe 3p peak area *vs.* evaporation time. 17
III. Data analysis 17
Figure 2. A typical photoemission spectrum from the 15 ML Fe/Au(100) system. 18
Figure 3. ARPEFS data from the Au 4f core level for 1ML Au/15ML Fe/Au(100) in the [001] and [011] directions. 19
Figure 4. The mean free paths for iron and gold 20
Figure 5. ARLP-FTs of the ARPEFS [001] data and the [011] data 22
Figure 6. R-factor vs. inner potential and Au-Fe1 interlayer spacing. 24
Figure 7. R-factor vs. inner potential and Fe1-Fe2 interlayer spacing 24
Figure 8. R-factor vs. the interlayer spacing and a parabolic fit 25
IV. Error Analysis 25
V. Conclusion 26
References 26

CHAPTER 3

THE STRUCTURAL DETERMINATION OF MNNI AND MNCU SURFACE ALLOYS USING ANGLE-RESOLVED PHOTOEMISSION EXTENDED FINE STRUCTURE AND PHOTOEMISSION HOLOGRAPHY 31

I. Introduction 31
II. Experimental 32
Figure 1. Top panel: optical layout of Beamline 7.0 at the ALS. Bottom panel: Experimental geometry. 33
III. Data Analysis 34
Figure 2. Photoemission spectra for Ni 3p and Mn 3p 35
Figure 3. Experimental Mn 3p c(k) curves for the [001] and [011] emission directions from c(2x2)Mn/Ni(001) 36
Figure 4. Experimental Mn 3p χ(k) curves for the [001] and [011] emission directions from c(2x2)Mn/Cu(001) 37
Figure 5. Experimental data and fit for the c(2x2) Mn/Cu(001) Mn 3p photoemission peak. 38
Figure 6. Comparison of the χ(k) curves derived from the lineshape and window method 39
IV. Results and Discussion 41
Figure 7. Experimental and calculated holograms for the MnNi and MnCu surface alloys. 42
Figure 8. Electron scattering factors vs. scattering angle for Cu, Mn , and Ni 43
Figure 9. Top panel: Calculation geometry for Mn/Cu(001) surface alloy. Bottom panel: Polar angle scans along the [011] azimuth and the [101] azimuth 44
Figure 10. Calculated peak position of the forward focusing peaks vs the surface corrugation 45
Figure 11. The Mn 3p lineshape from the c(2x2) Mn/Cu(001) sample and from the c(2x2) Mn/Ni(001) 46
Figure 12. Comparison of the MSSW best fit calculations to the [001] emission data for three different adsorption sites. 47
Table I. Best fit parameters and the associated R-factor for the three adsorption sites 48

Figure 14. Atomic model of the c(2x2) Mn/Ni(001) structure determined by the present ARPEFS study. 49
Figure 15. The top two layers of the calculation cluster for c(2x2) Mn/Cu(001) 50
Figure 16. Comparison of the MSSW best fit calculations to the [001] emission data for different adsoption geometries. 51
Figure 17. Comparison of the MSSW best fit calculations to the [011] emission data for different adsoption geometries. 52
Figure 18. Atomic model of the c(2x2) Mn/Cu(001) structure determined by the present ARPEFS study. 53

Figure 19. R-factor vs. the interlayer spacing 53
Figure 20. R-factor vs. the interlayer spacing 55
Figure 21. Experimental and calculated $\chi(k)$ curves for a surface Debye temperature of 375 K, 90% of the bulk Mn value. 57
Figure 22. Surface alloy formation mechanism 59
Conclusion 60
References 71

CHAPTER 4

THE SURFACE STRUCTURE OF (1x1)O/W(110)x12 DETERMINED BY ANGLE-RESOLVED PHOTOEMISSION EXTENDED FINE STRUCTURE

I. Introduction 65
Figure 1. Surface structure of the (1x1) O/W(110) showing possible high-symmetry adsorption sites. 66
II. Experimental 67
Figure 2. Optical layout of Beamline 9.3.2 at the Advanced Light Source in Berkeley. 67
Figure 4. The experimental geometry for the ARPEFS data collection. ... 68
Figure 5. A typical O 1s photoemission spectrum of [O(1x1)/W(110)]x12 70
III. Fourier Analysis 71
IV. Multiple Scattering Calculations 72
Figure 6. ARLP-FT of the experimental $\chi(k)$ curves for the O 1s normal emission and 45° off-normal emission 73
Figure 8. Best-fit calculations to the off-normal emission O 1s $\chi(k)$to the threefold hollow and center sites. 76

Figure 9. R-factor vs. fitted parameter for the O-W1 and W1-W2 interlayer spacing 77
V. Discussion 78
Figure 10. Directions of the hybrid orbitals directed out of the BCC (110) surface according to the model of Altmann, Coulson, and Hume-Rothery. 79
VI. Conclusion 79
References: 80

CHAPTER 5 83
REDESIGN OF THE ARPES LENS SYSTEM AND POWER SUPPLIES 83

I. Introduction 83
II Lens system 84
Figure 1. Schematic of the ARPES electron energy analzyer 86
Figure 2. Trager-Cowan et al. curves used in the parameterization determining the lens voltage ratios 89
Figure 3. The voltage curves for lens elements 2, 3, and 4 at constant linear magnification 90
Figure 4. The voltage on lens element 4 corrections 91
Figure 5. SIMION ray tracing of the old and new lens systems 92
III. Power Supplies 92
Figure 7. Linear Magnification plotted as a function of the overall voltage ratio 94
Figure 9. Schematic layout of the power supply groups and output voltages. 96
Figure 10. New APRES Power supply Tree 97
IV. Analyzer Changes 98
Figure 11. V1 voltage surface 99
Figure 12. Contour and Image plot of the V1 voltage surface 100
V Future Improvements 101
References 102

CHAPTER 6
CONCLUSIONS

I. Summary 105
II. The Present 106
III. Experimental Considerations 107

III. The Future 108

APPENDIX A 111
GOLD POLISHING 111

Now I see the secret of the making of the best persons.
It is to grow in the open air, and to eat and sleep with the earth.

Walt Whitman, Leaves of Grass

CHAPTER 1

INTRODUCTION

This dissertation describes the application of photoelectron diffraction, in its various forms, to determine the local atomic structure of transition-metal overlayers and transition-metal oxides. The transition-metal overlayers of interest in this thesis are those that are predicted to exhibit novel magnetic properties as two dimensional overlayers. The study of these transition-metal overlayers represents an extension of the Angle-Resolved Photoemission Extended Fine Structure (ARPEFS) technique to structural studies using photo-excited electrons from initial states with orbital angular momentum greater than zero. Additionally the metal oxide study is the first ARPEFS study using a chemically shifted core level. This thesis also describes in Chapter 5, instrumental improvements to the electron lens system used with hemispherical electron-energy analyzers, in addition to other improvements to hemispherical analyzers in general.

The first section of the introduction will give a general overview of the electron diffraction technique and some footing for why the information this technique provides is useful. The second section compares the photoelectron diffraction technique to other structural probes and gives a very selective and abbreviated history of its development. The third section describes a simple physical model containing the basic physics of the electron diffraction process.

I. General Overview

As Physical chemists our goal is often to relate form with function. Of the many interesting phenomena associated with condensed matter, Magnetism has enjoyed, of late, a kind of renaissance. This renewed research interest has followed the discovery of a variety of new phenomena associated with artificially made thin-transition-metal films. Among these phenomena are the theoretical prediction of enhanced magnetic moments in ultra-thin films and at surfaces[1], the discovery of perpendicular magnetic anisotropy in layered structures[2, 3], and the discovery of

giant magnetoresistance effects (GMR)[4, 5] and oscillatory exchange coupling[6] in multilayers. These multilayer materials are made by growing alternating thin films of magnetic and 'nonmagnetic' metals. These newly discovered magnetic phenomena are already being incorporated into new consumer products. One example is the spin-valve sensors now being used as magnetic read heads on hard drives. Another example is the use of GMR materials as a non-volatile (the information is stored in magnetic bits which are not affected when power is lost) alternative to semiconductor based direct random access memories (DRAMS)[7].

Many of these interesting materials are layered structures consisting of alternating ultra-thin layers of different metals. These layers range in thickness from less than a monolayer to a few atomic layers. It has already been shown that the two-dimensional nature of these structures affects their physical properties[3]. Additionally the crystal structure of these thin layers can be very different from that of the bulk material, changing the magnetic moments and their preferred bulk orientation[8, 9]. Detailed knowledge of the local atomic structure may be critical to understanding the complex phenomena exhibited by these new materials. While many techniques can probe the atomic structure of the bulk material, the lower concentration of surface and near-surface layers requires a technique that is selectively sensitive to this region. Furthermore, because the magnetic properties of the material are most often the result of a specific element, a technique that can selectively investigate the structure around a selected element and even a specific chemical state of one element is highly desirable. These are the strengths of photoelectron diffraction.

Atomic scale structural determinations of bulk crystals have been routine for some time. X-ray diffraction is the most commonly used for bulk crystalline samples. Extended X-ray absorption fine structure (EXAFS) has also been used in studies of crystalline, as well as non-crystalline, bulk materials. This technique uses the fine structure modulations in the photoabsorption cross section caused by final state interference effects of a photoexcited core electron. Fourier analysis of the fine structure modulations provides information about the radial bond lengths of the nearest neighbor atoms surrounding the adsorbing atom. EXAFS main advantage is that, unlike X-ray diffraction, it has elemental selectivity through the binding energies of the core electrons.

When one is interested in the surface and near-surface region, one must use a technique that is more sensitive to this region than bulk techniques. There are of course many creative solutions to this surface sensitivity problem; I will only briefly describe a few. Two direct methods are scanning tunneling microscopy (STM)[10] and atomic force microscopy (AFM). The STM technique scans an extremely thin needle across surface of a metal or semiconductor. When the tip of the needle is brought very close to the surface, electrons tunnel across the intervening space. Measuring the current between the surface and the needle gives a measure of the distance of the needle from the surface. STM can detect atomic-scale varia-

tions in the height of the surface, but it is limited to studying only conducting or semiconducting surfaces, while AFM is applicable to any surface including, insulators. AFM measures the van der Waals force between the sample surface and an ultra-fine silicon tip mounted on a spring-loaded cantilever. Laser light is focused onto the cantilever and the reflected light is measured by a position sensitive detector which converts cantilever deflection into an electrical signal. As the tip scans over the sample, the variation in the tip deflection produces an image of the surface with sub-nanometer resolution. While Both techniques provide atomic images of the surface layer, neither technique has the ability to identify specific elements or provide much reliable information about distances perpendicular to the surface.

To achieve surface sensitivity, low energy electron diffraction (LEED) and photoelectron diffraction use the limited mean free path of electrons with kinetic energies between approximately 50 eV and 1000 eV. In LEED, a primary electron beam is incident on a surface with long range order and one collects the diffracted electrons. The measured two-dimensional LEED pattern provides direct information about the periodicity and translational symmetry of the surface. More quantitative information, such as bond lengths and adsorption sites, can be obtained by measuring the intensities of the reflected electrons as a function of incident electron kinetic energy, and comparing these intensities to theoretical calculations. While LEED is convenient as an in-laboratory technique it has some drawbacks. The first problem is the radiation damage caused by an intense electron beam. For delicate overlayers, the incident electron beam can damage the surface layer while the measurements are being made. LEED may not be suitable for very complex systems because it requires that the sample have long-range order, on the order of 100 Å. Also, for buried films composed of materials of similar atomic number, the difference in scattering factors is insufficient to allow LEED to distinguish the relative position of the elements in the film. Photoelectron diffraction has the added benefit of elemental specificity because of the unique binding energy of core-level electrons.

In a photoelectron diffraction experiment one records the angle-dependent or energy-dependent oscillations in the core level photoemission partial cross section. The unique binding energies of core-level electrons give photoelectron diffraction elemental specificity. The process begins with the ejection of a core level electron by an incoming photon of sufficient energy. The dipole selection rules for this process are:

$$\Delta l = l_f - l_i = \pm 1 \tag{1a}$$
$$\Delta m = m_f - m_i = \pm 1 \tag{1b}$$

where l_i and m_i are the angular momentum and the magnetic quantum numbers

of the initial core level and l_f and m_f describe the continuum final state. Once the free electron is created, part of this wave function, φ_0, propagates directly to the detector, and part of the wave, φ_j, scatters elastically off nearby atomic potentials before reaching the detector. The interference between these two parts of the photoelectron wave creates an intensity pattern in the 2π steradians above the crystal surface. The intensity of the photoemission peak is given by

$$I(k,\theta,\phi) \propto \left|\varphi_0 + \sum_j \varphi_j\right|^2 \tag{2}$$

where j represents all scattering paths, including multiple scattering paths, taken by the electron. k is the magnitude of the wavevector **k** and the angles θ and ϕ represent the emission direction.

$$k = |\mathbf{k}| = \frac{\sqrt{2m_e E_k}}{h/2\pi} \tag{3a}$$

$$k(\text{Å}^{-1}) = 0.512\sqrt{E_k(\text{eV})} \tag{3b}$$

This interference pattern is unique to the local geometry around the emitter. Through suitable calculations one can reconstruct the local geometry from the interferogram. Direct methods use Fourier transforms of the interference pattern to produce atomic positions that are within 0.1 Å of the true positions[11, 12]. More accurate structural determination requires comparison of the interference patterns to theoretical calculations[11, 12]. In the past, these theoretical calculations required significant amounts of computing time. However, with the improvements in computer hardware and improved calculation codes computing time is no longer a limiting factor[13].

The interference pattern consists of maxima and minima in the photoelectron intensity depending on the detection angle and the electron kinetic energy. In angle-scanned diffraction, one samples the interference pattern at one kinetic energy over several angles. The extension of this method to many hundreds of angles is known as photoelectron holography. The analogy to optical holography is intentional. In fact, this was the initial intention of Gabor when he first proposed holography. This method requires that either the sample or the analyzer rotate in both azimuthal and polar angles in order to record most of the 2π pattern. Through the appropriate three-dimensional Fourier transform one can obtain a real-space map of the atomic positions around the emitter. The lateral accuracy of this technique is quite good, better than one-tenth of an Ångstron. In the vertical direction, perpendicular to the surface however, the atomic positions are only known to about one Ångstrom resolution. Still, this technique is attractive in that it gives a direct

method, without the need for theoretical calculations, of determining the structure of the near surface. At high-kinetic energies, in the regime where forward scattering is the dominant scattering process, the holographic images are very useful, even without transformation. The forward scattering peaks which will be discussed more in Section III (Fig. 2) can provide elementally and chemically specific information about the symmetry of a buried layer.

If instead of recording the photoemission intensity as a function of emission angle, one measures the modulations as function of electron kinetic energy, the technique is then called energy-scanned diffraction by some researchers. We refer to this technique as Angle-Resolved Photoemission Extended-Fine Structure (ARPEFS), because of its similarity to EXAFS. The method requires a tunable x-ray source, such as a synchrotron. In the energy-scanned method one again records the angle-resolved photoemission intensity, but now the incoming photon energy is varied such that out-going photoelectrons from the core level will range from about 100 eV to 500 eV kinetic energy.

If the photoelectron is from a non-s initial state, $l_i \neq 0$, then by the dipole selection rules, Eqn. 1a, there are two possible emission channels. The final state interference between these two partial waves must be accounted for in the multiple scattering calculations. The computational complexity of handling these final state effects has, in the past, limited ARPEFS studies to s-initial states. The new calculation code developed by Chen, Wu, and Shirley makes it possible to fit the diffraction patterns created by electrons from non-s initial states to extract the most accurate structural parameters[14].

The ability to use non-s initial states in ARPEFS calculations enhances ARPEFS applicability to the study of transition metal overlayers. For s-initial states the photoemission cross sections are generally quite small compared to other levels, which makes their detection in dilute systems difficult over the whole ARPEFS range. While 1s states have larger cross sections than s-states with larger principal quantum numbers, they are very tightly bound. The K-shell of 3d transition metals requires hard X-rays for an ARPEFS experiment, while the K-shells of the 4d and 5d metals are inaccessible. For the 3d metals the use of very hard X-rays precludes one from performing an ARPEFS experiment with chemically shifted peaks. Measuring the ARPEFS modulations of a chemically shifted photoemission peak allows one to determine the chemically specific atomic structure. To resolve these energy shifts, one needs very good photon and electron-kinetic-energy resolution, as well as a natural linewidth that is narrow in comparison to the chemical shift. Hard X-ray monochromters generally do not have the necessary resolution to distinquish between chemically shifted peaks in the photoemission spectrum.

In a photoelectron diffraction experiment when one varies the detection angle or the photoelectron kinetic energy, E_k, one varies the amplitudes and phase differences between φ_0 and φ_j in Eqn. 2. The amplitude variations are due to the angle

and energy dependencies of the photoemission process and the atomic-scattering factors. The phase differences have two causes. The first is the interaction of the electron with the atomic potential in the scattering process. The second is the different path lengths traveled by the direct wave and the scattered waves before reaching the detector. It is the phase difference caused by path-length differences that carries the structural information. These intensity modulations, known as diffraction patterns, can then in principle be related to the local geometry around the emitting atom. The most accurate structural information is obtained by comparing experimental diffraction patterns to theoretical simulations.

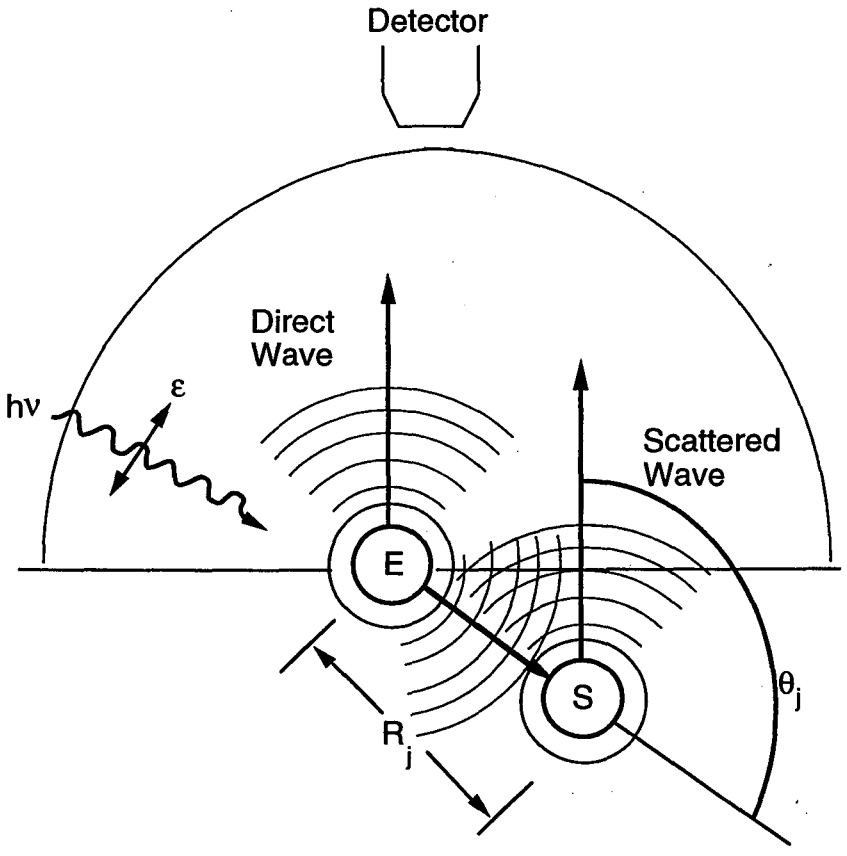

Figure 1. This schematic shows the important aspects of photoelectron scattering. A photon of energy $h\nu$ polarization ε ejects an electron from a surface atom. This atom is the emitter, labeled 'E'. The primary photoelectron wave propagates to the detector and part of the wave scatters off a nearby atom labeled 'S'. R_j is the scattering vector and θ_j is the scattering angle. The detector is a hemispherical electron-energy analyzer with an angle-resolving lens. It is shown here sampling the diffraction pattern at normal emission.

II. Scattering Theory

The electron scattering inside the solid is a complicated computational problem. A rigorous theoretical treatment must account for the curvature of the photoelectron wave, final state interference effects in photoemission from non-s initial states (Section II), and the multiple scattering events inside the solid. Most of these effects act to diminish the overall size of the diffraction modulations and are most important at lower kinetic energies. In this section we will discuss the important aspects of the scattering process in terms of plane-wave, single-scattering approximation.
The single scattering of a plane wave is the simplest approximation of photoelectron diffraction. This approximation is easy to understand and contains most of the important physics of the scattering process. A fully quantitative treatment accounts for multiple-scattering effects, final-state interference effects, and the curvature of the electron wave front. In the single scattering model, one assumes that the portion of the photoelectron incident on the scatterer has sufficiently low curvature, compared to the dimensions of the scattering potential, that it can be represented as a plane-wave. This is the small-atom approximation. To avoid the complications of final state interference effects, one also assumes that the initial state has zero angular momentum so that the final state before the scattering event is a p-wave. The final expression for the intensity at the detector, I(**k**) is:

$$I(\mathbf{k}) \propto \left| \hat{\varepsilon} \cdot \hat{k} \cdot e^{-L_0/2\lambda_e} + \sum_j \hat{\varepsilon} \cdot R_j \frac{f_j(\theta_j)}{R_j} W_j \cdot e^{-L_j/2\lambda_e} e^{-ikR_j(1-\cos\theta_j)+\psi_j(\theta_j)} \right|^2 \tag{4}$$

where $\mathbf{k}$ is the wave vector of the photoelectron and k its magnitude. θ_j is the scattering angle as shown in Fig. 1. ε is the photon polarization vector and R_j is the vector pointing from the emitter to the scatterer. L_0 is the distance from the emitter to the surface, and L_j is the total path length traveled by the photoelectron from the emitter to the scatterer to the surface. W_j is a Debye-Waller factor that accounts for the attenuation of the diffraction oscillation amplitude by the scatter's and emitter's thermal vibrations. $\varepsilon \cdot \mathbf{k}$ and $\varepsilon \cdot R_j$ represents the s-level photoemission cross section of the photoelectron in the direction of the detector and the scatterer, respectively. $f_j(\theta_j)$ is the complex, plane-wave scattering-factor with a magnitude equal to $|f_j(\theta_j)|$ and a phase equal to $\psi_j(\theta_j)$. The scattering factor can be calculated from

$$f_j(\theta_j) = \frac{1}{2ik} \sum_{l_j=0}^{l} (2l_j + 1) \cdot e^{(2i\partial_{l_j})-1} P_{l_j}(\cos\theta_j) \tag{5}$$

where l_j is the angular momentum of each partial wave, ∂_{l_j} is the phase shift of the l_j^{th} partial wave for the jth scatterer, and P_{l_j} is the l_j^{th} order Legendre polynomial. The limit on the sum is $l_{max} = kR_{MT}$, where R_{MT} is the effective or muffin-tin radius of the scattering potential.

The magnitude and phase of this scattering factor for scattering from Ni atoms at energies from 100 eV to 500 eV are shown in Fig. 2. The amplitude of the scatter-

ing factor has a prominent peak in the forward-scattering direction, $\theta_j = 0°$ and a significant amplitude in the back-scattering direction, $\theta_j = 180°$. The generally small phase shift in the forward-scattering direction also implies that this peak in forward-scattering direction will produce enhanced intensity in that direction. Some authors have called this forward-scattering preference "forward focusing".

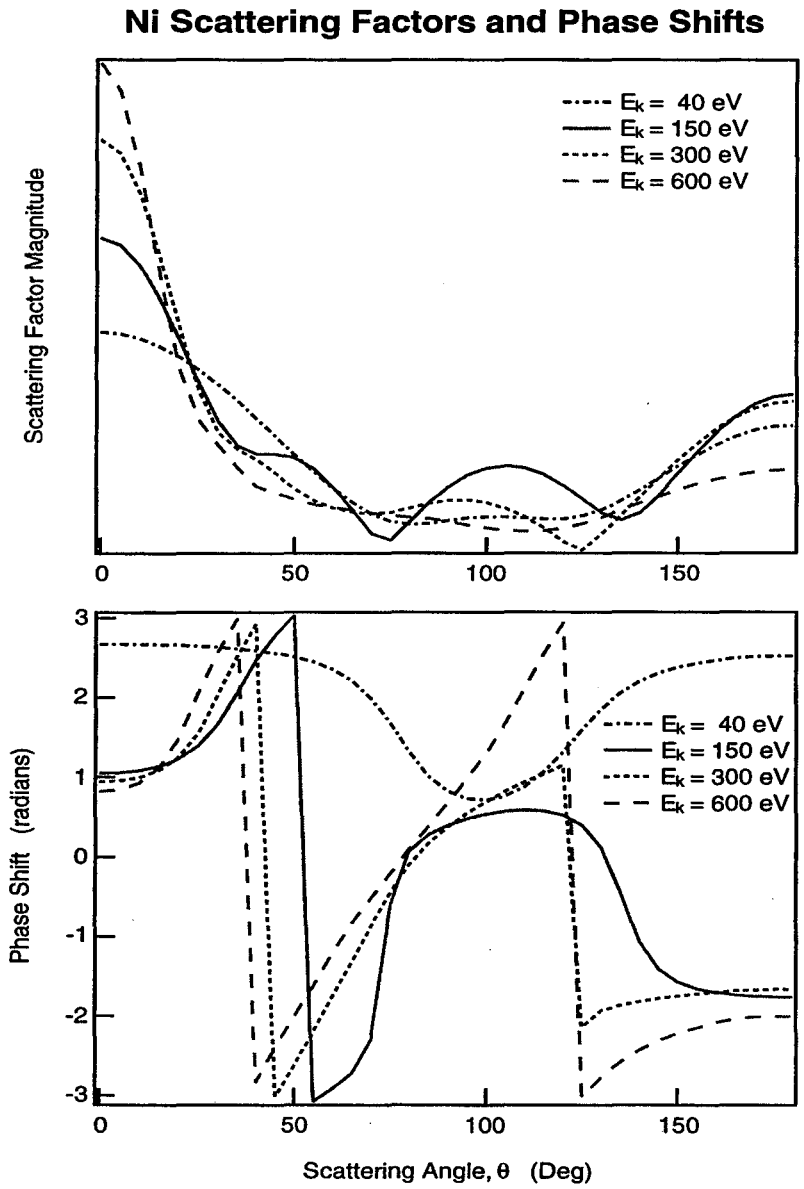

Figure 2. Top panel: the Ni scattering factors for electron kinetic energies from 40 eV to 600 eV. Note the enhancement of scattering in the forward direction, $\theta_j = 0°$, as the electron kinetic energy increases. Bottom panel: Ni scattering phase shift for electron kinetic energies from 40 eV to 600 eV. Again the forward scattering direction is noteworthy because of the small phase shift.

This phenomena is very useful for studying the structure of near-surface, buried films with photoelectron holography. These forward-scattering peaks correspond to very short path-length differences. The back-scattering peaks in the scattering-factor plots are the most important for ARPEFS. The APREFS data reduction removes most of the information from the forward-scattering peaks and emphasizes the back-scattering information. ARPEFS emphasis on back scattering makes it an excellent probe of adsorbate structure.

The quantity $kR_j(1-\cos\theta_j)$ in Eqn. 4 represents the geometric phase shift associated with extended path followed by the scattered part of the photoelectron wave. This phase difference arises due to the different distances traveled by the primary wave φ_0 and the scattered wave φ_j before reaching the detector. This phase shift contains the bond-length information.

Photoelectron diffraction is an inherently surface and near surface technique. The reasons for this are two-fold. The first is the $1/R_j$ dependence of the outgoing spherical wave as it passes to each scatterer, Eqn. 4. Additionally, the inelastic scattering of the electrons in the solid further limits the information depth. The inelastic mean free path of the photoelectrons is accounted for in Eqn. 4 by the factors $e^{-L_0/2\lambda_e}$ and $e^{-L_j/2\lambda_e}$ where λ_e is the mean free path of the electron in the scattering medium.

The first step in ARPEFS data analysis usually is to take the Fourier transform (FT) of the $\chi(k)$ curve. This transforms the diffraction curve from k-space to real-space path-length differences (PLD). This method ignores multiple-scattering and phase-shift effects, but usually allows one to determine the adsorption site and the bond lengths within two-tenths of an Ångstrom. The next step is to fit the $\chi(k)$ data to multiple-scattering spherical-wave (MSSW) calculations to obtain very accurate structural parameters, usually better than 0.010 Å.

In summary, photoelectron diffraction is an excellent technique for obtaining very accurate information about the local atomic structure of interesting thin-metal films. The thin films studied in this dissertation are the basic building blocks of the new layered materials which exhibit exotic magnetic behavior. Detailed knowledge about the local atomic structure is essential for a fundamental understanding of the two-dimensional magnetic behavior. ARPEFS, or energy-scanned diffraction, is most sensitive to emitters in a strong back scattering environment, that is adsorbates. New scattering calculation codes enable one to study the diffraction signal from arbitrary electron initial states, greatly broadening the range of materials that can be studies. The importance of forward scattering in high-energy photoelectron holography makes this technique especially sensitive to probing the atomic abruptness of the interfaces of theses intertransition-metal layered materials. The elemental specificity of photoelectron diffraction makes it a very attractive alternative to LEED for many of the studies of these systems. The hope is that accu-

rate knowledge about the local geometry of these materials will lead to a better understanding of two-dimensional magnetism.

III. Contents

The remainder of this dissertation is organized as follows: Chapter 2 describes the ARPEFS study of thin-Fe films grown on Au(100). The Fe grows layer-by-layer with one monolayer of Au atoms, acting as a surfactant, remaining on the surface of the growing Fe film. In Chapter 3, I examine two manganese surface alloys, MnNi and MnCu. The one-half monolayer coverage alloys are highly corrugated. Using a combination of ARPEFS and photoelectron holography we accurately determine the local atomic structure of the alloy layer, and using holography determine the atomic discreteness of the Mn layer. Chapter 4 is an ARPEFS study of a two-dimensional oxide grown on W(110). The oxide has very long-range order, as shown by the complex LEED pattern, but the local structure is very similar to other O/W(110) phases. Chapter 5 describes instrumental improvements to the electron lens system used with a hemispherical electron-energy analyzer, as well as improvements to the analyzer itself and the analyzer power supplies.

References

[1] A. J. Freeman and R. Wu, Magn. Magn. Mater. **100**, 497 (1991).

[2] P. F. Carcia, A. D. Meinholdt, and A. Suna, Applied Physics Letters **47**, 178 (1985).

[3] U. Gradmann and J. Müller, Phys. Status Solidi **27**, 313 (1968).

[4] G. Binasch, P. Grunberg, F. Saurenbach, and W. Zinn, Physical Reveiw B. **39**, 4828 (1989).

[5] M. M. Baibich, J. M. Broto, A. Fert, F. N. V. Dau, F. Petroff, P. Eitenne, G. Creuzet, A. Frederich, and J. Chazelas, Physical Review Letters **61**, 2472 (1988).

[6] S. S. P. Parkin, N. More, and K. P. Roche, Physical Review Letters **64**, 2304 (1990).

[7] J. M. Daughton, Thin Solid Films **216**, 162 (1992).

[8] Z. Huang, Ph.D. (University of California, Berkeley, 1992).

[9] J. W.F. Egelhoff, Crit. Rev. Solid State Mater. Sci **16**, 213 (1990).

[10] G. Binning and H. Rohrer, Helv. Phys. Acta **55**, 2795 (1982).

[11] J. J. Barton, C. C. Bahr, S. W. Robey, Z. Hussain, E. Umbach, and D. A. Shirley, Phys. Rev. B **34**, 3807-3819 (1986).

[12] J. J. Barton, Ph.D. Thesis (The University of California, Berkeley, 1985).

[13] S. Tanuma, C. J. Powell, and D. R. Penn, Surf. Interface Anal. **11**, 577- 589 (1988).

[14] Y. F. Chen, W. Wu, and D. A. Shirley, (To be published).

...But when you grow up in those suburbs–when you've seen the streams, woods, farms, and ponds dying all around you but have been lucky enough to escape every weekend or vacation to a wild river full of beautiful game fish, only to return home to the sight of hopeful little kids with impossibly crappy poles plying poisoned creeks where even the crawdads have died– it does something: something way inside me would start to die...

...Across the road from my cabin was a huge clear-cut–hundreds of acres of massive spruce stumps interspersed with tiny Douglas firs–products of what they call "Reforestation," which I guess makes the spindly firs en masse a "Reforest," which makes an individual spindly fir a "Refir," which means you could say that Weyerhauser, who owns the joint, has Refir Madness, since they think that sawing down 200-foot-tall spruces and replacing then with puling 2-foot Refirs is no different from farming beans or corn or alfalfa. They even call the towering spires they wipe from he earth's face forever a " crop" –as if they'd planted the virgin forest! But I'm just a fisherman and may be missing some deeper significance in their strange nomenclautre and stranger treatment of primordial trees...

...There's just nothing like the feel of a trout dancing through the river, making the pole pulse like a heart in your hands. It does to the hands what the sight of your sweetie does to your body, what dreams of eternity do to your heart, what milk chocolate does to your mouth...And yet we killed two trout. It's strange to kill your dance partners, but that's what we did. We did it because the world is strange–because this is a world where no matter who you are or where you live or what you eat or whether you choose or don't choose to undersatnd and be grateful, it is sacrifice–sweet. bleedomg sacrifice–that sustains you. So we killed two trout, but knew no sacrificial prayers, and so simpley knelt by the river, commended them on how well the'd fought... then broke their bodies to sustain our own.

David James Duncun, The River Why

CHAPTER 2

Surface Structure Determination of Au(1 ML)/Fe(15 ML)/Au(100) Using Angle-Resolved Photoemission Extended Fine Structure

I. Introduction:

A great amount of attention has been given to investigating thin magnetic films and magnetic multilayers, especially systems involving iron and the noble metals[1-8]. In most of these studies the authors assume that the Fe layers will maintain bulk spacing even at interfaces. However, it is well known that for the clean metal the first and second layer spacing is contracted from the bulk value, and that absorbates can significantly expand this spacing[9-20]. Atomic structural details about these interfaces are important because the electronic states that are localized at the interface between the two different materials are critical in determining the magnetic properties of ultra-thin films and multilayers[21, 22]. For example, the bonding at the interface induces a magnetic moment in the non-magnetic material, thus ferromagnetic order is attained in the non-magnetic noble metal overlayers on iron. The resulting magnetization is often sizable but decays rapidly away from the interface on the scale of a few atomic layers[23].

In this study we use Angle-Resolved Photoemission Extended Fine Structure (ARPEFS) to investigate thin (*ca.* 10 and 15 monolayers) Fe films grown on a Au(100) single crystal. ARPEFS is a well established technique for determining the atomic structure of atomic and molecular adsorbates on metal surfaces[18, 19, 24-27]. The technique's advantages are its atomic selectivity due to the unique binding energies of core level electrons, the large oscillations, which in this study are ± 40%, and its inherent accuracy. In the past, structural determinations have only been done with ARPEFS signals from initial states with zero angular momentum because of the difficulties in treating non-s initial states in the scattering calculations. This

study presents the first structure determination of a bimetalic system using the ARPEFS from non-s initial states. We report results from a new computer simulation and fitting procedure based on the Rehr and Albers formalism[28]. This program, developed by our group, uses second-order matrices (6x6) and up to eighth-order scattering to produce a convergent calculation at these electron energies and inter-atomic distances[29].

II. Experimental

The experiment was performed at the Advanced Light Source (ALS) on the bend magnet beamline 9.3.2, which covers the photon energy range of 30 eV to 1500 eV. The ultra-high vacuum (UHV) chamber is equipped with a high precision, five-axis manipulator capable of a temperature range from 80 K to 2500 K and other standard surface science techniques for sample preparation and characterization. The photoemission data were collected with two-axis rotatable, 50 mm mean radius hemispherical, electron energy analyzer equipped with multichannel detection. The angular resolution of the electron lens system for the analyzer is ± 2.0 degrees. Kevan describes the analyzer more completely[30].

The gold crystal was spark cut from a high-purity boule and oriented with Laue x-ray back reflection to within ± 0.5 degree of the [100] direction. The crystal was mechanically polished with six μm and one μm sized diamond paste, and finally with a 0.05 μm CeO_2 slurry. Because gold is very soft, the mechanical polishing steps create a deep, polycrystalline, damaged layer which must be removed in order to obtain high quality, ordered surfaces. Electro-polishing is the best method to remove this damage layer. We used the Markinovich method described in appendix A[31]. After repeated cycles of Ar^+ ion sputtering, $E_k = 500$ eV, $I_e = 10$ μA, and annealing to 550° C in vacuum, we could detect no carbon or sulfur, and saw a sharp 5x20 LEED pattern.

The iron source was a 99.999% purity iron wire heated by electron bombardment. The base pressure in the experimental chamber was 7×10^{-11} torr, while during the evaporation, which lasted 15 minutes, the pressure rose to 8×10^{-10} torr. To determine the iron coverage, we plotted the gold $4f_{7/2}$ photoemission peak intensity and the iron 3p peak intensity against the Fe evaporation time, assigning a value of 1 monolayer (ML) to the first break in the slope of each of these two curves, Fig. 1. The bulk iron layer was then grown at room temperature with evaporation times of ten and 15 times the 1 ML evaporation time, and ARPEFS curves taken of these two samples. After the Fe evaporation we detected no contaminants on the crystal surface and observed a bright and sharp 1x1 LEED pattern, unrotated relative to the substrate Au(100) face.

The sample temperature, measured with a liquid nitrogen reference junction and a thermocouple mounted very near the sample, was 80 K for all the data shown here.

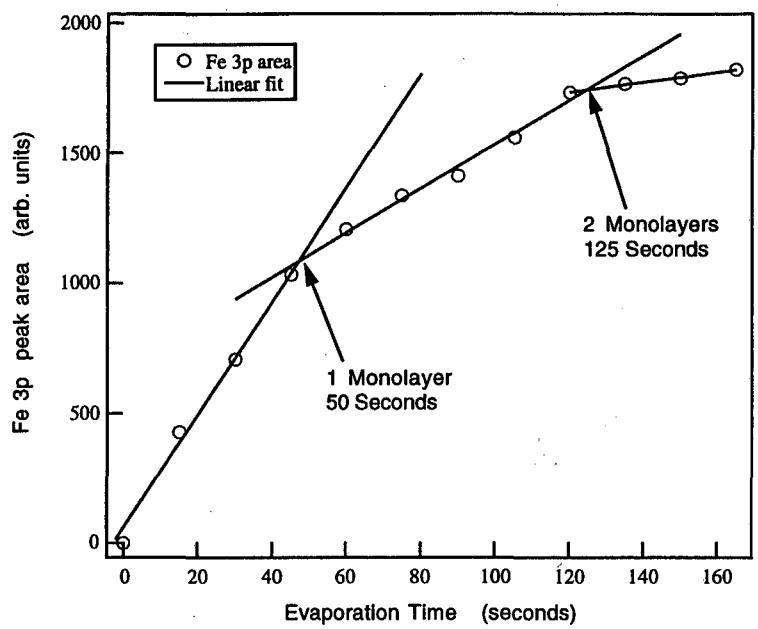

Figure 1. Fe 3p peak area *vs* evaporation time. Circles are the data points taken every 15 seconds. The solid line is a linear fit showing each break in the slope at each completed monolayer.

III. Data analysis

The primary ARPEFS data consist of three sets of Au(4f) photoelectron spectra, two collected in the [100] direction and one collected in the [110] direction. In each data set the photon energies were chosen such that the Au(4f) photoelectron kinetic energies are equally spaced in electron wave number, k; k ranges from 5.3 $Å^{-1}$ to 12.0 $Å^{-1}$ in 0.1 $Å^{-1}$ steps. Each of the 67 individual photoemission curves for each data set was fitted with a Voigt function, s step function for each peak and a background offset. A Voigt function is the convolution between a Lorenztian describing the peak's natural linewidth and a Gaussian describing the experimental contribution to the peak's width. Fig. 2 shows a typical spectrum and fit. We fitted each spectrum to extract the most accurate peak intensities to construct the $\chi(k)$ diffraction curve. The function $\chi(k)$ is defined by[24]

$$\chi(k) = \frac{I(k)}{I_0(k)} - 1 \tag{1}$$

where $I(k)$ is each individual peak area plotted as a function of its position in k-space. $I_0(k)$ is a smooth, slowly varying function with a much slower oscillation frequency than $I(k)$, which depends on the inelastic scattering processes and the

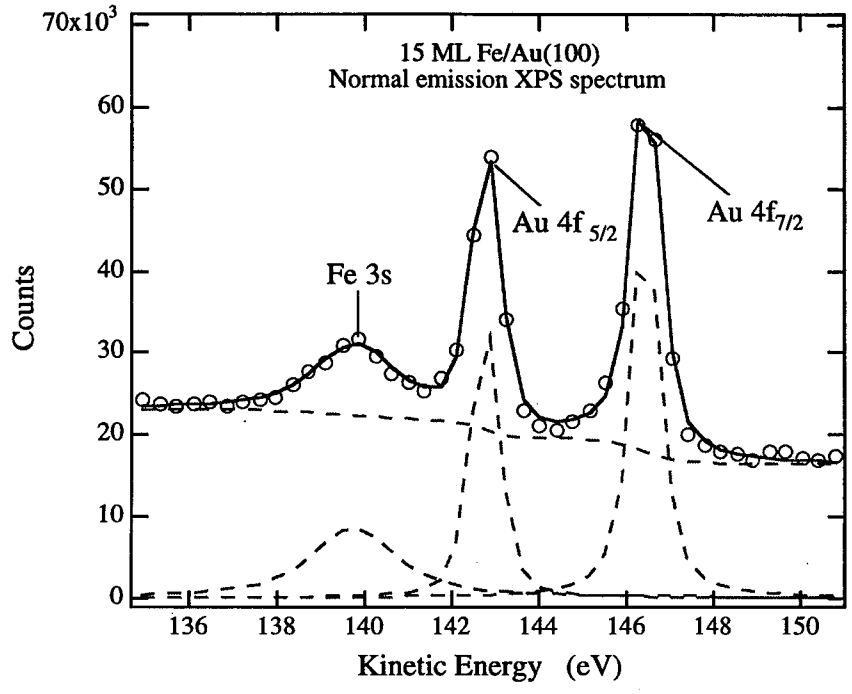

Figure 2. A typical photoemission spectrum from the 15 ML Fe/Au(100) system. The open circle are the data, the solid line is the fit to the data and the dashed lines the Voigt function peaks and background.

varying atomic cross section. We determined $I_0(k)$ by fitting a smooth, cubic spline through the intensity curve. The experimental ARPEFS data thus obtained are plotted in Fig. 3 along with the best fit results from the multiple scattering calculations which will be discussed later.

The generally accepted growth mode of iron on Au(100) is Fe layer by Fe layer with one monolayer of gold, acting as a surfactant, migrating to the surface of the growing iron layer[5,7,32]. To test this growth model, at the end of ARPEFS data collection we lightly sputtered the Fe/Au(100) sample with 200 eV Ar+ ions, periodically checking the Fe 3p and Au $4f_{7/2}$ peak intensities. After a total sputtering time of 20 minutes, the Au $4f_{7/2}$ signal was undetectable, and the sample still showed a bright, 1x1 LEED pattern. We also compared the Fe 3s and Au 4f peak intensities from the 15 monolayer Fe sample following a procedure outlined previously by Fadley[33]. For a substrate with a uniform overlayer of thickness t, the substrate peak intensity, N_s, and the overlayer peak intensity N_1 are given by Equation 2:

$$\begin{aligned} N_S &= I_0\Omega_0(E_S)D_0(E_S)\rho_S(d\sigma_S / d\Omega)\cdot e^{(-t/\lambda_s(E_s)\cos\theta)} \\ N_1 &= I_0\Omega_0(E_S)D_0(E_S)\rho_1(d\sigma_1 / d\Omega)\cdot(1-e^{(-t/\lambda_1(E_1)\cos\theta)}) \end{aligned} \tag{2}$$

Experimental Data and Mulitiple Scattering Fits

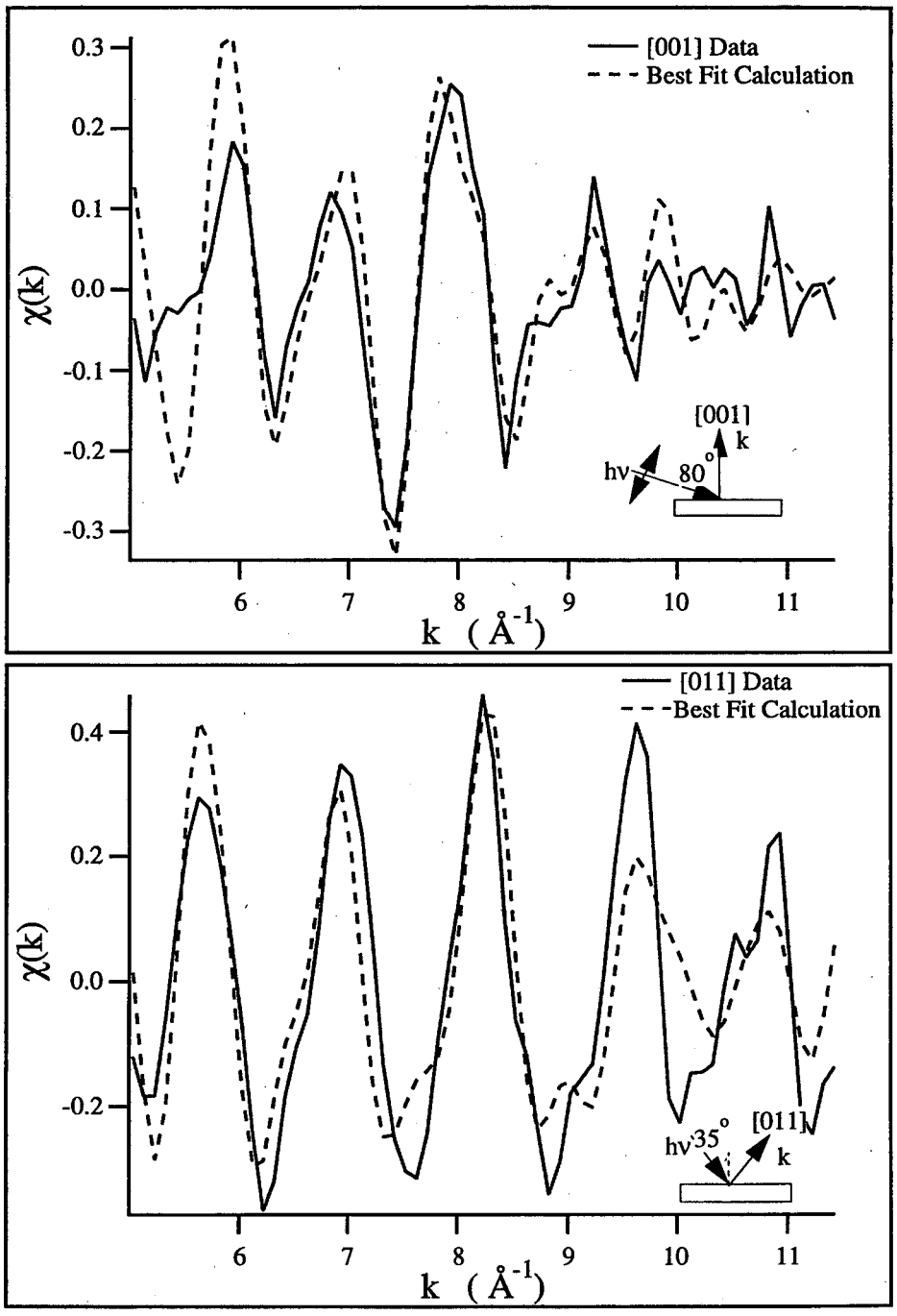

Figure 3. ARPEFS data from the Au 4f core level for 1ML Au/15ML Fe/Au(100) in the [001] and [011] directions. Schematics of each experimental geometry are shown. Dashed lines are the best fit multiple scattering modeling calculation results. The largest-amplitude oscillations in each curve arise from strong backscattering off the nearest-neighbor Fe atoms in the [001] and [011] directions, respectively. See Fourier transforms in Fig. 5.

Where I_0 is the photon flux, and Ω_0 is the electron analyzer's mean acceptance angle for a given kinetic energy along a given emission direction. The mean emission direction is assumed to be at an angle q with respect to the surface normal. D_0 represents the detector efficiency for a given kinetic energy, and ρ_s and ρ_l are the respective atomic desities of the substrate and the overlayer. $\lambda_s(E_s)$ is the electron attenuation length in the substrate, $\lambda_l(E_l)$ the attenuation length in the overlayer, and $(d\sigma / d\Omega)$ is the subshell photoionization cross section from reference[34] The electron attenuation length was determined for each material using the Tanuma, Powell, and Penn (TPP-2) formula[35]. Fig. 4 shows the plots of attenuation length for both gold and iron versus electron kinetic energy determined from this formula. If we assume that those quantities in Eqn. 2 which depend on the electron's kinetic energy are equal for both the iron and gold peaks because the Fe 3s and Au 4f binding energies differ by only 3.7 eV, and that the photon flux is constant during the data acquistion time, then the intensity ratio of the Au $4f_{7/2\ to}$ the Fe 3s is given by

$$\frac{N_{Au}}{N_{Fe}} = \frac{\rho_{Au}(d\sigma_{Au} / d\Omega)\lambda_{Au}(E)}{\rho_{Fe}(d\sigma_{Fe} / d\Omega)\lambda_{Fe}(E)} \cdot (1 - e^{(-t/\lambda_{Au}(E_{Au})\sin\theta)} e^{(t/\lambda_{Au}(E_{Fe})\sin\theta)}) \qquad (3)$$

Comparing the theoretical ratio from Eqn. 3 with the experimental ratio taken as the average of several fitted photoemission curves (Fig. 2) we find the experimental intensity ratio to be 22% smaller that the theoretical calculation for a monolayer

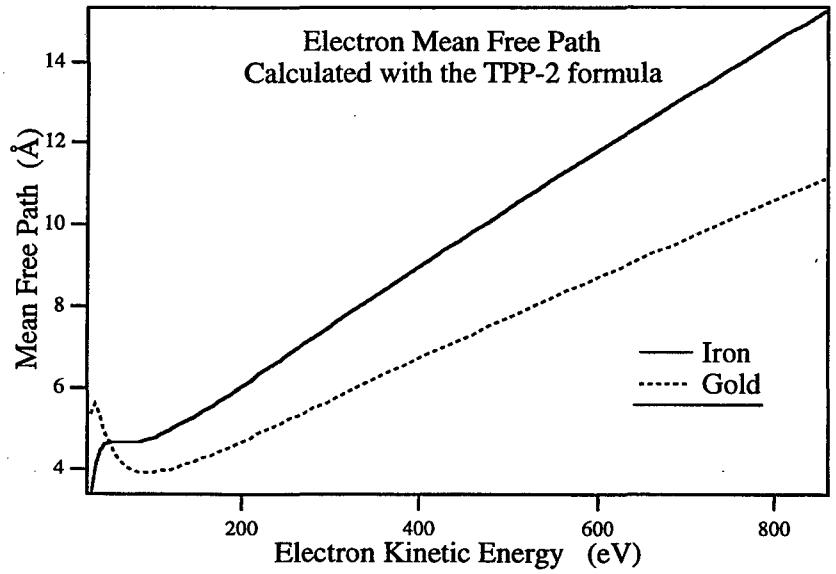

Figure 4. The mean free path for iron(solid line) and gold(dashed line) *vs* electron kinetic energy calculated by the TPP-2 formula.

coverage of gold on bulk iron. We take this as further evidence for a single monolayer growth mode. The 22% error is within the error limits for such a calculation, considering the weakness of the Fe 3s signal and the fact that this is an angle-resolved photoemission experiment so that electron wave interference effects can affect the peaks' intensity ratios. We note that the surface free energies of gold (1.410 J/cm^2) and iron (2.150 J/cm^2) make it thermodynamically favorable for gold to be the surface layer.

The auto-regressive linear-prediction based Fourier transform (ARLP-FT) transforms the diffraction data from momentum space to real space[36]. In ARPEFS, the positions of the strong backscattering peaks in ARLP-FTs from adsorbate/substrate systems can be predicted with fairly good accuracy using the single-scattering cluster model together with the concept of strong backscattering from atoms located within a cone around 180° from the emission direction. The effective solid angle of this backscattering cone is *ca.* 30° to 40°, though signals from scattering atoms very close to the source atom may be observable even if the scatters lie outside the nominal backscattering cone. Most notably this applies to the nearest neighbor Au atoms in the surface layer for this system.

The ARLP-FT peaks correspond to path-length differences between that component of the wave which propagates directly to the detector and those components which are first elasticly scattered by the atomic potentials within this backscattering cone. This scattering takes place within the crystal, which requires that the ARPEFS data be shifted to account for the effect of the inner potential. In the modeling calculations the inner potential is treated as an adjustable parameter, but for the Fourier analysis we estimate its value as the sum of the work function and the valence band width which for the present case we take to be 12.6 V. Thus we shifted the ARPEFS data by 12.6 eV to higher kinetic energy before calculating the ARLP-FT.

Analysis of the ARLP-FT provides information about the adsorption site as well as the bonding distance of the gold atoms. The 1x1 LEED pattern suggests a high-symmetry absorption site, and the fact that the lattice constant for bcc iron is a factor of $\sqrt{2}$ smaller than the lattice constant of FCC gold further points to the four-fold hollow as the likely binding site. Using the bulk Fe interlayer spacing, 1.43 Å and ignoring phase-shift effects, the strongest peak in the [100] ARLP-FT at 6.0 Å can be used as a calibration to calculate the distance between the Au and the first-layer Fe atoms for each high symmetry absorption site, atop, bridging, or four-fold hollow. Using only plane geometry one can then calculate the path length differences (PLD) and scattering angles for strong scattering events from each adsorption site geometry and compare to the observed peaks in the ARLP-FTs. This comparison for both the [100] and [011] emission directions is shown in Fig. 5.

The Fourier analysis agrees best if the Au atoms adsorb in the four-fold hollow *ca.* 1.57 Å above the first layer iron. The peak at 6.0 Å corresponds to backscattering from the second layer iron atoms. For this geometry the predicted and observed

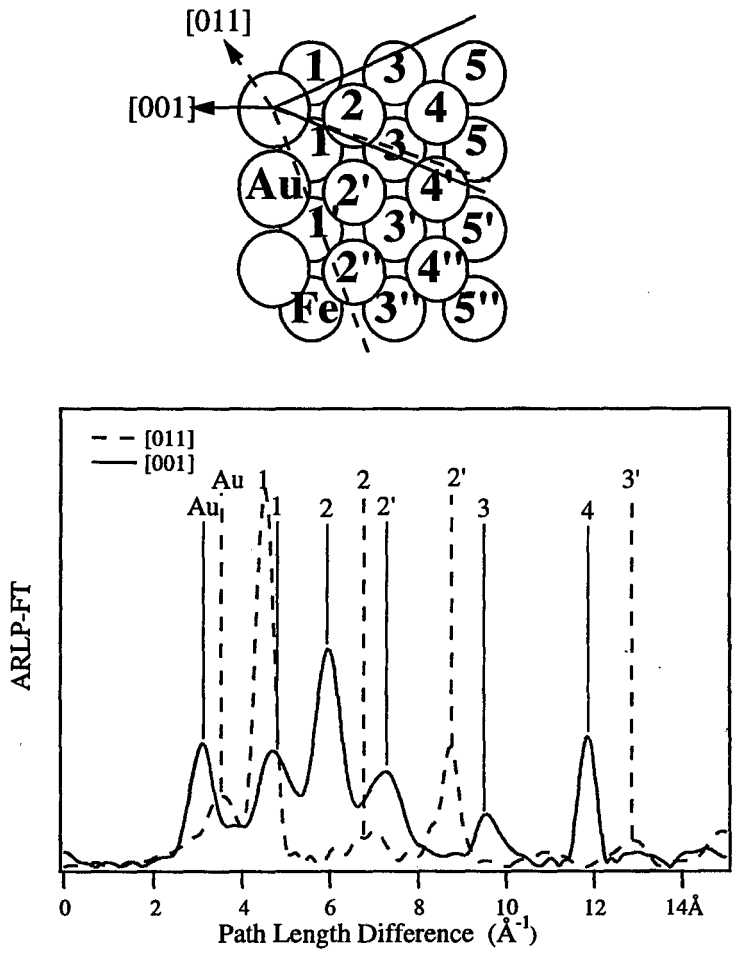

Figure 5. ARLP-FTs of the ARPEFS [001] data (solid line) and the [011] data (dashed line). A model of the lattice with the backscattering cones for each emission direction indicates the scattering atoms coresponding to the FT peaks. Note the excellent agreement between peak positions and calculated values.

PLD are in very good agreement and the relative peak strengths are reasonable for the scattering angles.

Fitting the experimental diffraction curves to a multiple-scattering model yields more precise structural parameters than that given by the Fourier analysis alone. Chen, Wu, and Shirley recently developed a new multiple-scattering code, based on the Rehr-Albers formalism, which can model initial states with arbitrary angular momentum and which is fast enough to allow practical fitting to be done[28, 29]. This calculation requires both structural and non-structural parameters. We used the structural parameters determined by the Fourier analysis as the initial guesses in the fitting procedure. The non-structural parameters include the initial-state angular momentum, the atomic scattering phase-shifts, the crystal tempera-

ture, the inelastic mean free path, the emission and light polarization directions, the electron analyzer acceptance angle, and the inner potential.

To account for the vibrational effects of the bulk atoms, the mean square relative displacement was calculated and the correlated Debye temperature was set to 265 K. The atomic-scattering phase-shifts were calculated using the atomic potentials tabulated by Moruzzi *et al*[37]. The emission and polarization directions and the analyzer acceptance angle were set to the experimental values described previously[30]. The inelastic mean free path was included using the exponential damping factor $e^{-\frac{t}{\lambda}}$ where λ was calculated using the Tanuma, Powell, and Penn (TPP-2) formula[35].

The scattering code allows for several curves of the same initial state to be fitted simultaneously. In this case the two $\chi(k)$ curves from the 15 ML sample with emission along the [100] and [110] directions were fit simultaneously. The [100] emission $\chi(k)$ curve from the 10 ML sample was fitted separately. We determined the best fit by minimizing the A-factor function defined as

$$\text{A} - \text{factor} = \frac{\sum(\chi_c - \chi_e)^2}{\sum\left(\chi_c^2 + \chi_e^2\right)} \tag{4}$$

We employ the A-factor in the fitting routine instead of the conventional R-factor because when the fit is far from its minimum the A-factor emphasizes the importance of the structurally-sensitive $\chi(k)$ curve periodicity, over the absolute peak intensity. Near the minimum the A-factor and R-factor analyses are functionally equivalent. We report the conventional R-factor throughout this paper.

We show the experimental $\chi(k)$ curve and the best fit for each emission direction in Fig. 3. For these fits we used an 88-atom cluster and allowed the Au-Fe1, Fe1-Fe2, and Fe2-Fe3 layer spacings to vary, as well as the inner potential and the Debye temperatures of the near surface layers. During the data analysis it was obvious that, for initial states with orbital angular momentum greater than zero, the diffraction curves are very sensitive to small errors in the measured emission direction. For this reason an iterative process was employed to find the best fit. First, a fitting to the multiple-scattering calculation was performed with the Fourier analysis parameters as the starting structural parameters. The best-fit results of this fitting process were then held fixed as the emission direction in the code was allowed to vary. The resulting best-fit value for the emission angle was then used as the input for the next set of calculations. This iterative process was continued until the emission direction converged. We found that the true emission direction was 4° from that determined experimentally for both the [100] and the [011] directions. We attribute this error to a misalignment of the experimental-chamber viewports used in the laser auto-collimation orientation procedure.

The best fits determine the Au-Fe1 spacing to be 1.67 Å, and the Fe1-Fe2, and the Fe2-Fe3 spacing to be that of the bulk iron, 1.43 Å, within the experimental error limits. It is interesting to note that this value is a slight expansion of interlayer spacings relatiave to the clean metal[38]. A surface Debye temperature of 265 K and an inner potential of 13.8 V were found to give the best fit. The best fit value for the Debye temperature is noteworthy because it is a measure of the disorder in the system. ARPEFS observes the thermal averaging of the interference effects in which the vibrational motions of the surface atoms attenuate the oscillation amplitude of the $\chi(k)$ function. In the same manner sample imperfections, i.e. intermixing of the gold and iron layers and roughness of the grown iron layers will also attenuate amplitude of $\chi(k)$. Analysis of the ARLP-FTs shows peaks corresponding to scattering events from as far away as the fourth iron layer. Wang *et al.* showed previously that information from such large (PLD) is lost as the sample temperature approaches the Debye temperature, that is as the sample becomes more disordered[39, 40]. The fact that we see such long PLD is another indication of the qualitiy of the iron films and the sharpness of the iron-gold interface. The very good agreement between the predicted and the observed peaks in the ARLP-FT and the presence of sharp ARLP-FT peaks due to scattering from the fourth Fe layer, shows the Fe lattice to be very like the Fe bulk.

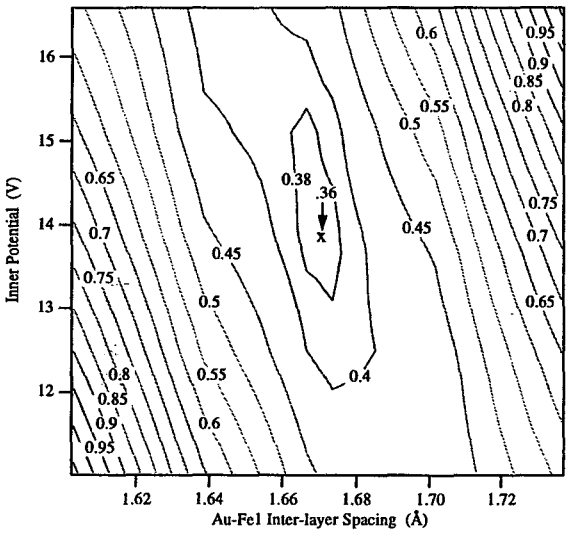

Figure 6. R-factor *vs.* inner potential and Au-Fe1 interlayer spacing. The minimum is at a layer spacing of 1.67 ±0.02 Å. The Fe1-Fe2 interplanar distance is held constant.

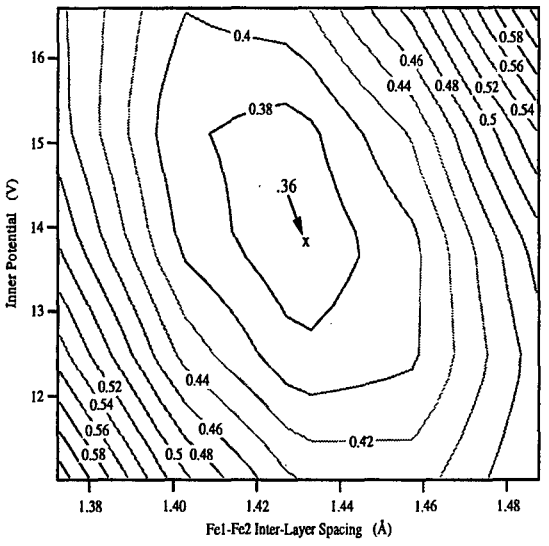

Figure 7. R-factor *vs.* inner potential and Fe1-Fe2 interlayer spacing. The minimum is at an interlayer spacing of 1.43 ±0.03 Å

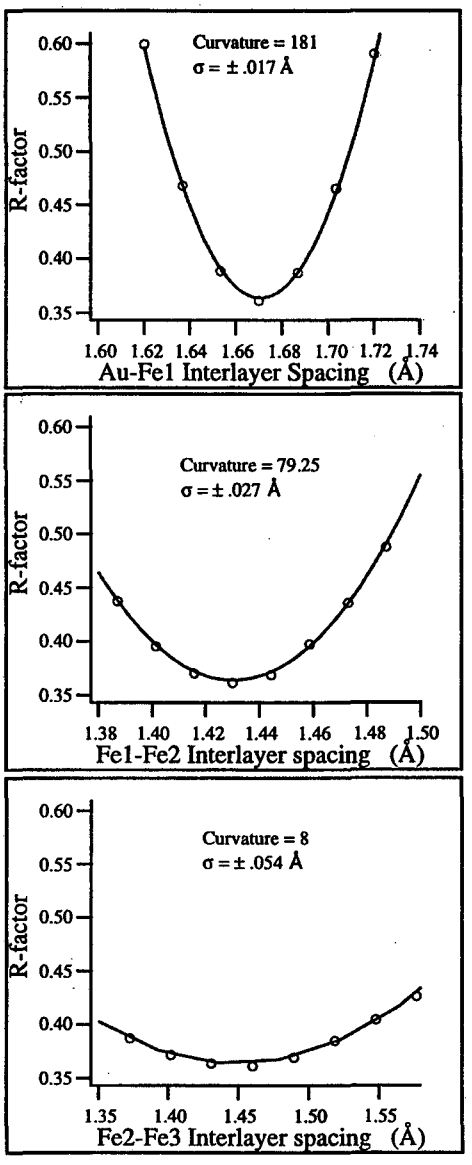

Figure 8. R-factor *vs.* the interlayer spacing (open circles) and a parabolic fit (solid line) for A) Au-Fe1 B) Fe1-Fe2, and C) Fe2-Fe3. The inner potential is fixed at 13.6 V for all calculations.

IV. Error Analysis

To establish the sensitivity of the fitting procedure to the layer spacings and establish error bars we calculated the R-factor for the various interlayer spacings and inner potential. It has been shown that the inner potential may affect the derived layer spacings and must be included in the R-factor analysis[27]. Fig. 6 shows the R-factor contours *versus* the Au-Fe1 layer spacing and the inner potential. Fig. 7 shows a similar plot for the distance bewteen the first and second layer Fe and the inner potential. These plots show very steep valleys in the interlayer spacing direction with very broad valley floors in the inner potential direction, indicating the relative insensitivity of the fits to the inner potential value. With the inner potential held fixed at the best-fit value of 13.8 V the R-factor analysis for the gold first layer

spacing, first layer iron second layer iron, and second layer iron third layer iron are shown in Fig. 8. Huang discussed the determination of error bars in ARPEFS from the R-factor analysis[26]. Following his treatment we quote error bars of plus or minus one standard deviation. We conclude from the MSSW calculation and the R-factor analysis that the Au-Fe1 spacing is 1.67 ± 0.02 Å, the Fe1-Fe2 spacing to be 1.43 ± 0.03 Å, and the Fe2-Fe3 spacing to be 1.46 ± 0.05 Å.

V. Conclusion

We have measured the Au 4f ARPEFS signal from 1ML Au / 15 ML Fe / Au(100) and find that the iron grows layer by layer with one monolayer of Au sitting in the four-fold hollow site of the bcc iron. We find that the layer spacing between the top gold layer and the first iron layer is 1.67 ± 0.02 Å, the spacing between the first and second layer iron atoms is 1.43 ± 0.03 Å, and the interlayer spacing for second and third layer iron atoms is 1.46 ± 0.05 Å. The Fourier analysis indicates that the growing iron layers are very like bulk Fe with a BCC lattice. We have also demonstrated a new multiple-scattering code and fitting procedure based on the Rehr-Albers formalism that can calculate up to eighth-order scattering, using 6x6 scattering matrices rapidly enough to allow practical fitting to be done.

References

[1] F. Ciaccacci and S. D. Rossi, Physical Review B **51**, 11538-11545 (1995).

[2] E. Vescovo, O. Rader, J. Redinger, S. Blugel, and C. Carbone, Physical Review B **51**, 12418-12424 (1995).

[3] F. J. Himpsel, Physical Review B **44**, 5966-5969 (1991).

[4] J. M. Maclaren, M. E. McHenry, S. Crampin, and M. E. Eberhart, Journal of Applied Physics **67**, 5406-5411 (1990).

[5] S. D. Bader and E. R. Moog, Journal of Applied Physics **61**, 3729-3734 (1987).

[6] W. Gerts, Y. Suzuki, T. Katayama, K. Tanaka, K. Ando, and S. Yoshida, Physical Review B **50**, 12581-12586 (1994).

[7] Y.-L. He, Y.-F. Liew, and G.-C. Wang, Journal of Applied Physics **75**, 5580-5582 (1994).

[8] W. Heinen, C. Carbone, T. Kachel, and W. Gudat, Journal of Electron Spectroscopy and Related Phenomena **51**, 701-712 (1990).

[9] W. Arabczyk, H.-J. Müssig, and F. Storbeck, Surf. Sci. **251/252**, 804-808 (1991).

[10] W. Arabczyk, T. Baumann, F. Storbeck, H. J. Müssig, and A. Meisel, Surf. Sci. **189/190**, 190-198 (1987).

[11] Osterwalder, and C. S. Fadley, Phys. Rev. Lett. **63**, 283-286 (1989).

[12] S. R. Chubb and W. E. Pickett, Phys. Rev. B **38**, 10227-10243 (1988).

[13] R. Imbihl, R. J. Behm, G. Ertl, and W. Moritz, Surf. Sci. **123**, 129-140 (1982).

[14] K. O. Legg, F. Jona, D. W. Jepsen, and P. M. Marcus, Phys. Rev. B **16**, 5271-5276 (1977).

[15] K. O. Legg, F. Jona, D. W. Jepsen, and P. M. Marcus, Surf. Sci. **66**, 25-37 (1977).

[16] R. S. Saiki, G. S. Herman, M. Yamada, J. California, Berkeley, 1985).

[17] S. Tang, A. J. Freeman, and G. B. Olson, Phys. Rev. B **47**, 2441-2445 (1993).

[18] X. S. Zhang, L. J. Terminello, A. E. S. v. Wittenau, S. Kim, Z. Q. Huang, Z. Z. Yang, D. A. Shirley, F. M. Tao, and Y. K. Pan, (Lawrence Berkeley National Laboratory, 1987).

[19] X. S. Zhang, L. J. Terminello, S. Kim, Z. Q. Huang, A. E. S. v. Wittenau, and D. A. Shirley, J. Chem. Phys. **89**, 6538-6546 (1988).

[20] J. M. V. Zoest, J. M. Fluit, T. J. Vink, and B. A. V. Hassel, Surf. Sci. **182**, 179-199 (1987).

[21] A. J. Freeman and R. Wu, Journal of Magnetic Materials **100**, 497 (1991).

[22] L. H. Bennet and R. E. Watson, (World Scientific, Singapore, 1993).

[23] K. Totland, P. Fuchs, J. C. Groebli, and M. Landolt, Physical Review Letters **70**, 2487 (1993).

[24] J. J. Barton, S. W. Robey, and D. A. Shirley, Phys. Rev. B **34**, 778-791 (1986).

[25] J. J. Barton, C. C. Bahr, S. W. Robey, Z. Hussain, E. Umbach, and D. A. Shirley, Phys. Rev. B **34**, 3807-3819 (1986).

[26] Z. Huang, Ph.D. Thesis (University of California, Berkeley, 1992).

[27] W. R. A. Huff, Y. Zheng, and Z. Hussain, Journal of Physical Chemistry (1994).

[28] J. J. Rehr and R. C. Albers, Physical Review B **41**, 8139-8149 (1990).

[29] Y. F. Chen, W. Wu, and D. A. Shirley, (To be published).

[30] S. D. Kevan, Ph.D. Thesis, (The University of California, Berkeley, 1980).

[31] N. Markinovich, Personal Communication, 1993).

[32] R. Germar, W. Durr, J. W. Krewer, D. Pesdia, and W. Gudat, Applied Physics A **47**, 393-398 (1988).

[33] C. R. Brundle and A. D. Baker, (Academic Press, London, 1978), Vol. 2.

[34] J. J. Yeh and I. Lindau, Atomic Data and Nuclear Data Tables **32**, 1-155 (1985).

[35] S. Tanuma, C. J. Powell, and D. R. Penn, Surf. Interface Anal. **11**, 577-589 (1988).

[36] J. J. Barton, Ph.D. Thesis, (The University of [11]S. R. Chubb and W. E. Pickett, Solid State Commun. **62**, 19-22 (1987).

[37] V. L. Moruzzi, J. F. Janak, and A. R. Williams, *Calculated Electronic Properties of Metals* (Pergamon Press, Inc., New York, 1978).

[38] K. O. Legg, F. Jona, D. W. Jepsen, and P. M. Marcus, Physical Review B **16**, 5271-5276 (1977).

[39] L.-Q. Wang, Z. Hussain, Z. Q. Huang, A. E. Schach von Wittenau, and others., Physical Review B **44**, 13711-19 (1991).

[40] L.-Q. Wang, A. E. Schach von Wittenau, Z. G. Ji, L. S. Wang, and others., Physical Review B **44**, 1292-1305 (1991).

It is not given to human beings, happily for them, for otherwise life would be intolerable, to foresee or to predict to any large extent the unfolding course of events. In one phase men seem to have been right, in another they seem to have been wrong. Then again, a few years later, when the perspective of time has lengthened, all stand in a different setting. There is a new proportion. There is another scale of values. History with its flickering lamp stumbles along the trail of the past, trying to reconstruct its scenes, to revive its echoes, and kindle with pale gleams the passion of former days. What is the worth of all this? The only guide to a man is his conscience; the only shield to his memory is the rectitude and sincerity of his actions. It is very imprudent to walk through life without this shield, because we are so often mocked by the failure of our hopes and the upsetting of our calculations; but with this shield, however the fates may play, we march always in the ranks of honour.

Winston Churchill, Speaking before the

House of Commons

CHAPTER 3

THE STRUCTURAL DETERMINATION OF MNNI AND MNCU SURFACE ALLOYS USING ANGLE-RESOLVED PHOTOEMISSION EXTENDED FINE STRUCTURE AND PHOTOEMISSION HOLOGRAPHY

I. Introduction

Understanding the crystal structure that results from the growth of one metal on the surface of another is one of the most challenging aspects of thin-film growth, with potential applications for magnetic multilayers and for highly reaction-specific catalysts[1]. A number of unusual magnetic phenomena are expected in these two-dimensional structures, including magnetization perpendicular to the surface plane at temperatures above the bulk Curie temperature, and enhanced magnetic moments. These phenomena are critically dependent on the local atomic structure[2-4].

Manganese is an interesting candidate for thin-film growth because of its varied magnetic and structural properties, with four different lattice structures, depending on temperature. The α and the β phases are complex cubic structures with 58 and 20 atoms per unit cell, respectively, while the γ and the δ phases are face-centered cubic and body-centered cubic with nearest-neighbor spacings of 2.73 Å and 2.67 Å respectively[5]. Recently, ultra-thin films of manganese on Ni(100) and Cu(100) have received attention because of the reported existence of stable, surface alloys that form at one-half monolayer (ML) coverage[6-13]. These surface alloys form at or near room temperature and exhibit a c(2x2) low energy electron diffraction (LEED) pattern. LEED I-V studies and some scanning tunneling microscopy (STM) of these two similar systems suggest that the surface alloys are much more corrugated than would be expected from a simple comparison of the hard-sphere radii. However, the STM study by Noh *et al.* disputes the existence of this

corrugation for the copper system[13]. Wuttig *et al.* proposed that the large surface corrugation is driven by the magnetic ordering of the surface Mn atoms[10].

In this study we use Angle-Resolved Photoemission Extended Fine Structure (ARPEFS) to investigate two manganese surface alloys, c(2x2)Mn/Ni(100) and c(2x2)Mn/Cu(100). ARPEFS is a well-proven technique for determining the atomic structure of adsorbates and the near-surface region of the substrate with high accuracy[14-21]. ARPEFS is advantageous in studying these bimetallic systems because it has elemental selectivity through the binding energy of core electrons, because the oscillation amplitudes can be quite large, and because it is spatially accurate, to a few hundreths an Ångstrom. In addition, we used high-energy, angle-scanned, photoelectron diffraction or holography to study the quality of the grown film, because knowledge of the atomic abruptness of the magnetic interface is important for comparing the theoretical to the experimental magnetic properties of these two-dimensional structures. Photoelectron holography allows one to image the atomic symmetry near the emitter directly . High kinetic-energy electrons, with kinetic energy greater than 500 eV, are very strongly scattered in the forward direction along internuclear axes[22, 23]. This scattering preference and the long mean free path of these electrons, make holography especially sensitive to the local symmetry around and especially above the emitter. Of course, for structural determinations that are accurate to much better than one-tenth Ångstrom, one must compare the diffraction data with a multiple-scattering calculation and this is ARPEFS strength.

Lastly, while other researchers have studied this system with LEED, the atomic sensitivity of photoelectron diffraction is especially advantageous for these systems involving metals that have similar atomic numbers. This selectivity allows us to probe the local geometry of the emitter, and thus easily determine where the adatom is in relation to the surface plane. The LEED measurements instead rely on the small differences in scattering factors between Mn and Ni, or Mn and Cu, to make such a determination. As the Fe/Au(100) case shows, one cannot assume that the adatom remains on the substrate surface. This information about these two-dimensional magnetic systems may be critically important.

II. Experimental

The experiments were performed by Jonathan Denlinger and Eli Rotenberg, in an ultra-high vacuum (UHV) chamber with a base pressure of 1×10^{-10} torr. The UHV chamber is equipped with the standard surface-science diagnostic and preparation tools and a high-precision, five-axis, horizontally mounted manipulator that allows the crystal to be heated to 2500 K by electron bombardment. The photon source for these measurements is Beamline 7.0, at the Advanced Light Source (ALS). Beamline 7.0 is an undulator-based spherical-grating monochromator (SGM)

beamline with an energy range from 75 eV to 1200 eV. The photoemission spectra were collected using a Physical Electronics hemispherical, electron energy analyzer which has a 140 mm radius and a 16-element multichannel detector. The angular acceptance of the analyzer lens system is ± 1.0°. It is further described in reference [24].

A schematic of Beamline 7.0 and a sketch of the experimental geometry are shown in Fig. 1. The analyzer is fixed at an angle of 60° from the Poynting vector, and all changes in the measured electron-emission direction were accomplished by rotating the sample. The ARPEFS photoemission data were collected at two different emission angles, normal emission, $\theta = 0°$, and $\theta = 45°$ along the [011] direction. The holography photoemission data were excited with a Mg Kα source. The Mn 2p photoemission signal was then measured in constant-solid-angle steps over a range of polar angles from $\theta = 0°$ to $\theta = 80°$ and azimuthal angles from $\phi = 0°$ to $\phi = 90°$. The sample was at room temperature for all the measurements.

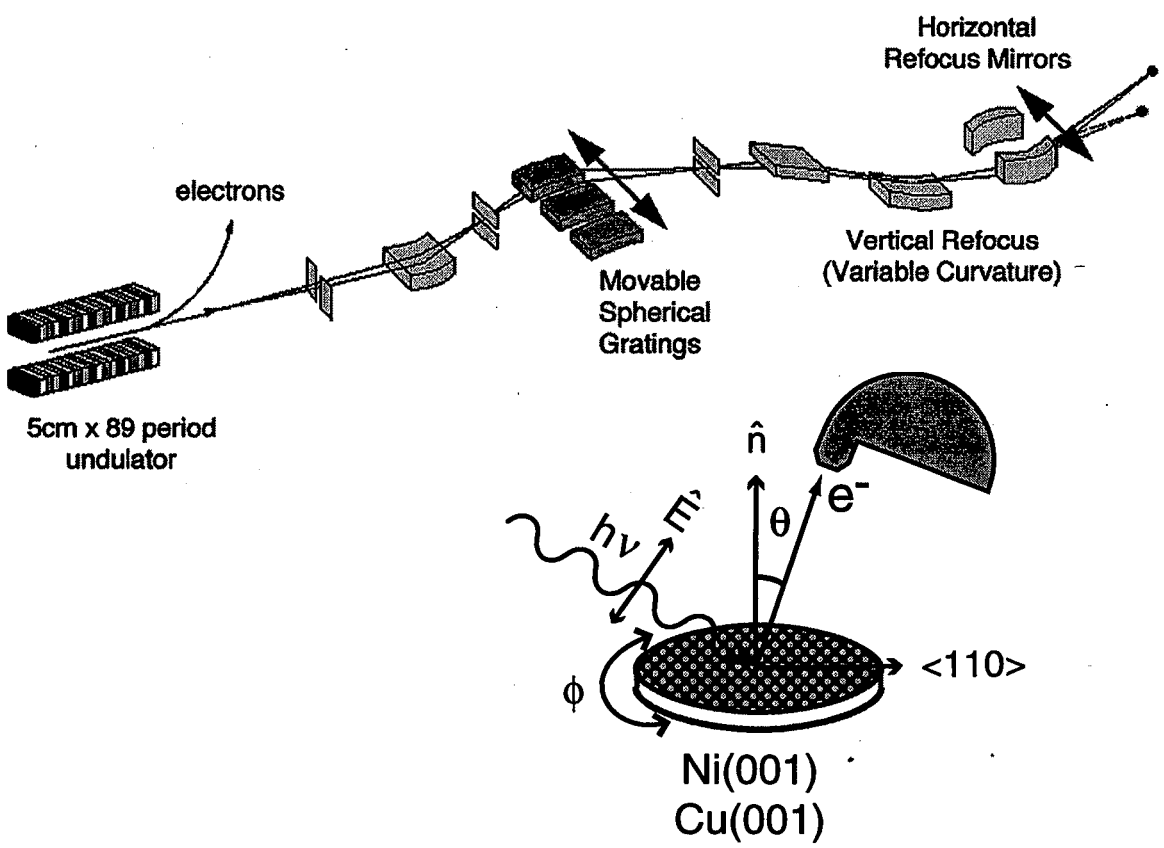

Figure 1. Top panel: optical layout of Beamline 7.0 at the ALS. Bottom panel: Experimental geometry. The angle θ is the polar angle between the emission direction and the surface normal, $\hat{n}$. The azimuthal angle, ϕ is defined as rotation about the surface nornal. The off-normal emission is along the <110> direction. The angle between the analyzer and the light's $\vec{E}$ is fixed at 60°. The light polarization vector is perpendicular the analyzer dispersion direction.

The Ni(001) and Cu(001) crystal were aligned to within $\pm$ 0.5° of the [001] direction with Laue backscattering and then mechanically polished with six μm and one μm diamond paste. Once in vacuum, the crystals were cleaned with repeated cycles of Argon ion sputtering and annealing. The Cu was annealed to 950 K and the Ni to 1100 K. We checked the sample cleanliness with core-level photoemission. Neither crystal had any detectable oxygen contamination and the Cu crystal was also free of any detectable carbon. The carbon signal from the Ni crystal was just out of the background noise, less than one or two *percent* of a monolayer.

The manganese source consisted of 99.99% pure Mn pellets, heated in an alumina crucible, surrounded by a water-cooled jacket. The Mn was evaporated at a rate of ~ 1.0 monolayer per minute with the chamber pressure below 1.5×10^{-9} torr. We monitored the evaporation rate with a quartz-crystal microbalance (QCM) calibrated by comparing the Mn-3p to the Ni-3p photoemission peak intensity ratio for the Ni case and the Mn-3p/Cu-3p ratio for the Cu case. The c(2x2)Mn/Cu(001) sample studied here was prepared by evaporating 1/2 ML of Mn directly onto the Cu(001) substrate at room temperature. No subsequent annealing was necessary to obtain a sharp (2x2) LEED pattern. The crystal was still free of any detectable oxygen or carbon contamination after the Mn evaporation.

In contrast to the Cu case, and to the results reported by other authors, in this study evaporating one-half monolayer onto the Ni substrate at room tempurature, without annealing, never led to a clear c(2x2) LEED pattern[11]. Instead, the c(2x2) Mn/Ni(001) sample studied in this work was prepared by evaporating one monolayer of Mn onto the clean Ni(001) surface at room temperature. The resulting LEED pattern is a fuzzy c(2x2) structure. After annealing the crystal for 30 seconds at 350° C the Mn coverage drops by half and the LEED image sharpens considerably. We assign a value of 1/2 monolayer to this c(2x2) structure. The Mn 3p photoemission-peak intensity supports this assignment (Fig. 2). Following the evaporation there was no detectable oxygen, and the carbon contamination was still less than one to two *percent* of a monolayer.

III. Data Analysis

The experimental ARPEFS data for each sample are two series of manganese 3p angle-resolved photoemission spectra taken at two different emission angles, normal emission and 45 degrees from normal along [011]. In each series the photon excitation energy is varied so that the kinetic energy of the Mn 3p photoelectrons ranges from 90 eV to 450 eV in electron wavevector steps of 0.1 $Å^{-1}$. The conversion from kinetic energy, E_k to wavevector, k, is: $k(Å^{-1}) = 0.512\sqrt{E_k(eV)}$. The total collection time for one series of spectra is approximately 30 minutes. We fitted each of the 65 spectra in each series to extract the most accurate peak intensites with which to construct the diffraction curve, $\chi(k)$. However, because the Mn 3p photoemis-

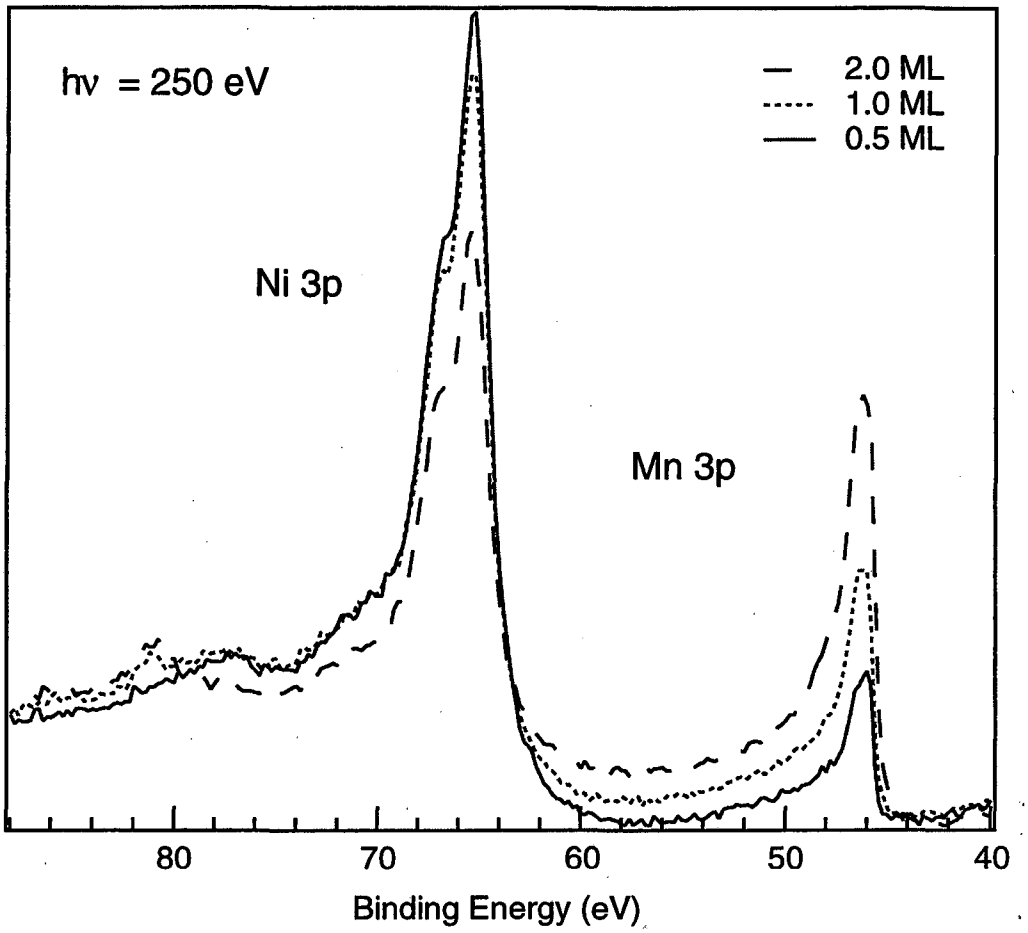

Figure 2. Photoemission spectra for Ni 3p and Mn 3p taken with a photon energy of 250 eV. Solid line 1/2 ML Mn, dotted line 1 ML Mn, and dashed line 2 ML Mn. The 1 ML and 1/2 ML coverage spectra were taken after annealing the 2 ML sample at 350 K for 30 and 60 seconds respectively.

sion 'peak' is a complex manifold of six peaks we developed an empirical lineshape to represent the manifold in the peak fitting routine. This empirical lineshape is a Mn 3p photoemission spectrum taken with very good statistics, scaled to unit peak height, and set to a peak position of zero eV kinetic energy. Using an empirical lineshape allows us to obtain accurate peak intensities, while saving considerable time in the fitting process. The Mn 3p peak intensites are extracted by fitting each spectra in the series with this lineshape and a linear background. We take the amplitude of the lineshape as the measure of the photoemission intensity. The Mn 3p lineshape is significantly broader for the Cu sample than for the Ni sample, and we used a different lineshape for each sample in the fitting routine. We will address this lineshape difference in Section IV.

The intensity of each Mn 3p peak in the series plotted against the electron wavevector, k, is denoted as I(k). This function I(k) has two components; a slowly varying, atomic-like portion, $I_0(k)$, upon which is superimposed a rapidly oscillating beat pattern that arises from interference between the primary wave propagat-

ing directly to the detector, and waves that scatter elastically off nearby atomic potentials before they reach the detector. The experimental and calculated diffraction curves, $\chi(k)$, are obtained by removing the slowly varying $I_0(k)$ portion from I(k).

$$\chi(k) = \frac{I(k) - I_0(k)}{I_0(k)} \tag{1}$$

We construct $I_0(k)$ in two steps, designed to eliminate the low frequency oscillations in I(k). The first step is to create an intermediate $I_0(k)$ consisting of seven points. The first and seventh points are the first and last points of I(k). The five points in between the first and seventh are calculated by dividing I(k) into five sections of equal length in electron wavevector, k. The average value of I(k) in each of these five sections is one of the five points in the intermediate $I_0(k)$. In the second step we set $I_0(k)$ equal to the fit of a cubic spline through the seven points making up the intermediate $I_0(k)$. For consistency this routine is automated and used for both the experimental and calculated data. The resulting $\chi(k)$ curves for each sample in the two emission directions are shown in Figs. 3 and 4.

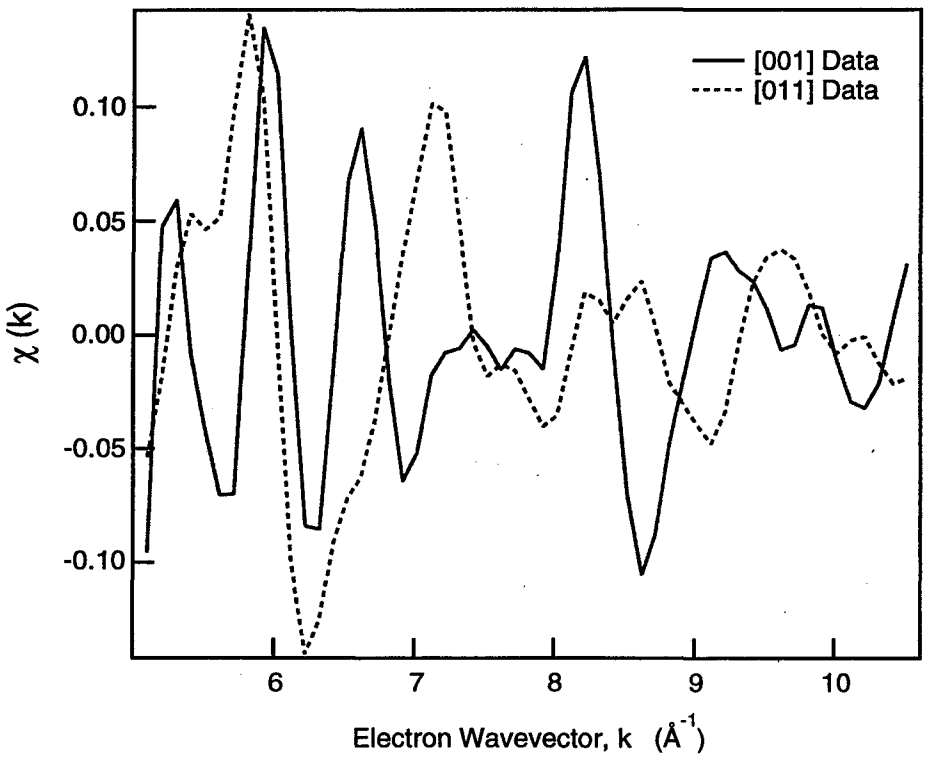

Figure 3. Experimental Mn 3p c(k) curves for the [001] and [011] emission directions from c(2x2)Mn/Ni(001).

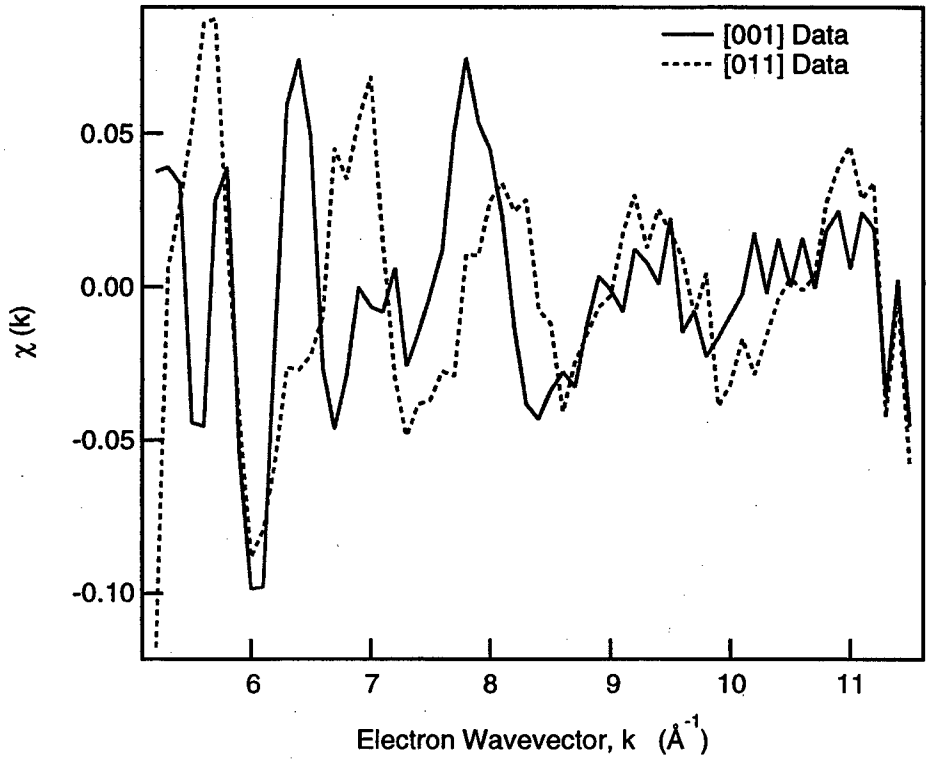

Figure 4. Experimental Mn 3p c(k) curves for the [001] and [011] emission directions from c(2x2)Mn/Cu(001).

The intrinsic features that make up the overall Mn 3p peak shape will exhibit the same ARPEFS oscillations as the peak centroid. That is, each peak has the same $\chi(k)$ curve, but they are shifted in k-space by the differences in their binding energy. The electron kinetic energy is related to the electron wavevector by: $k(\text{Å}^{-1}) = 0.512\sqrt{E_k(\text{eV})}$. Differentiating this expression gives: $dk/dE_k = 0.131/k$. For a lineshape 10 eV wide, at a k-value of 5.0 Å^{-1} the photoelectrons at the highest and lowest kinetic energies differ by 0.262 Å^{-1}. If $\chi(k)$ varies rapidly over this range of k-values then the contributions from widely separated regions of the lineshape will tend to cancel out sharp maxima and minima in $\chi(k)$. The smaller than normal oscillations in the experimental $\chi(k)$ curves could be due to this effect. To test for this effect in our data reduction, we extracted $\chi(k)$ curves from the Mn/Cu(001) data set in a second manner. In this second procedure, we divided each individual Mn 3p spectra into four separate, 1.6 eV wide sections. The I(k) from each of these sections is the area of that section divided by the area of a 1.6 eV wide section on the high-binding-energy side of the peak. The $\chi(k)$ curves derived from these four sections are labeled for the binding energy at the center their respective integration windows. Fig. 5 shows a typical spectrum and fit as well as the four windows used to obtain the other $\chi(k)$ curves by the second method.

The $\chi(k)$ curves for the Mn/Cu(001) case obtained by the second method Fig. 6. The $\chi(k)$ curve derived from the area around the peak center, Chi48, is

nearly identical to the $\chi(k)$ curve derived with the lineshape method, ChiLS. The curves from peaks farther from Mn 3p centroid than Chi48 are shifted to lower k-values as expected. These other $\chi(k)$ curves are very similar to ChiLS, except that Chi54 has oscillations that are nearly twice as large as ChiLS. The $\chi(k)$ curves extracted from sections closer to the tail of the Mn 3p peak are noisier due to the poorer statistics in this section of each spectra. We note that the Mn 3p peak from the c(2x2)Mn/Cu(001) sample is much broader than that from the similar Ni(001) sample. This broader peak suggests Mn atoms in different chemical environments and the difference may account for the difference in the $\chi(k)$ curves derived from different parts of the 3p lineshape. However, Chi48, obtained with the second method agrees very will with ChiLS obtained with the lineshape method. The relatively $\chi(k)$ small oscillations are not an artifact of the peak fitting method. We will use ChiLS throughout this paper for comparisons to the mulitple-scattering calculations.

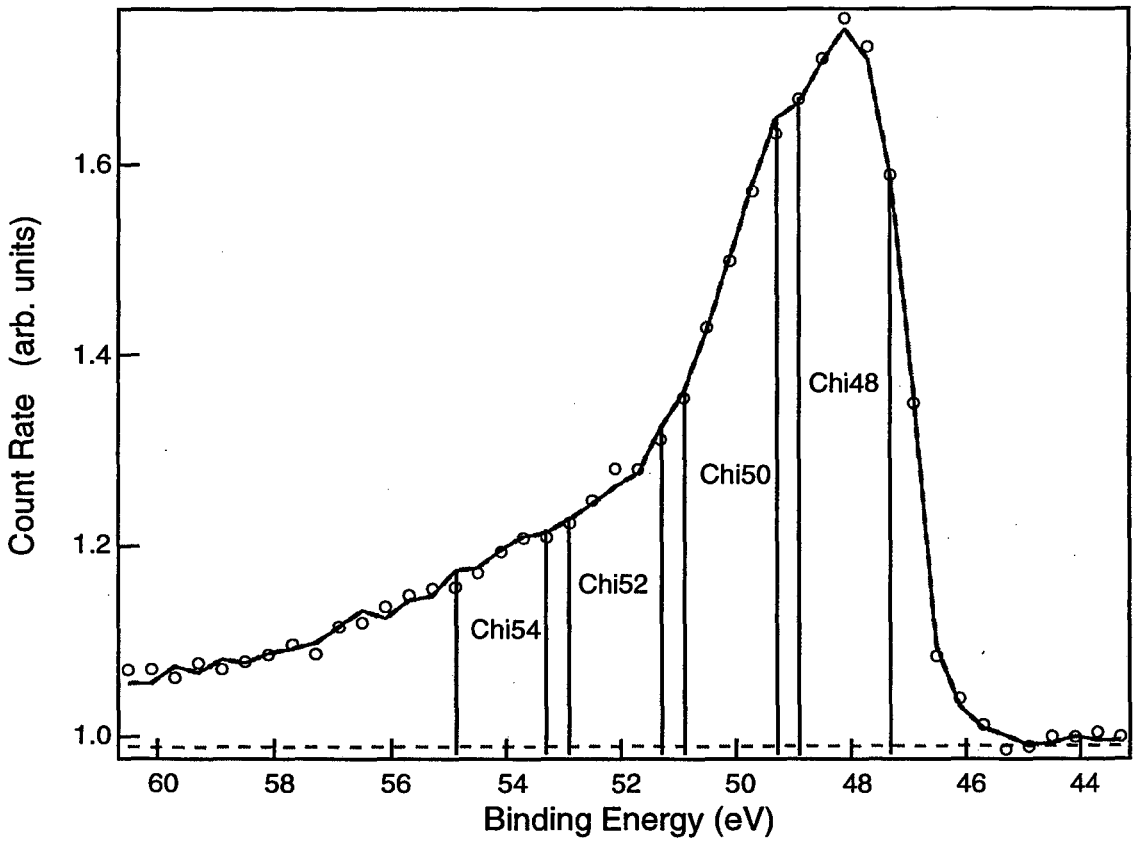

Figure 5. Experimental data (open circles) and fit (solid line) for the c(2x2) Mn/Cu(001) Mn 3p photoemission peak. The compontents of the fit are shown as dashed lines. The windows used to derive the other c(k) curves are shown and labeled by the value of the binding energy at their center.

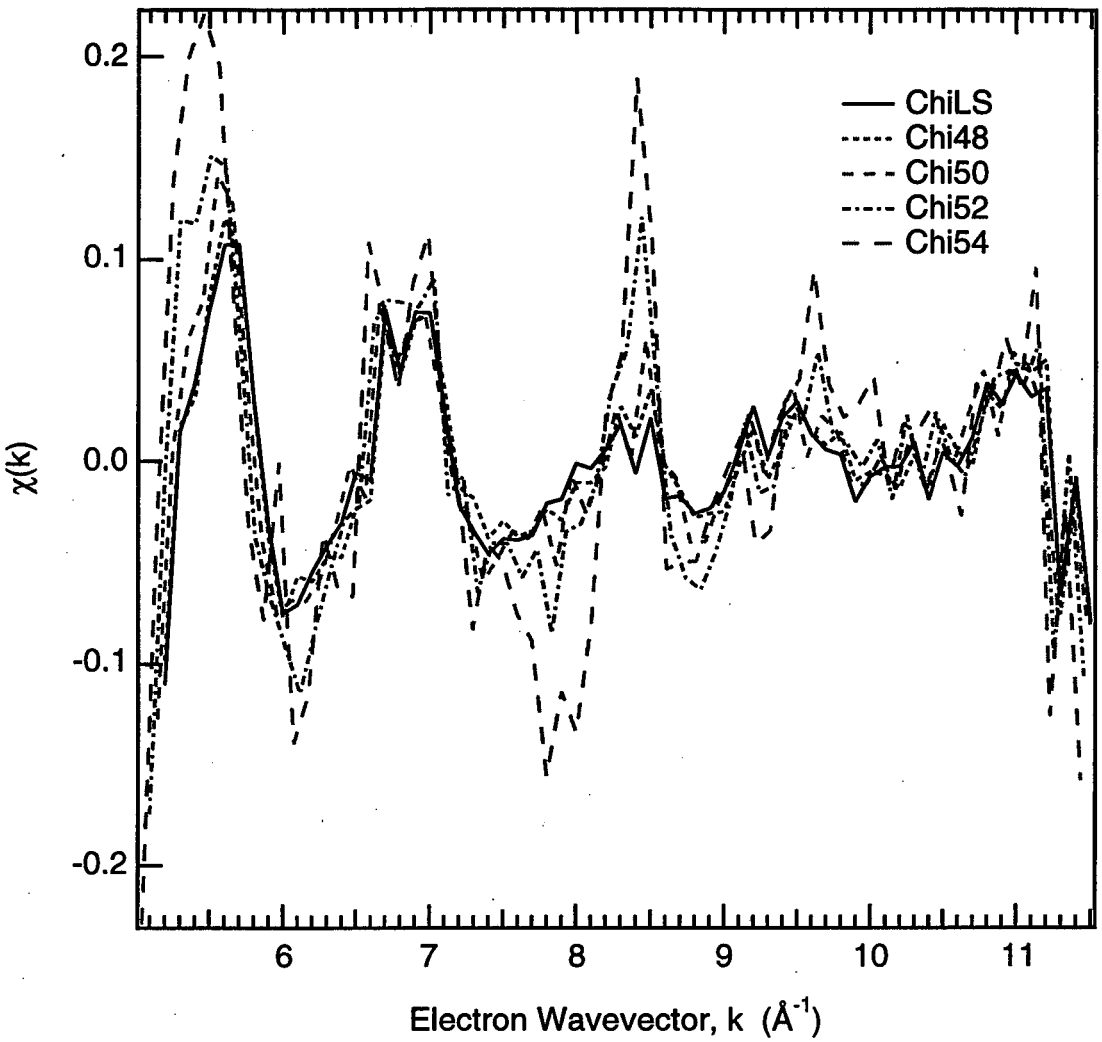

Figure 6. Comparison of the c(k) curves derived from the lineshape fitting method and the c(k) curves derived by measuring the areas of the photoemission peak in a small energy window. The name of each c(k) curve is based on the binding energy at the center of the energy window. (Fig. 5)

We performed multiple-scattering spherical-wave (MSSW) calculations to model the experimental $\chi(k)$ curve data and determined the adsorption site and interlayer spacings of the near-surface layers. The calculation program, based on the Rehr and Albers formalism, was developed by our group and is optimized for obtaining a best fit to experimental energy-dependent $\chi(k)$ data[25, 26]. This program uses second-order matrices and up to eighth-order scattering to produce a convergent calculation at the electron energies used in ARPEFS. The best fit is determined by the A-factor:

$$A = \frac{\sum\left(\chi_c - \chi_e\right)^2}{\frac{1}{2}\sum\left(\chi_c^2 + \chi_e^2\right)} \tag{2}$$

which is useful in the fitting routine when the fit is far from the minimum because the A-factor emphasizes the structurally important periodicity of the $\chi(k)$ curve over the intensity of the peaks. The conventional R-factor is given by

$$R = \frac{\sum(\chi_c - \chi_e)^2}{\sum \chi_e^2} \tag{3}$$

When the fit is close to the minimum the two factors are functionally equivalent and the best fit occurs at the minimum of both the A-factor and R-factor. We shall report the conventional R-factor throughout this paper[15].

This MSSW calculation requires both structural and non-structural input parameters. As an initial guess for the fitting procedure we used the structural parameters from the LEED I-V analysis[9]. The non-structural parameters include the initial state, the atomic scattering phase shifts, the crystal temperature, the inelastic mean free path, the emission and light polarization directions, the electron analyzer acceptance angle, and the inner potential.

The atomic scattering phase shifts were calculated using the atomic potentials tabulated by Moruzzi *et al.*[25]. The emission and light polarization directions and the analyzer acceptance angle were set to the experimental values described previously in section II. The inelastic mean free path was included using the exponential damping factor $e^{-\frac{t}{\lambda}}$ where λ was calculated using the Tanuma, Powell, and Penn (TPP-2) formula[27]. To account for the vibrational effects of the bulk and surface atoms, the mean square relative displacement was calculated and the correlated surface Debye temperature was set to 375 K for Ni and 325 for Cu. The MSSW results reported here are for a normalized $\chi(k)$ curve calculated with a 95-atom cluster and a 0.8% pathcut. The pathcut is defined as a percentage of the most intense scattering event in the calculation. Scattering events with intensities less than the pathcut value are excluded from the calculation, saving considerable memory and calculation time. Obviously the calculation is more accurate if one includes all scattering events, but we have found that a pathcut of about 1% is sufficient for these systems.

The experimental $\chi(k)$ curve oscillations for both samples are unusually small, only about $\pm 10\%$. The small oscillation size necessitates that we use a normalized $\chi(k)$ in all the fitting calculations. Normalized $\chi(k)$ is defined in terms of the experimental $\chi(k)$ in Eqn. 3, where χ_e and χ_c are the experimental and calculated $\chi(k)$ curves and N is the number of data points.

$$\frac{1}{N}\int \chi_c^2 dk = \frac{1}{N}\int \chi_e^2 dk \tag{4}$$

We will address the reason for the small oscillations in Section IV.

The holographic data are shown as stereographic projections of the Mn 2p angle-resolved photoemission peak intensity. During the data collection the emission angle is varied in constant solid angle steps from a polar angle of $\theta = 0°$ to $\theta = 80°$ and an azimuthal angle from $\phi=0°$ to $\phi = 90°$. The peak intensity at each of the 650 different angles is determined by averaging the intensity over a small kinetic energy window about the peak centroid divided by the average intensity of the same size window on the high kinetic energy background. It is not necessary to fit each peak in the spectrum because we are using a constant photon energy so the peak shape should be constant. This intensity map is then symmetrized to produce the full 360° data. The data collection time for each hologram is less than 45 minutes. The electron kinetic energy for the holographic image is 635 eV, $k = 12.5$ Å^{-1}, high enough to be into the regime where forward focusing is the dominant scattering process[22, 23] (Fig. 7).

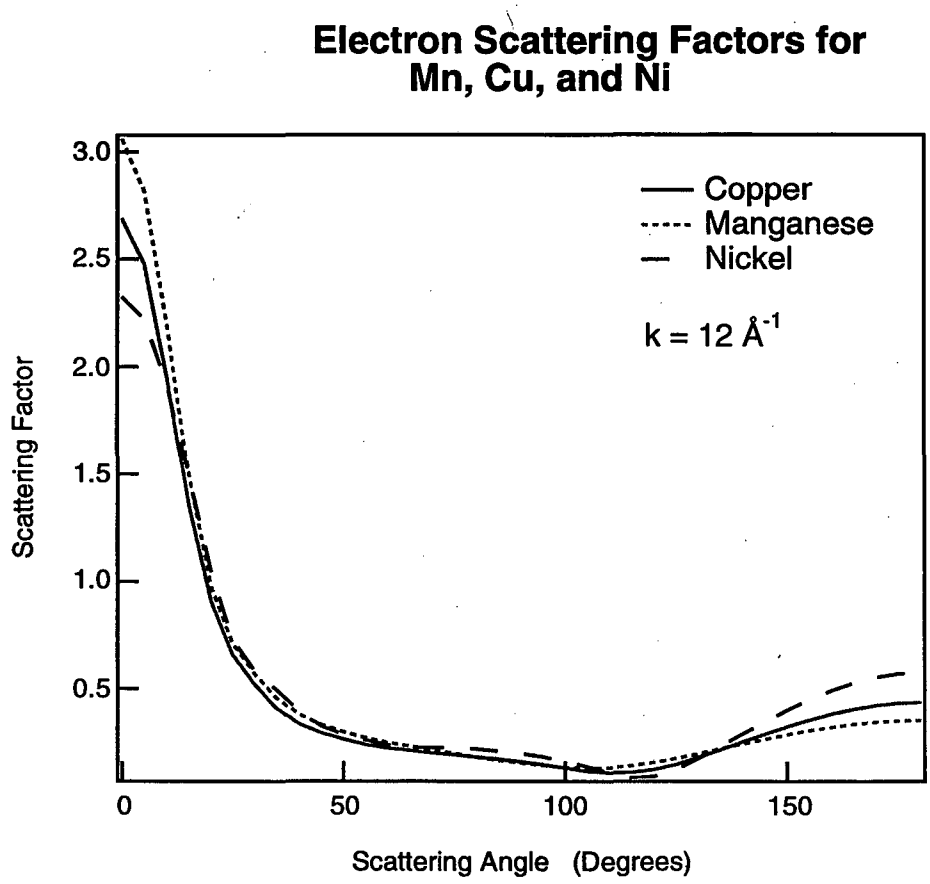

Figure 7. Electron scattering factors *vs.* scattering angle for Cu (solid line), Mn (dotted line), and Ni (dashed line) at a kinetic energy of 550 eV, $k = 12$ Å^{-1}. Note the scattering preference for the forward direction at this high-kinetic energy.

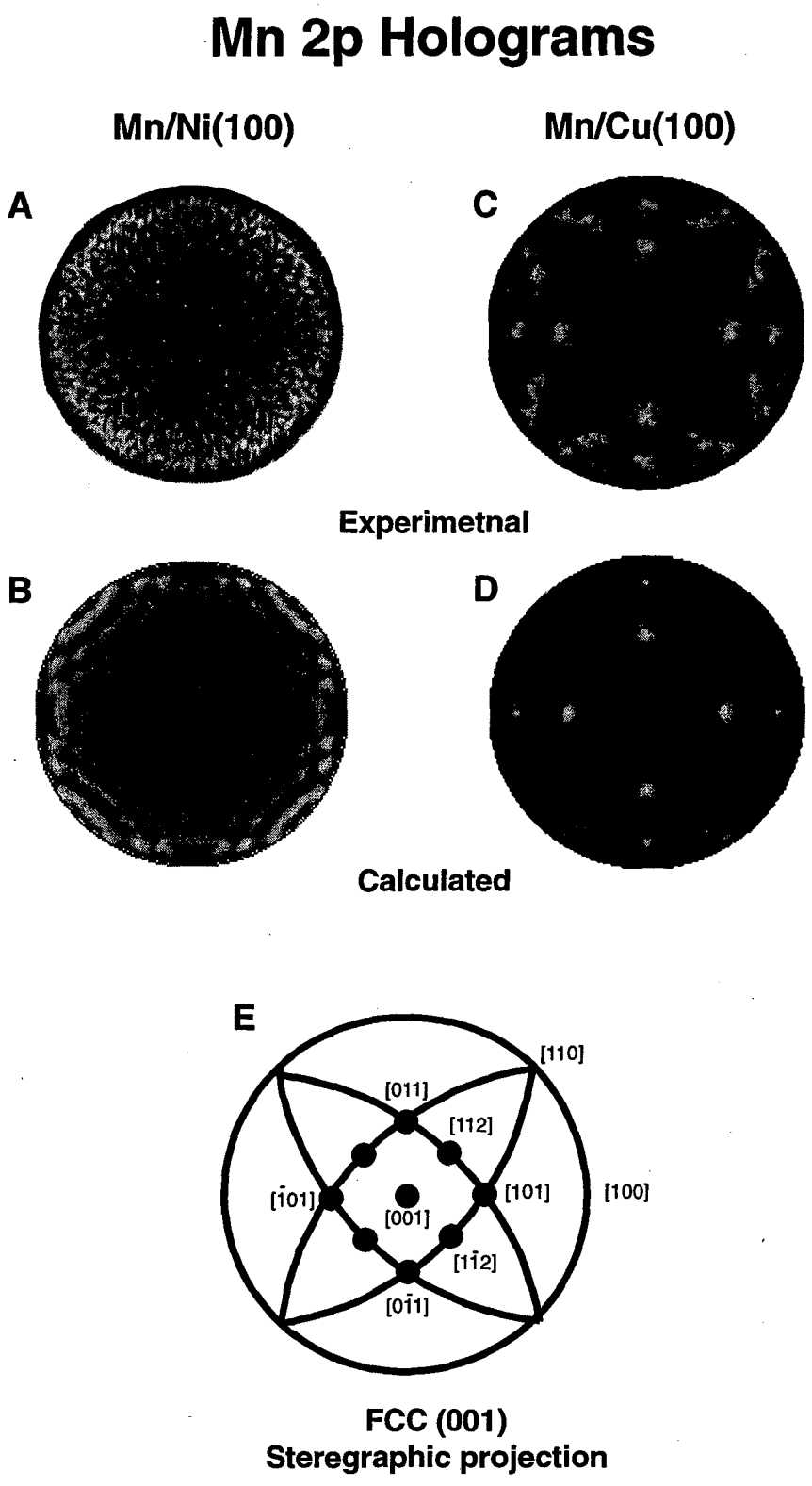

Figure 8. Experimental and calculated holograms for the MnNi and MnCu surface alloys. A) c(2x2) Mn/Ni(001) experimental data. B) Calculated hologram for the surface alloy. C) c(2x2) Mn/Cu(001) experimental data. D) Calculated hologram for the surface alloy with a Mn emitter in the second layer. E) Stereographic projection for the FCC(001) surface

For comparison to the experimental data we calculated the holograms at this kinetic energy for both samples. The model for the Ni sample is a c(2x2) surface alloy, while for the Cu sample the model is the surface alloy with a second layer Cu atom replaced by a Mn atom emitter. The calculated and experimental holograms are shown in Fig. 8. We used a 95-atom cluster with a 0.8% pathcut for these calculations, computing the interferogram over the same angular range as the experimental data.

IV. Results and Discussion

While the LEED patterns for both samples are c(2x2), the holograms immediately show that the two systems are quite different, The four intensity maxima at about 45° polar angle in the c(2x2)Mn/Cu(001) sample must be from subsurface Mn, Fig. 7C. These peaks are at positions marking the family of (011) crystal planes. The stereographic projection for the (001) face of a face-centered-cubic (FCC) crystal is depicted in Fig. 7E for comparison. These four intensity maxima in Fig. 7C are due to the forward scattering of the photoelectrons from an emitter one layer below the surface along the [011] crystal planes. Osterwalder *et al.* have shown that holography intensity maxima at these positions are due to emitters one layer below the surface. We have independently confirmed this, as shown in Fig. 7D. This figure is the calculated hologram for the c(2x2) Mn/Cu(001) surface-alloy structure determined by LEED, but with a second-layer copper atom replaced by a manganese-atom emitter. The calculated hologram shows excellent agreement with the experimental data, showing that some Mn leaks into the second substrate layer during the sample preparation.

We can also use the the forward-focusing peaks in the Mn/Cu(001) hologram to estimate the corrugation of the surface layer. The angular position of the forward-focusing peaks is determined by the distance of the atom from the emitter. Fig. 9 shows the calculated intensity profiles for polar-angle scans along two perpendicular azimuths for the Mn/Cu(001) system. We performed these calculations for eight surface-corrugation values from 0.0 Å to 0.7 Å. The extremes are shown in the figure. Fig. 9 also shows the sum of these two intensity profiles. The sum of the polar-angle scans over perpendicular azimuths simulates the domain averaging of the experimental data. The angular position of these peaks corresponds to the amount of surface corrugation. We label the double peak near 45° 'Peak1' and the less intense peak near 65° 'Peak2'. We derive the position of Peak1 by fitting a single gaussian to the double peak structure of the sum curve. The Peak2 position is the maximum of the sum curve. In Fig. 10 we plot the position of Peak1 and Peak2 *vs.* the surface corrugation. In the experimental hologram, Peak 1 is at θ = 42.6° and Peak2 is at θ = 67.6°. Comparing the experimental peak positions to the curves shown in Fig. 10 we estimate the surface corrugation is between 0.34 Å and 0.38 Å.

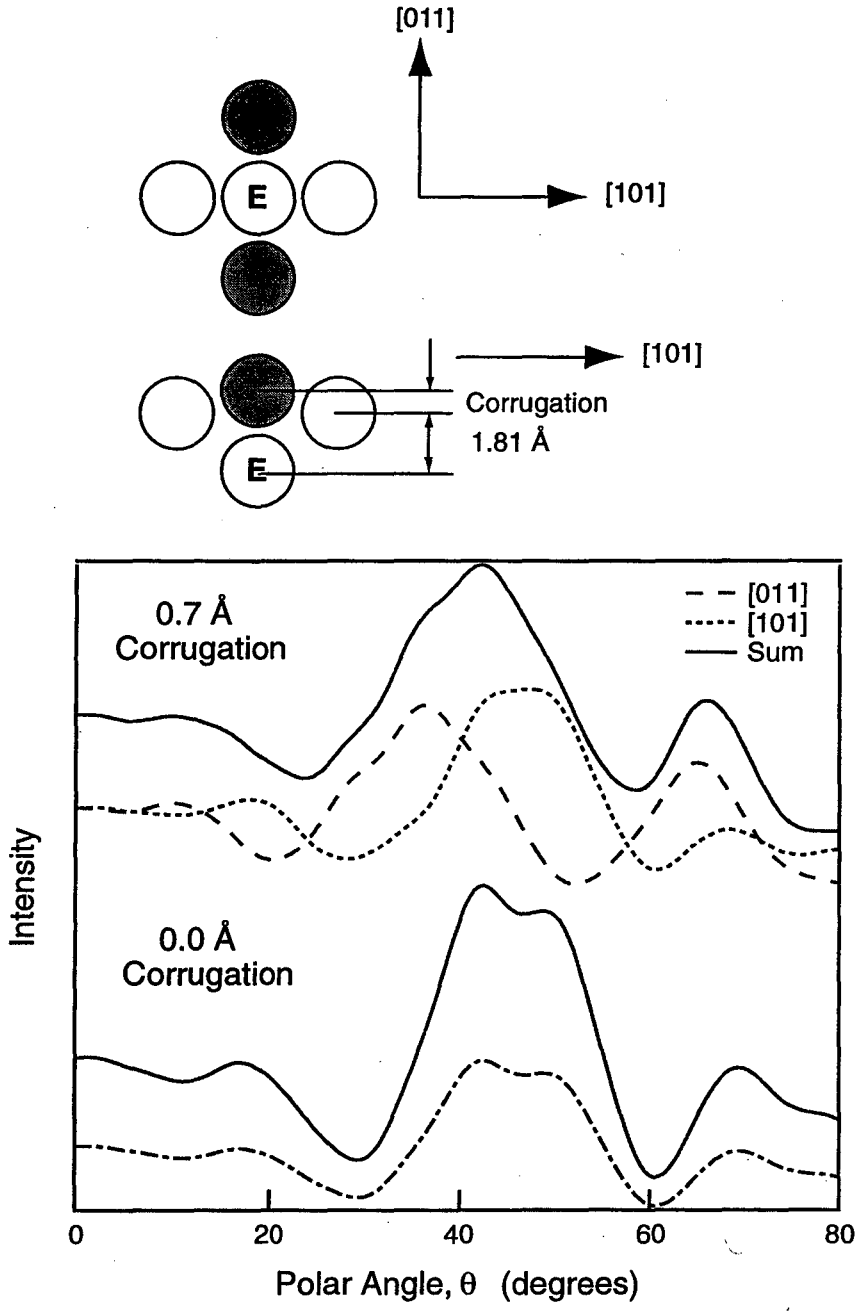

Figure 9. Top panel: Calculation geometry for Mn/Cu(001) surface alloy. The corrugation varies from 0.0 Å to 0.7 Å. Bottom panel: Polar angle scans along the [011] azimuth (dashed line) and the [101] azimuth (dotted line). The solid line is the sum of the two azimuths to simulate domain averaging. The corrugation on the bottom is 0.0 Å and on the top it is 0.7 Å.

The Mn on Ni(001) hologram has no forward-focusing peaks, only broad, weak features at large polar angles, Fig. 7A. This intensity on the outer ring of the hologram is from in-plane scattering, which should be quite weak at these electron energies. Again guided by the LEED analysis, we calculated the hologram for the c(2x2)Mn/Ni(001) surface alloy and this is shown in Fig. 7B. This calculation also

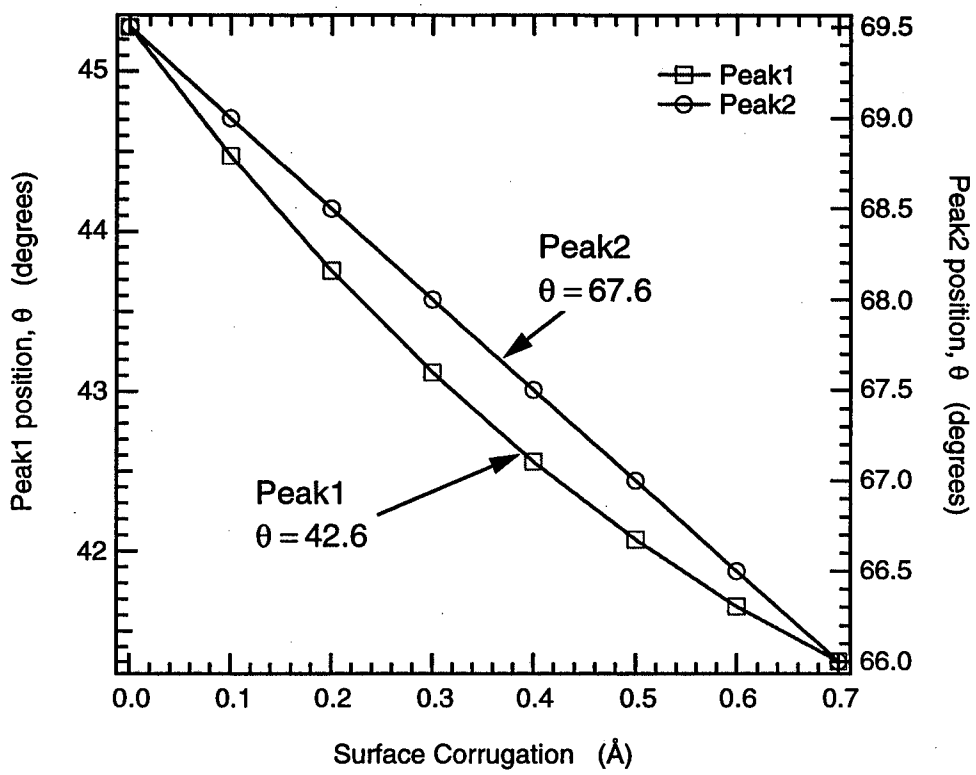

Figure 10. Calculated peak position of the forward focusing peaks *vs* the surface corrugation. The forward focusing peaks in the experimental hologram are labeled in the figure as Peak1 and Peak2.

agrees very well with the experimental data, indicating the absence of adatom Mn below the surface plane. The holographic information suggests that the growth mechanism for the two alloys is quite different.

The Mn 3p photoemission spectra also support this interpretation of the hologragraphic data. Fig. 11 shows the Mn 3p lineshapes for Mn on Ni(001) and Mn on Cu(001). The Mn 3p line from the Cu sample is clearly wider than the nickel sample and appears to have two components. The width of the Mn 3p peak on the Cu sample suggests that there may be two chemically inequivalent Mn sites on the copper sample, namely the surface alloy position and the bulk position. However, from comparison with the 3p lineshape on Ni, the splitting for the Cu case is approximately 2 eV. This splitting is much larger than any reported bulk-surface core level shift. For example, the tungsten 4f bulk and surface peaks are split by *ca.* 300 meV. The reason for the large splitting may be that the two Mn sites are in different magnetic states. A recent total-energy calculation by Wuttig *et al.* found that a ferromagnetic surface had a much lower energy than the paramagnetic surface, and that surface corrugation of the alloy is driven by this Mn ferromagnetic state[10]. The same study also found that for Mn trapped in bulk Cu the paramagnetic state was lowest energy state. The differences between the Mn 3p lineshape for the c(2x2)

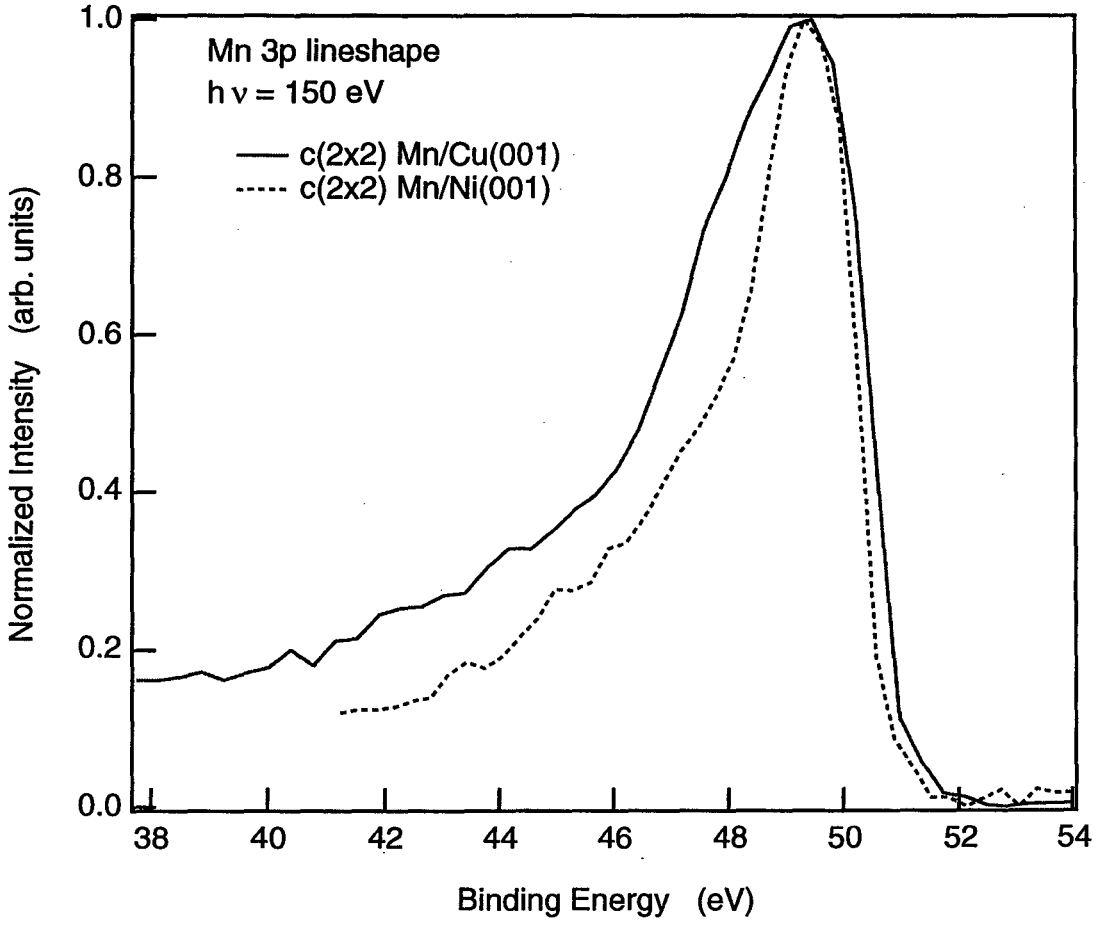

Figure 11. The Mn 3p lineshape from the c(2x2) Mn/Cu(001) sample (solid line and from the c(2x2) Mn/Ni(001) (dashed line). The Mn 3p peak from the Cu sample is significantly broader than that from the Ni sample, suggesting chemically inequivalent adsorption sites on the Cu sample.

Mn/Ni(001) phase and c(2x2) Mn/Cu(001) phase are consistant with the interpretation that the surface Mn for both Ni and Cu is ferromagnetic and that for the Cu the second Mn 3p component, at higher binding energy, is paramagnetic.

While the holography data can tell us about how the overlayer grows and the local atomic symmetry, to accurately determine the atomic structure we must fit the ARPEFS (scanned-energy) data with multiple scattering calculations. There are several possible Mn adsorption sites for a c(2x2) LEED structure on the (100) surface; the surface alloy with the Mn adatom slightly above the substrate surface plane, the surface alloy with the adatom slightly below the substrate surface plane, or the case of an overlayer with the Mn in the four-fold hollow of the substrate. We performed simultaneous best-fit MSSW calculations to both emission angles for each of the three sites. Of course, the Mn could also adsorb to an atop or a bridge

site on the (001) surface, but these are very high-energy and unlikely sites for metal adsorbates. They are also unlikely in light of the holography data. We did fit the diffraction data to models for these sites but the fits were so poor that we will not discuss them further. During the fitting procedure we allowed the surface corrugation, the spacing between the surface and second-layer substrate atoms and the spacing between the second and third-layer substrate atoms as well as the inner potential to vary. Figs. 12 and 13 show the best fit results for each of these sites compared with the c(2x2)Mn/Ni(001) experimental data. Table 1 summarizes the

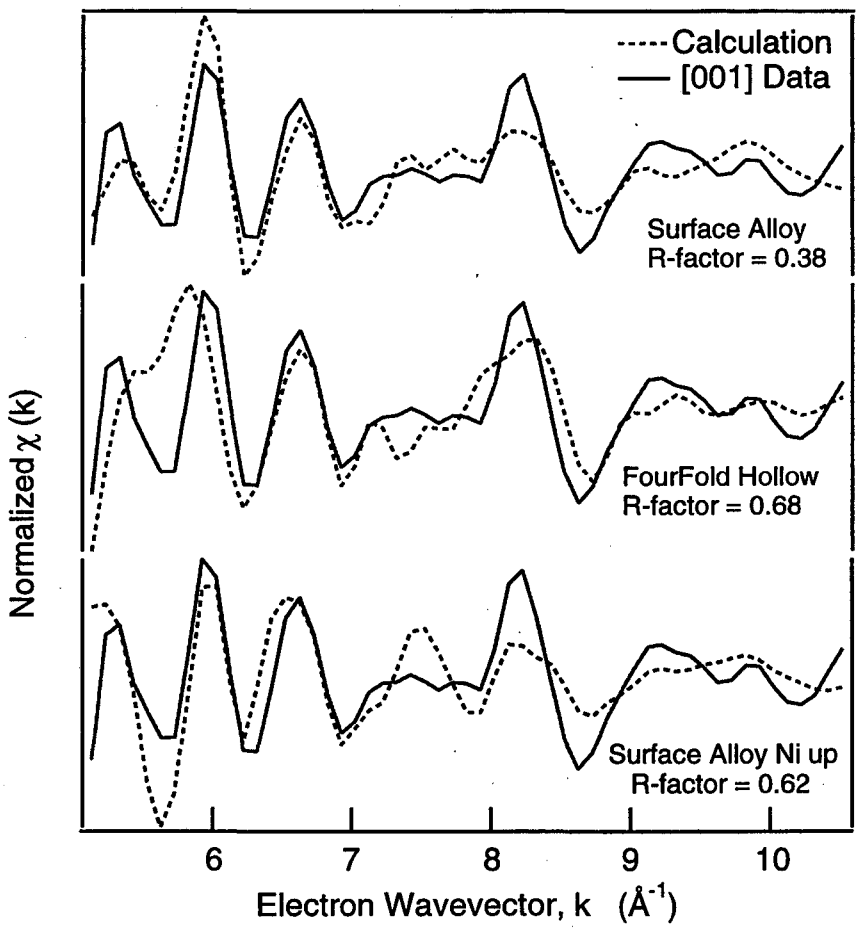

Figure 12. Comparison of the MSSW best fit calculations to the [001] emission data for three different adsorption sites. The surface alloy is the best fit with an R-factor equal = 0.38

R-factors and fit values for the three adsorption sites. The surface alloy with the Mn 'up' is clearly the best fit to the experimental data with an R-factor of 0.38. Although the R-factors for the other two sites are nearly twice that of the surface alloy, visually the fit looks pretty good. One would expect this because the scattering geometry for the three cases is similar. However, as Table 1 shows, the fit pa-

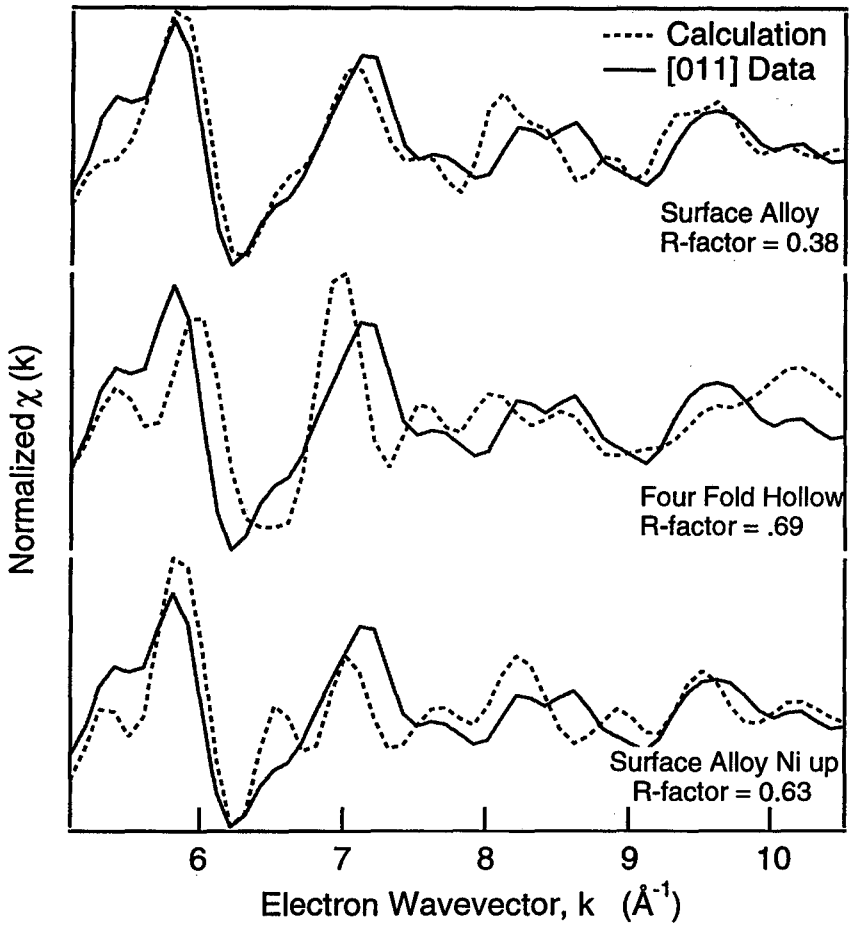

Figure 13. Comparison of the MSSW best fit calculations to the [011] emission data for three different adsorption sites. The surface alloy with Mn above the surface Ni plane is the best fit with an R-factor = 0.38

rameters for these other models are not reasonable and we find that the surface alloy is the best structural model for c(2x2) Mn/ Ni(001).

From the best-fit results the surface-alloy corrugation is 0.24 $\pm$ 0.02 Å with the Mn atoms above the plane of the Ni atoms. The interplaner spacing between the surface-alloy Ni atoms and the second-layer Ni atoms is 1.80 $\pm$ 0.02 Å; this is a 2% expansion from the bulk value of 1.76 Å. The spacing between the second and third layer atoms is 1.78 $\pm$0.04 Å; this is the bulk value within our error limits. The best-fit value for the inner potential is 4.6 V. Fig. 14 shows the atomic model for the c(2x2) Mn/Ni(001) system.

For the MnCu-surface alloy we performed fits to a structural model with some of the second-layer Cu replaced by Mn, in addition to fitting with the same models described above for the Ni case. A schematic of the first two layers of this cluster

Table I. Best fit parameters and the associated R-factor for the three adsorption sites examined. The surface alloy structure with the Mn above the plane of the surface Ni layer is clearly the best fit with an R-factor of 0.38

Adsorption Site	Mn-Ni1 (Å)	Ni1-Ni2 (Å)	Ni2-Ni3 (Å)	R-factor
Surface Alloy	0.24 ± 0.02	1.80 ± 0.02	1.78 ± 0.04	0.38
Four-fold Hollow	0.72	1.60	1.28	0.69
Surface Alloy Ni up	0.21	2.05	1.75	0.62

The Bulk Ni interlayer spacing is 1.76 Å

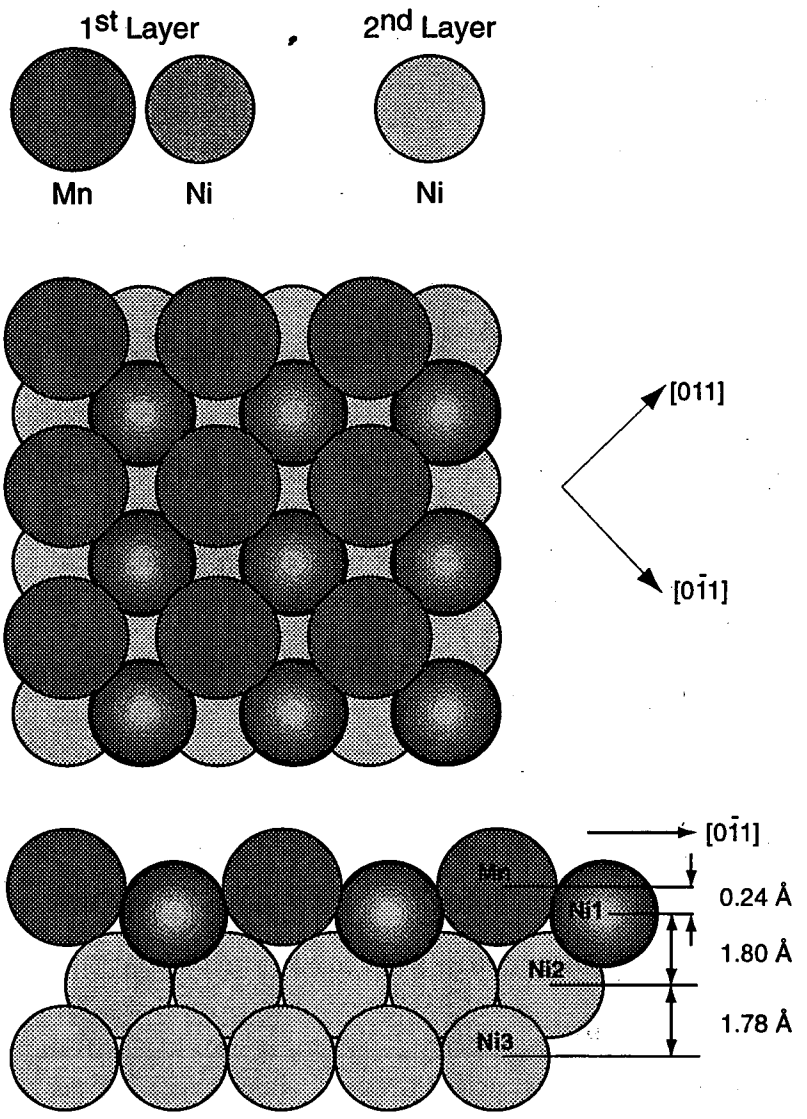

Figure 14. Atomic model of the c(2x2) Mn/Ni(001) structure determined by the present ARPEFS study.

model with a Mn emittier in the second layer is shown in Fig. 15. The second layer is 25% Mn. Again both emission angles were fitted simultaneously. The $\chi(k)$ curves

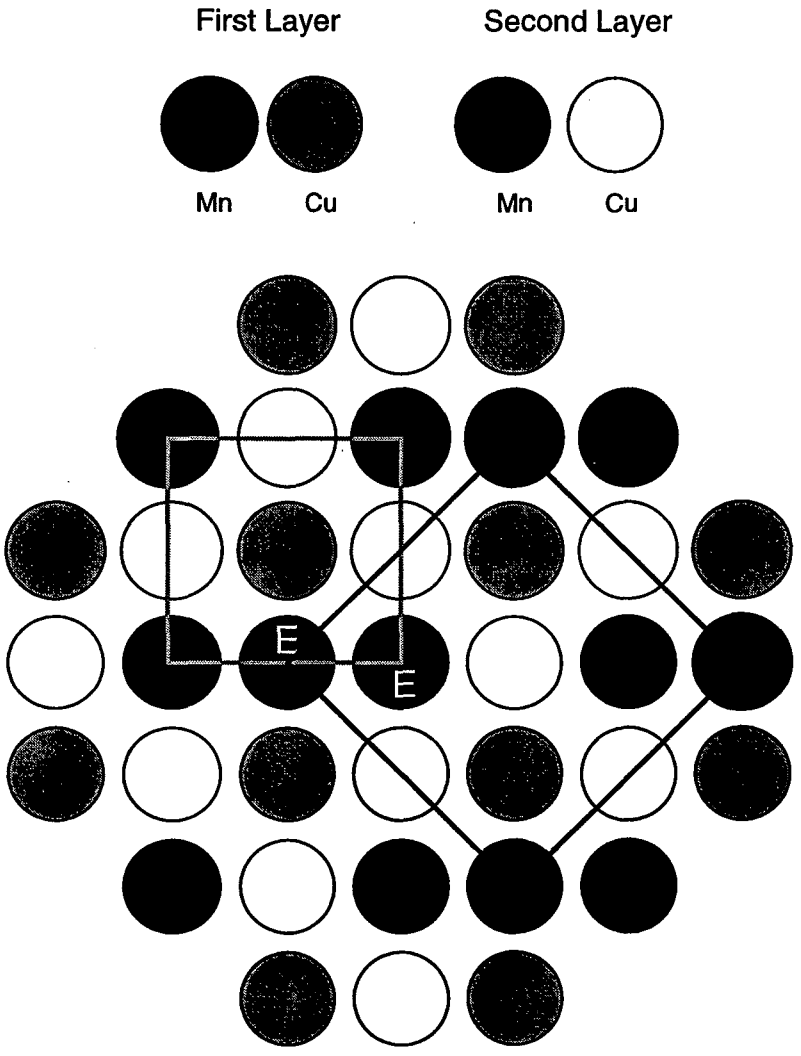

Figure 15. The top two layers of the calculation cluster for c(2x2) Mn/Cu(001) showing the position of the Mn emitters (labeled 'E') in the first and second layers. The light gray line marks the unit cell for the top layer and the heavy black line shows the unit cell for the second layer.

are very weak and noisy, especially at high k-values(Fig. 4). This is due to the fact that the Cu Debye temperature is close to room temperature. To remove the noise from the signal we Fourier filtered the $\chi(k)$ data, removing path length differences (PLD) greater than 15 Å. This filtering process was used because any PLD greater than 15 Å would be the result of several scattering events and would be a very minor part of the overall $\chi(k)$ signal intensity. The best fits as well as the filtered data for both emission angles are shown in Figs. 16 and 17. The best fit as deter-

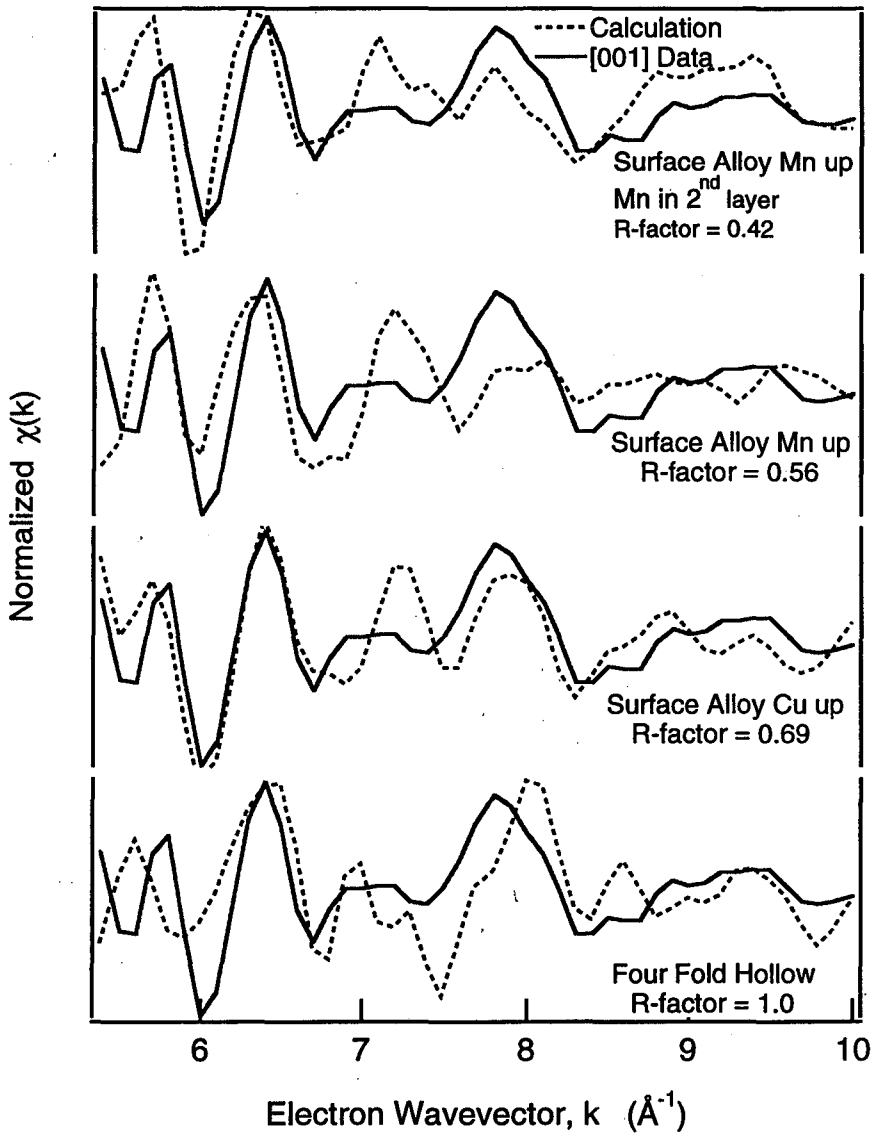

Figure 16. Comparison of the MSSW best fit calculations to the [001] emission data for different adsoption geometries. The surface alloy with the Mn up out of the surface Cu plane and subsurface Mn is the best fit with an R-factor equal = 0.42

mined by the R-factor is for the surface alloy with the Mn above the Cu surface plane and 25% of the second layer Cu replaced by Mn. The R-factor is 0.42. The other structural models give fits with comparable R-factors, but these best fit parameters are not very reasonable. Table II summarizes these results. The next best fit is for the surface alloy with the Mn up, but no subsurface Mn. Clearly these fit parameters do not make sense. Firstly, the inner potential wants to go to zero or below which is obviously unphysical. Secondly, the spacing between the alloy layer and second layer is 1.65 Å. This interlayer spacing is a 9% contraction from the bulk value, while the next layer is expanded 3% from the bulk value. It seems unlikley that the first-Cu layer should be so contracted. This contraction is even

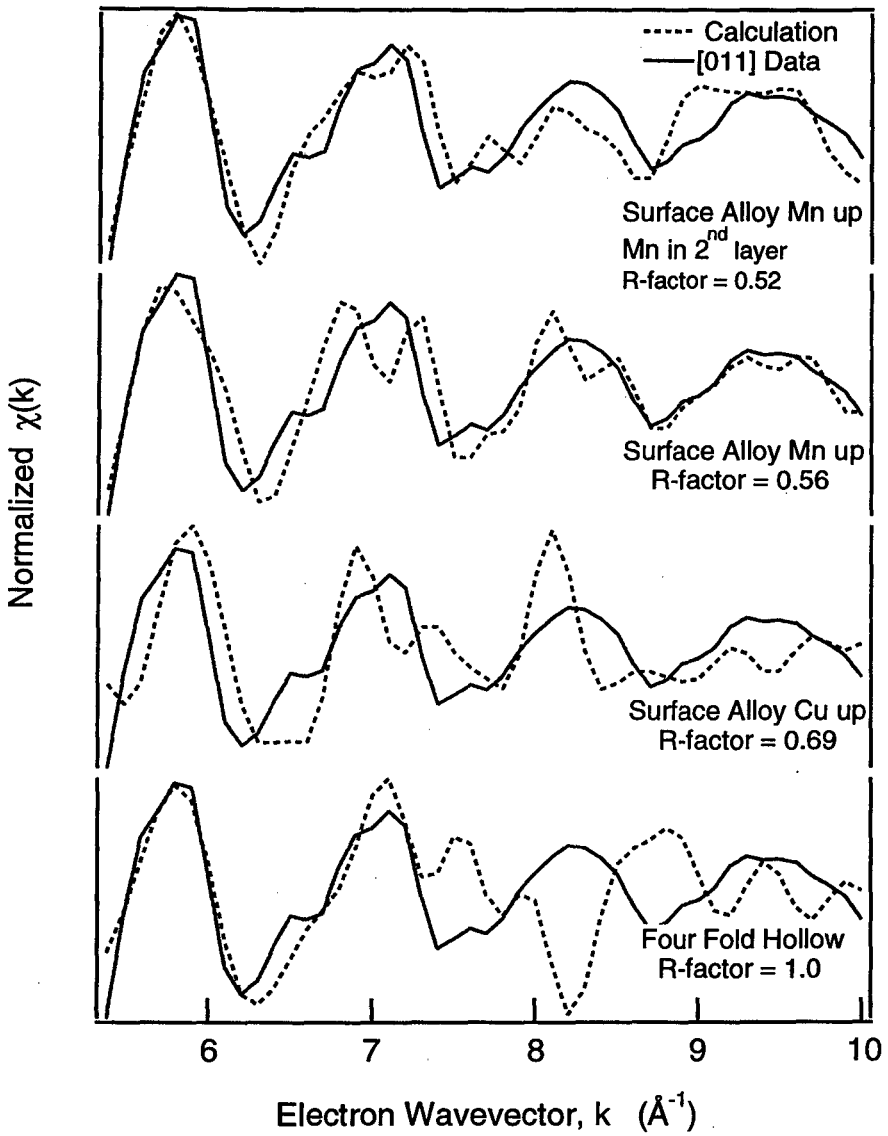

Figure 17. Comparison of the MSSW best fit calculations to the [011] emission data for different adsoption geometries. The surface alloy with the Mn up out of the surface Cu plane and subsurface Mn is the best fit with an R-factor equal = 0.42

greater than that of clean metals such as Ni[28]. Also, the holographic data clearly shows that there is some Mn in the second layer, and though we may overestimate the Mn concentration with the model described above, any reasonable fitting model must include a Mn emitter in the second layer. Lastly the Mn 3p lineshape data also suggests the presence of a significant amount of second-layer Mn.

From the best-fit parameters the corrugation of the surface-alloy layer is 0.30 ± 0.04 Å with the Mn atoms above the surface plane of Cu atoms. The spacing between the surface Cu and the second-layer Cu is 1.85 ± 0.04 Å, equal to the bulk value of 1.81 Å within the error bars of the measurment. The corrugation of the

Table II. Best fit parameters and the associated R-factors for several surface structures. The best fit is for the structure with some Mn in the second layer and the Mn 'up' above the copper in the surface layer.

Adsorption Site	Surface Corrugation (Å)	2nd Layer Corrugation (Å)	Cu1-Cu2 (Å)	Cu2-Cu3 (Å)	R-factor
Surface Alloy Mn up with 2nd Layer Mn	0.30 ± 0.03	0.06 ± 0.04	1.78 ± 0.03	1.86 ± 0.04	0.42
Surface Alloy Mn up	0.49	--	1.65	1.87	0.56
Four-fold Hollow	0.51	--	1.83	1.79	1.04
Surface Alloy Cu up	0.57	--	2.05	1.91	0.69

The Bulk Cu interlayer spacing is 1.81 Å

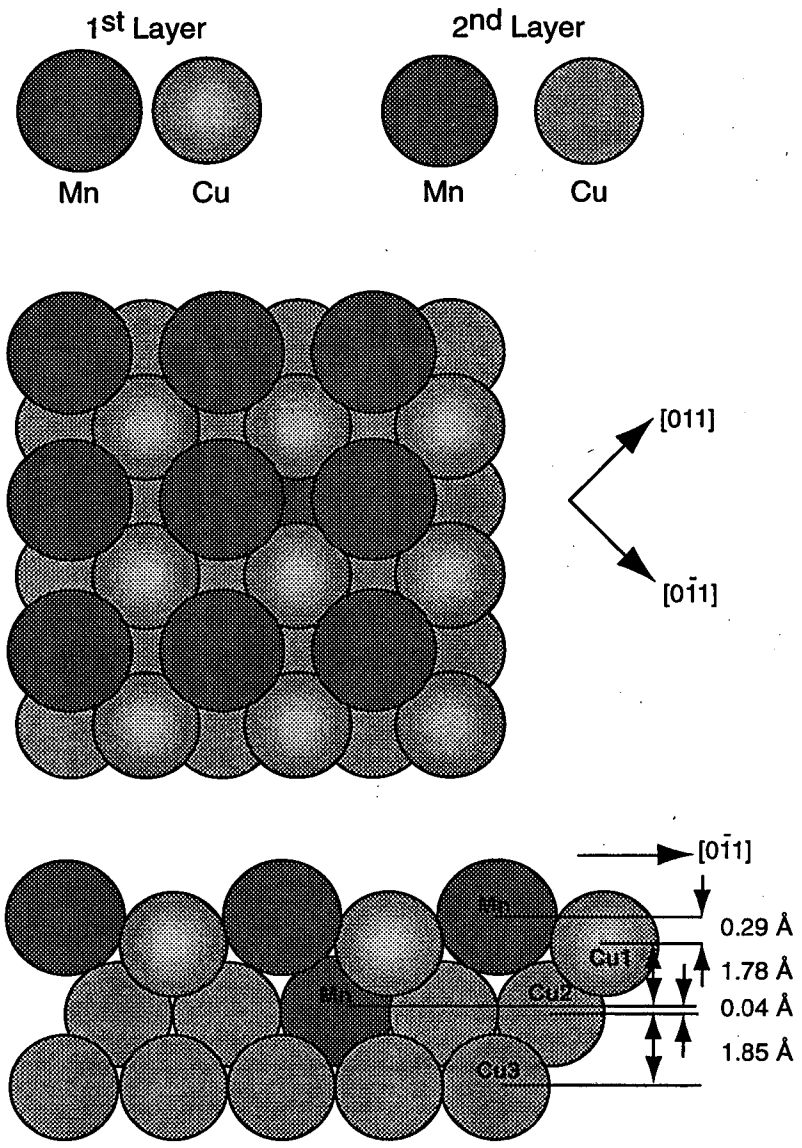

Figure 18. Atomic model of the c(2x2) Mn/Cu(001) structure determined by the present ARPEFS study.

second layer is quite small 0.04 ± 0.04 Å again with the Mn above the plane of the Cu. This corrugation value is close to what is predicted by Ref. 10 for a paramagnetic-Mn atom in bulk Cu, and what would be expected by a comparison of the hard-sphere radii[10]. The spacing between the second- and third-layer Cu atoms is 1.84 ± 0.05 Å. The best-fit value for the inner potential is 8.13 V. The atomic structure of the c(2x2) Mn/Cu(001) surface is shown in Fig. 18.

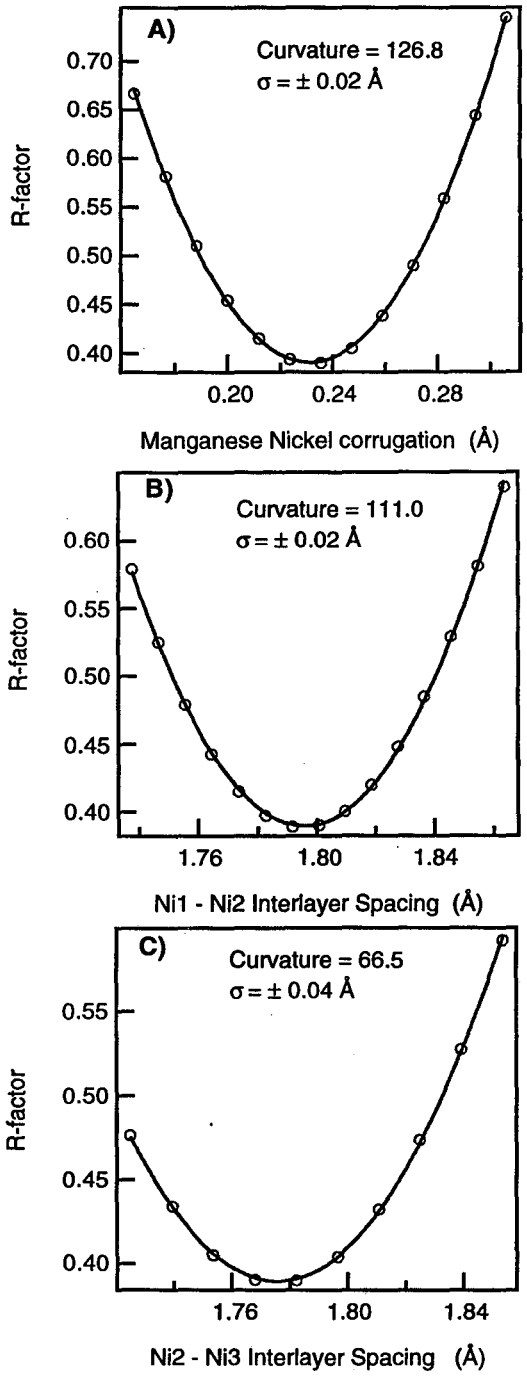

Figure 19. R-factor *vs.* the interlayer spacing (open circles) and a parabolic fit (solid line) A) Mn-Ni B) Ni1-Ni2 C) Ni2-Ni3.

The error bars reported for the fit parameters are one standard deviation. We estimate the statistical uncertainty of each structural parameter from the curvature of the R-factor *versus* parameter value plot. Huang first described this method of assigning error bars in ARPEFS studies[16]. Figs. 19 and 20 show plots of the R-factor *versus* each of the fitting parameters along with the associated standard deviations.

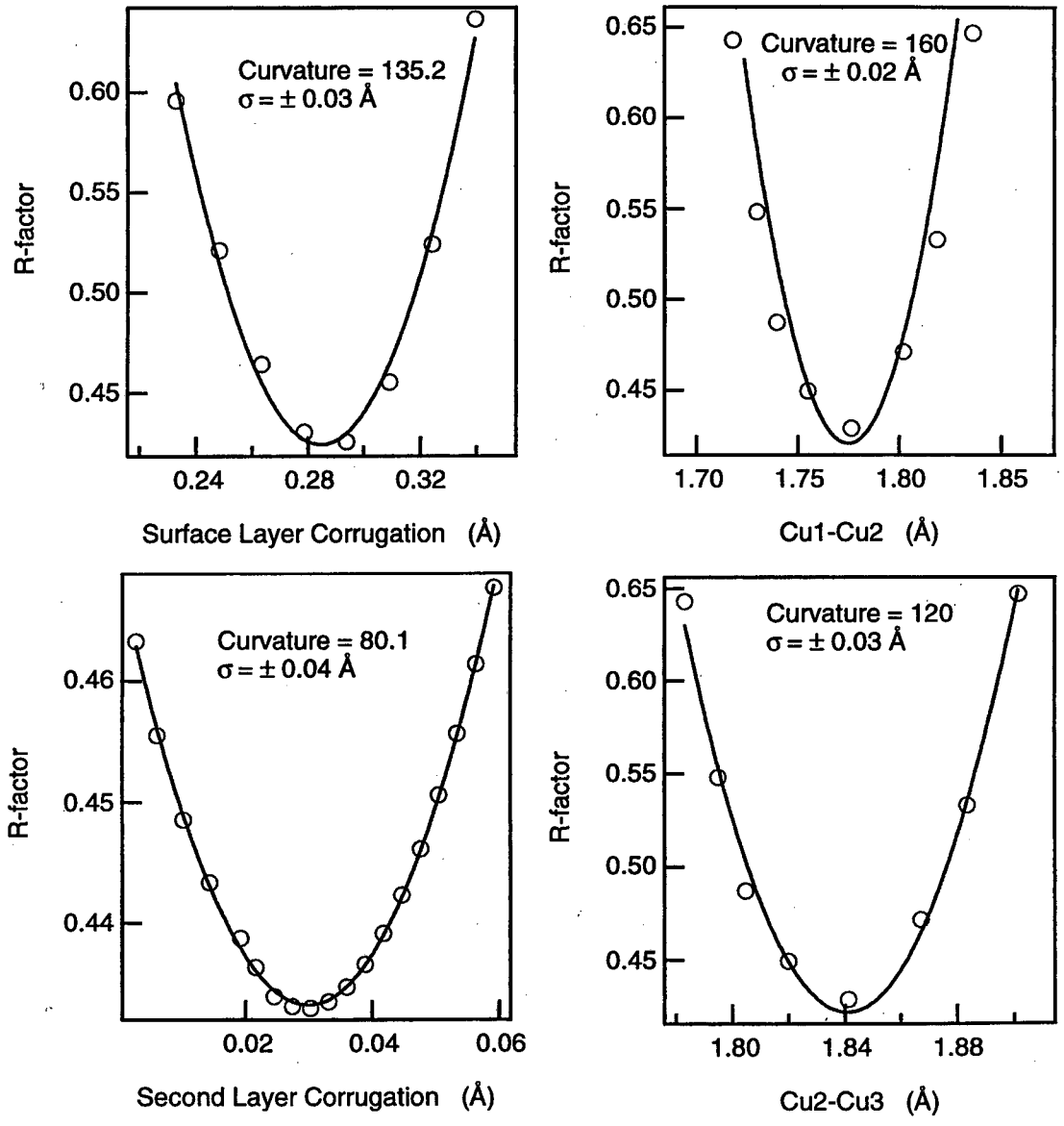

Figure 20. R-factor*vs.* the interlayer spacing (open circles) and a parabolic fit (solid line) A) Surface Corrugation B) Cu1-Cu2 spacing. C) Second layer Corrugation. D) Cu2-Cu3 spacing.

The best-fit results agree very well with the previous LEED I-V analysis[9]. We find surface corrugations of 0.24 ± 0.02 Å and 0.30 ± 0.04 Å for the Ni and Cu phases respectively. The interlayer spacing between the surface-alloy Ni atoms

and the second-layer Ni atoms is 1.80 ± 0.02 Å and the distance between the second- and third-layer Ni atoms is 1.78 ± 0.04 Å. These values represent respectively a 2% and a 1% expansion from the bulk value, though the spacing between the second- and third-layer Ni is the bulk value within the error bars of our measurement. Other authors report bulk spacing for all layers below the surface-alloy layer[9]. The distance between the surface Cu and second-layer Cu is 1.78 ± 0.05 Å and between the second- and third-layer Cu is 1.84 ± 0.05 Å. The LEED study reported bulk spacing for the Cu case which agrees with our analysis within our error bars. Lastly we find the corrugation of the second layer is 0.04 ± 0.04 Å with the Mn above the Cu layer. The previous LEED study did not consider such a model in their analysis, but this value agrees well with the calculated value of a paramagnetic-Mn atom sandwiched by Cu atoms[10].

The expansion of the first-layer Ni in the c(2x2) Mn/Ni(001) alloy may be significant because it concerns the degree of interaction between the Mn 3d orbitals and the Ni sp band. The total-energy calculations showed that the large surface-Mn corrugation is driven by a ferromagnetic state where the Mn has reduced coordination and very little d-cohesion. In this ferromagnetic state with a magnetic moment of 3.75 μ_B there are nearly as many Mn d-bonding states occupied as Mn d-anti-bonding states occupied. In another weakly bound adsorbate system c(2x2)N_2/Ni(001) the physisorbed nitrogen causes no change in the bulk spacing of the substrate nickel crystal[29]. However for the case of c(2x2)S/Ni(001) where one would expect the sulfur to interact quite strongly with the substrate-nickel metal, the interlayer spacing between the first- and second-Ni layers is 1.86 Å, a 6% expansion from the bulk[15, 30]. It seems that the c(2x2)Mn/Ni(100) is in between these two examples, closer to the very weakly bound physisorbed N_2 case.

However, we must also consider the possible formation of bulk layers of MnNi alloy as the driving force for the top-layer expansion. Wuttig *et al.*, found that multiple monolayers of Mn deposited on Ni(100) at temperatures above 450 K lead to the formation of several layers of the MnNi alloy[11]. The LEED I-V analysis of this multiple-layer alloy structure found the lattice constant to be 1.86 Å, in excellent agreement with the value for bulk MnNi of 1.87Å. The 4% expansion of the first layer Ni metal could be explained by the beginning of bulk-alloy formation. However, the holographic data clearly show that there is no subsurface Mn and hence no bulk alloy.

Now we wish to address the weakness of the oscillations in the raw ARPEFS data. A comparison of the theoretical intensity and the experimental intensity for the c(2x2) Mn/Ni(001) $\chi(k)$ curve is shown in Fig. 21. Many researchers have reported surface-Debye temperatures to be as small as one-half the bulk value of the clean metal[31]. In many previous ARPEFS studies this group found surface-Debye temperatures between 50% and 90% of the bulk value accurately describe the experimental data. The calculation shown in Fig. 21 uses the best-fit parameters and a surface-Debye temperature of 375 K, 90% of the bulk Mn value of 410 K. The 45°

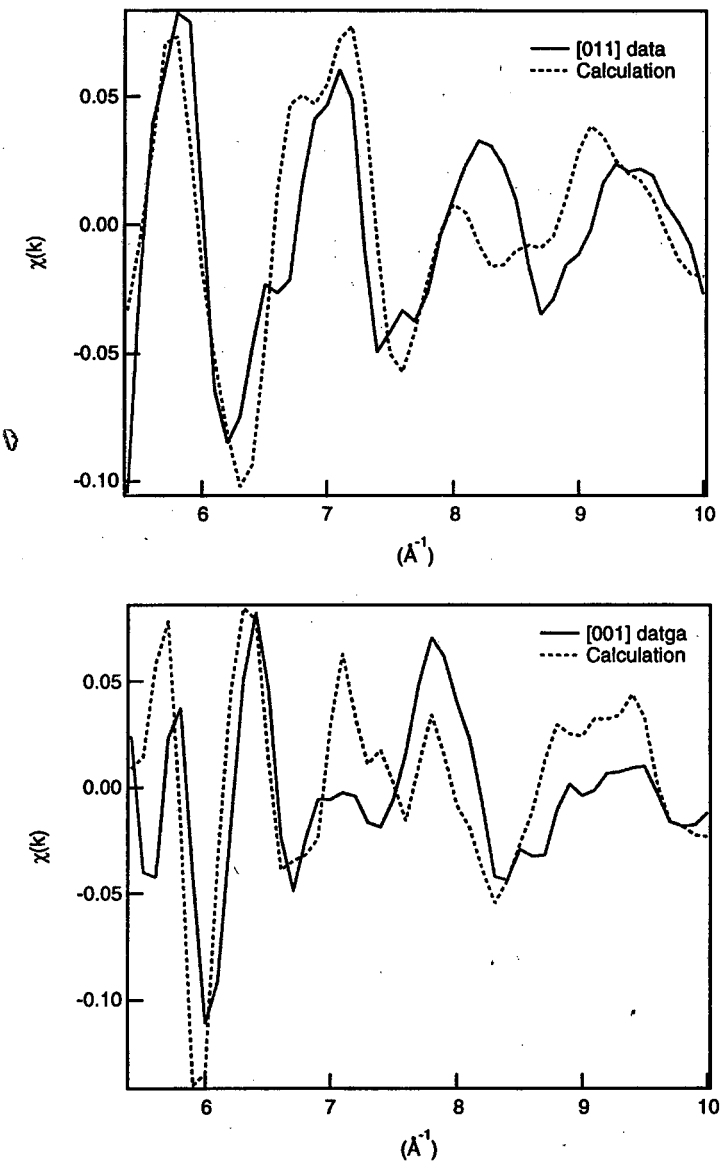

Figure 21. Experimental and calculated c(k) curves for a surface Debye temperature of 375 K, 90% of the bulk Mn value. Top panel 45° emission. Bottom panel normal emission.

data agrees very well with the calculation. For the normal-emission curve the agreement is obviously poorer. However, the agreement is only poor for a small k-range. The missing peak intensity around k equal to six could be due to improper normalization, which considering the the overall weakness of the oscillations seems unfortunate but not unexpected. The important message is that it is the period not the intensity of the oscillations that most reflects the structural parameters determined by ARPEFS.

The relatively weak oscillations in the c(2x2) Mn/Cu(001) data are due to the damping of the signal by the substrate Cu vibrations. The bulk-Debye temperature

for Cu is 343 K, and one can expect the surface-Debye temperature to be well below room temperature. The disorder induced by the thermal vibrations of the substrate can severely reduce the size of the ARPEFS oscillations as shown by Wang *et al.*[18]. This experiment would benefit greatly by cooling the sample.

The growth mechanism for the c(2x2)Mn/Ni(001) appears to be quite different from that for the c(2x2) Mn/Cu(001) and other surface alloys[9, 11, 32, 33]. The fact that we must anneal the one-monolayer or two-monolayer sample before the appearance of the sharp c(2x2) LEED pattern is quite different from the other systems and for the behavior of Mn on Ni(001) reported by other authors. However, with the

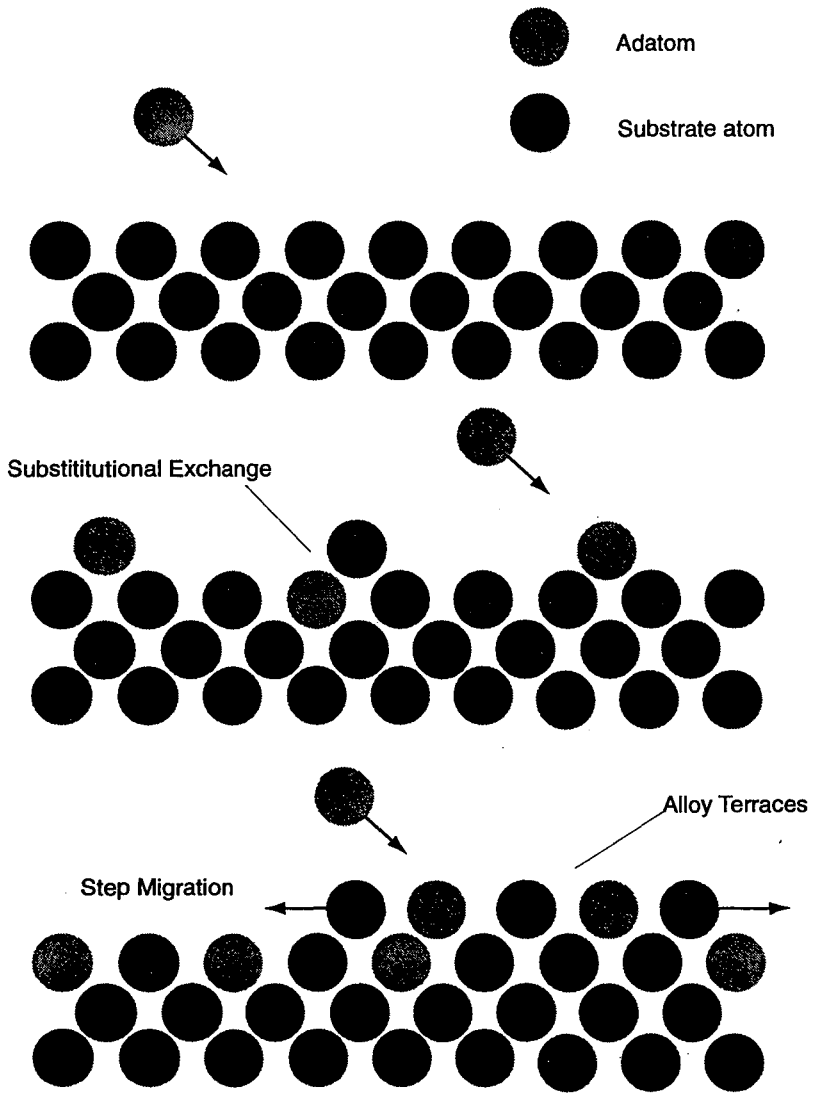

Figure 22. Surface alloy formation mechanism proposed by Chambliss and Chiang for the growth of Au on Cu(100)[34]. An incoming adatom displaces a surface substrate atom. Subsequent adatoms can either displace additional surface substrate atoms or form alloy terraces with the displace substrate atoms. This mechanism leads to adatoms below the surface alloy layer.

transition temperature for surface-alloy growth near room temperature, 275 K, differences in crystal cleanliness or terrace size could affect the kinetics enough to push the transition temperature to 350 K as we found. Of more interest is the lack of subsurface Mn. Chambliss and Chiang proposed a growth mechanism whereby the incoming-adsorbate atom replaces a surface atom; subsequent adatoms can either replace other surface atoms or form a second surface-alloy layer with the displaced substrate atoms[34]. It is easy to see how this mechanism would lead to subsurface-adsorbate atoms, and indeed Naumovic *et al.* reported seeing adsorbate atoms in the second- and third-substrate layers with high-energy-photoelectron holography for c(2x2) Au/Cu(001)[33]. For Au/Cu(001) and Mn/Cu(001) the surface free energies are more favorable for such a mechanism than for the Mn/Ni(100) case. Table III lists the surface free energies for several metals[31, 35]. The large difference between the surface free energies more strongly favors the Mn wetting the surface Ni than the surface Cu and prevents the Mn from diffusing into the bulk.

Table III. Surface free energies of some metals of interest

Material	γ (J/cm^2)
Au	1.41
Cu	1.67
Mn	1.54
Ni	2.38

Other studies of Mn on Ni(001) reported that evaporating multiple monolayers of Mn onto Ni(100) at 450 K lead to the formation of several layers of bulk MnNi alloy[11]. Considering the surface free energies, the photoemission data of the sample preparation, and the holographic information we feel that we can comment on the mechanism for this bulk-alloy formation. We found that to create the c(2x2) Mn/Ni(100) surface alloy we had to anneal the sample with one ML or even two ML of Mn evaporated onto the Ni substrate. After annealing,the concentration of Mn drops by half (Fig. 2). However, after annealing, as we have shown with the holographic data, there is no subsurface Mn. Where does the extra Mn go? It seems unreasonable to believe that it could diffuse through the bulk and out of the photoemission-information depth so rapidly, especiallly considering the surface free energies. We feel that it must be evaporating off the surface. Secondly the growth of bulk-MnNi alloy must be driven by the migration of Ni from the bulk to the surface layers and not by the diffusion of the Mn into the bulk.

Conclusion

We have examined the two Mn surface alloys, c(2x2) Mn/Ni(001) and c(2x2) Mn/Cu(001) with ARPEFS and high-energy-photoelectron holography. In agreement with previous LEED studies we find that the top layers are highly corrugated suface alloys with the Mn above the substrate-surface plane. The corrugation of the surface-alloy layer is 0.24 $\pm$ 0.02 Å and 0.30 $\pm$ 0.04 Å for the Ni and Cu surfaces respectively. The spacing between the surface Ni and the second-layer Ni is 1.80 $\pm$ 0.02 Å. This value is a 4% expansion from the bulk value of 1.76 Å. The spacing between the second- and third-layer Ni atoms is 1.78 $\pm$ 0.04 Å, a 2% expansion from the bulk. The holography data clearly shows that the alloy interface is very abrupt with very little Mn leaking into the bulk Ni. We believe that this information may be applied to the growth of multiple layers of MnNi alloy, and that this alloy formation is determined by the migration of Ni to the surface.

In contrast, the c(2x2) Mn/Cu(001) system has significant amount of Mn replacing Cu atoms in the second layer. This subsurface Mn is evident in the holograms as forward focusing peaks and in the Mn 3p photoemission data as a very broad peak when compared with the Mn 3p peak from the Ni sample. The Cu sample's broad Mn 3p peak may be due to two, chemically different Mn sites. We suggest that the surface Mn which is ferromagnetic, and that the Mn in the bulk is paramagnetic. The corrugation of the surface-alloy layer, was confirmed by using the polar-angle position of the forward-focusing peaks in experimental hologram. The distance between the surface Cu and the second-layer Cu is 1.78 $\pm$ 0.04 Å and between the second- and third-layer Cu atoms the distance is 1.84 $\pm$ 0.04 Å. Both of these value are equal to the bulk value of 1.81 Å within the experimental error. The corrugation of the second layer is 0.07 $\pm$ 0.04 Å again with the Mn above the Cu layer.

References

[1] P. Beccat, J. C. Bertolini, Y.Gauthier, J. Massardier, and R. Ruiz, Journal of Catalysis **126**, 451-456 (1990).

[2] D. S. Wang, R. Wu, and A. J. Freeman, Journal of Applied Physics **73** (1993).

[3] W. L. O'Brien and B. P. Tonner, Physical Review B. **49**, 15370-15373 (1994).

[4] J. G. Gay and R. Richter, Physical Review Letters **56**, 2729 (1986).

[5] P. Eckerlin and H. Kandler, , edited by K. H. Hellwege and L. Bornstein (Springer-Verlag, New York, 1971), Vol. 6.

[6] T. Flores, M.Hansen, and M. Wuttig, Surface Science **279**, 251-264 (1992).

[7] W. L. O'Brien, J. Zhang, and B. P. Tonner, Journal of Physics, Condensed Matter **5**, L515-L520 (1993).

[8] W. L. O'Brien, Journal of Applied Physics **76**, 6484-6470 (1994).

[9] M. Wuttig, C. C. Knight, T. Flores, and Y. Gauthier, Surface Science **292**, 189-195 (1993).

[10] M. Wuttig, Y. Gautier, and S. Blugel, Physical Review Letters **70**, 3619- 3622 (1993).

[11] M. Wuttig, T. Flores, and C. C. Knight, Physical Review B **48**, 12082-12092 (1993).

[12] M. Wuttig, S. Junghans, T. Flores, and S. Blugel, Physical Review B **53**, 7551-7554 (1996).

[13] H. P. Noh, T. Hashizume, D. Jeon, Y. Kuk, H. W. Pickering, and T. Sakurai, Physical Review B **50**, 2735 (1994).

[14] J. J. Barton, C. C. Bahr, Z. Hussain, S. W. Robey, J. G. Tobin, L. E. Klebanoff, and D. A. Shirley, Phys. Rev. Lett. **51**, 272-275 (1983).

[15] J. J. Barton, C. C. Bahr, S. W. Robey, Z. Hussain, E. Umbach, and D. A. Shirley, Phys. Rev. B **34**, 3807-3819 (1986).

[16] Z. Huang, Ph.D. Thesis, (University of California, Berkeley, 1992).

[17] L. J. Terminnello, X. S. Zhang, S. Kin, A. E. S. v. Wittenau, K. T. Leung, and D. A. Shirley, Physical Review B **38**, 3879-91 (1988).

[18] L.-Q. Wang, A. E. Schach von Wittenau, Z. G. Ji, L. S. Wang, and D. A.

[19] L.-Q. Wang, Z. Hussain, Z. Q. Huang, A. E. Schach von Wittenau, and D. A. Shirley, Physical Review B (Condensed Matter) **44**, 13711-19 (1991).

[20] X. S. Zhang, L. J. Terminello, A. E. S. v. Wittenau, S. Kim, Z. Q. Huang, Z. Z. Yang, D. A. Shirley, F. M. Tao, and Y. K. Pan, (Lawrence Berkeley National Laboratory, 1987)

[21] X. S. Zhang, L. J. Terminello, S. Kim, Z. Q. Huang, A. E. S. v. Wittenau, and D. A. Shirley, J. Chem. Phys. **89**, 6538-6546 (1988).

[22] C. S. Fadley, in *Synchrotron Radiation Research : Advances in Surface Science*, edited by R. Z. Bachrach (Plenum, New York, 1990).

[23] J. W.F. Egelhoff, Crit. Rev. Solid State Mater. Sci **16**, 213 (1990).

[24] P. Elmer, (Physical Electronics, Inc., 1993).

[25] V. L. Moruzzi, J. F. Janak, and A. R. Williams, *Calculated Electronic Properties of Metals* (Pergamon Press, Inc., New York, 1978).

[26] Y. F. Chen, W. Wu, and D. A. Shirley, (To be published).

[27] S. Tanuma, C. J. Powell, and D. R. Penn, Surf. Interface Anal. **11**, 577-589 (1988).

[28] J. W. M. Frenken and J. F. v. d. Veen, Physical Review Letters **51**, 1876-1879 (1983).

[29] E. J. Moler, S. A. Kellar, Z.Hussain, W. R. A. Huff, Y.Zheng, E. A. Hudson, Y.Chen, and D. A. Shirley, Submitted to Chemical Phsics Letters (1996).

[30] J. J. Barton, Ph.D. Thesis (The University of California, Berkeley, 1985).

[31] G. A. Somorjai, *Introduction to Surface Chemistry and Catalysis* (Wiley-Interscience, New York, 1994).

[32] T. Flores, M.Hansen, and M.Wuttig, Surface Science **279**, 251-264 (1992).

[33] D. Naumovic, A. Stuck, T. Gerber, J. Osterwalder, and L. Schlapbach, Surface Science **269/270**, 719-723 (1992).

[34] D. D. Chambliss and S.Chiang, Surface Science **264**, L187 (1992).

[35] W. R. Tyson and W. A. Miller, Surface Science **62**, 267 (1977).

What a beautiful world it was once. At least a river of it was. And it was almost mine and my family's and just a few others' who wouldn't steal beer. You could leave beer to cool in the river , and it would be so cold when you got back it wouldn't foam much. It would be a beer made in the next town if the town were ten thousand or over. What a wonderful world it was once when all the beer was not made in Milwaukee, Minneapolis or St. Louis.

Normal Maclean, A River Runs Through it.

CHAPTER 4

THE SURFACE STRUCTURE OF (1x1)O/W(110)x12 DETERMINED BY ANGLE-RESOLVED PHOTOEMISSION EXTENDED FINE STRUCTURE

I. Introduction

Oxygen adsorption on tungsten is one of the earliest and most studied model adsorption systems[1]. Researchers have identified multiple coverage-dependent phases on the W(110) face[2,3]. The three ordered phases are the (2x1) with a coverage of θ= 0.5 monolayer (ML), the (2x2) with θ= 0.75 ML, and the (1x1) with θ= 1.0 ML. The higher coverage phases are considered to be two-dimensional oxides with the oxygen arranged along the close-packed substrate directions. Previous researchers found that annealing these high-coverage phases led to additional superstructures in LEED[2]. These additional LEED spots were interpreted as due to a compressed "misfit" oxygen overlayer[2]. This structure would be extremely difficult to determine with a diffraction technique like Angle-Resolved Photoemission Extended Fine Structure (ARPEFS), because of the number of different scattering geometries. Recently however, using scanning tunneling microscopy (STM), Chiang *et al.* showed that these high-order diffraction spots were instead due to very regularly spaced domain walls[4]. These walls separate domains where the oxygen adsorption site switches from the left side to the right side of the unit cell. This configuration leads to domain walls which alternate between higher oxygen concentration and lower concentration than the rest of the surface. Figure 1 shows an illustration of these domain walls as well as the high-symmetry adsorption sites. The distance between the walls is *ca.* 10 atomic units[4]. Fadley *et al.* labeled this LEED structure [(1x1)O/W(110)]x12[5].

While the STM study showed the origin of these higher-order diffraction spots, no detailed atomic-structural study has been done for this system to date. In the present study we use Angle-Resolved Photoemission Extended Fine Structure

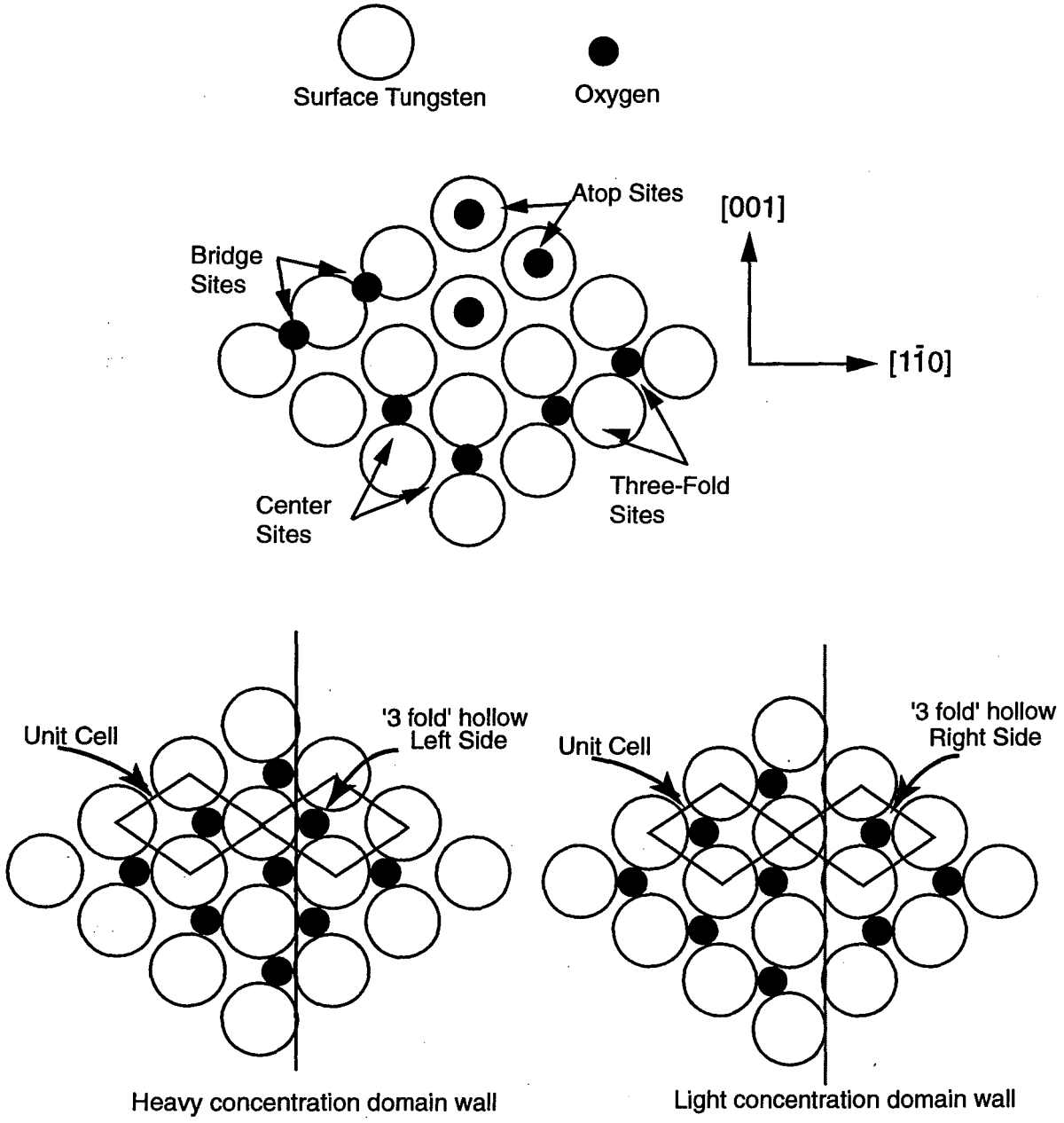

Figure 1. Top panel: Surface structure of the (1x1) O/W(110) showing possible high-symmetry adsorption sites. The bottom panel shows the oxygen atoms adsorbed into the quasi-threefold hollow site. The site exchange domain walls were proposed by Chiang *et al.* to explain the additional LEED superstructure seen when the (1x1)O/W(110) surface is annealed. The adsorption site exchange leads to alternating domain walls with light or heavy oxygen concentration. The LEED pattern for this structure is 12x1

(ARPEFS) to determine the adsorption site and local atomic structure of [(1x1) O/W(110)] x 12. ARPEFS is a well established technique for determining the atomic structure of atomic and molecular adsorbates on metal surfaces[6-12]. The technique's advantages are its elemental selectivity through the binding energies of core level electrons, the large oscillations in intensity, and its inherent accuracy.

II. Experimental

These experiments were performed at the Advanced Light Source (ALS) on beamline 9.3.2, a bend magnet beamline with a spherical grating monochromator (SGM). Three gratings span an energy range from 30 eV to 1200 eV, with a maximum resolving power, $E/\Delta E = 10{,}000$[13]. An optical layout of the important components is shown in Figure 2.

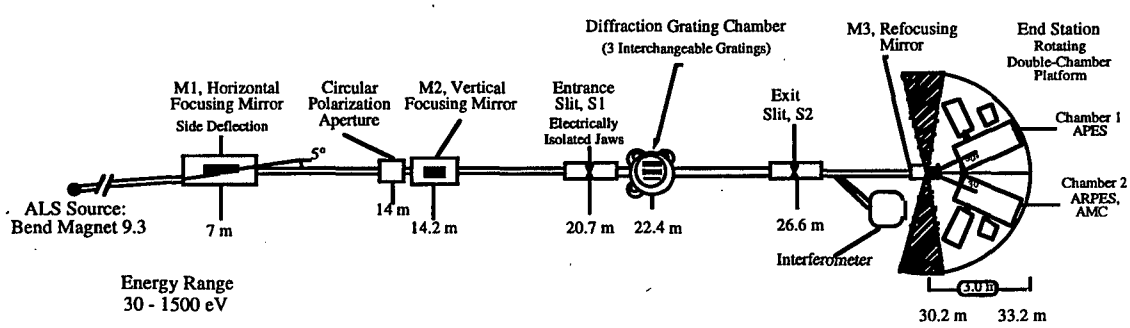

Figure 2. Optical layout of Beamline 9.3.2 at the Advanced Light Source in Berkeley. The important optical elements are labeled. Also shown in the figure is the rotating platform where the experimental chamber shown in Figure 3 is installed.

The analyzer and chamber system for these measurements is unique and deserves some special attention. A more complete description can be found in Reference 14. The system is built around a Scienta ES200 hemispherical, electron-energy analyzer. This analyzer has a 200 mm mean radius and an ultimate resolution of 4 meV at 5 eV pass energy[14]. The energy-selected electrons are collected by a single, multichannel detection system based on a phosphor screen and a CCD (charge coupled device) camera. The CCD camera limits the maximum integrated count rate to 100 kHz. This detector is the limiting factor preventing this system from achieving its full potential at a third generation synchrotron light source such as the ALS (Advance Light Source). The detector has a non-linear response at both

large and small count rates. The nonlinearity is a concern especially for ARPEFS which will be discussed in more detail in this section. This detector is in the process of being upgraded, which will greatly increase the utility of this system. The analyzer is mounted to a chamber which can rotate over 60° in the plane of the electron storage ring. This rotation is accomplished by the use of differentially pumped, rotary seals on the chamber and a large, 12.0 inch diameter, bellows connecting the chamber to the beamline. Figure 3 is a schematic drawing of the experimental chamber.

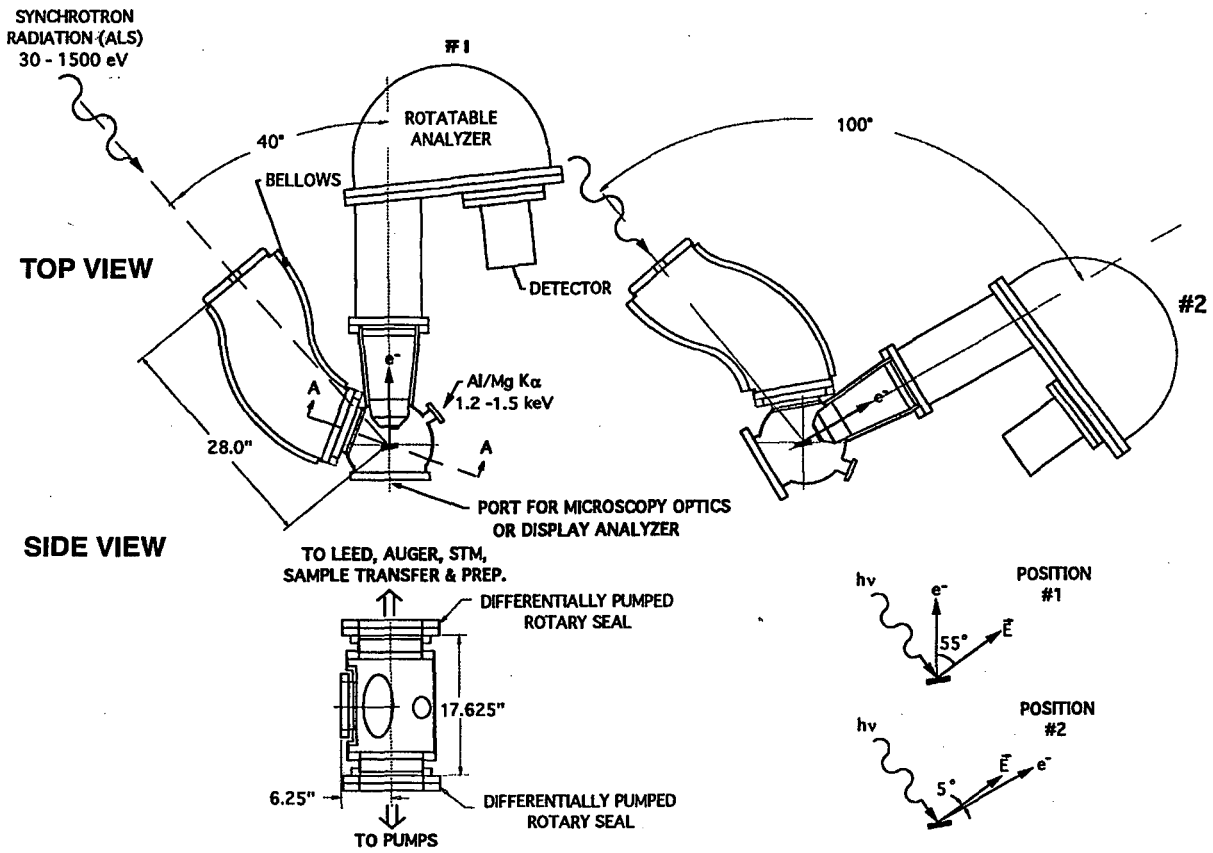

Figure 3. Schematic of the Advanced Photoelectron Spectrometer installed at Beamline 9.3.2 at the ALS. The Figure shows the two extremes of the analyzer rotation. The important components are labeled.

The manipulator for this chamber has three translational degrees of freedom, x, y, and z, as well as high-precision angular rotation about the surface normal, ϕ, and about the vertical axis, θ. The θ and ϕ rotations are computer-controlled, which allows for the efficient collection of angle-scanned diffraction data, photoelectron holograms. The sample can be heated by electron bombardment to 2500 K. The experimental chamber is further equipped with the standard surface-science equipment.

The tungsten crystal was aligned to within ± 0.5° of the (110) direction and polished with one μm and six μm diamond paste to obtain a mirror like finish. We cleaned the tungsten crystal in vacuum with repeated cycles of hot oxidation followed by flash annealing to 2200 K to remove the oxide layer. After this cycling process there was no evidence of carbon, sulfur, or oxygen contamination, as determined by core-level photoemission. The base pressure in the experimental chamber was 7×10^{-11} Torr. We found that to obtain a clean crystal the chamber pressure must not exceed 5×10^{-9} Torr during the flash-heating step. The LEED pattern after the cleaning process is a very sharp (1x1) pattern.

The (1x1)x12 oxide preparation method is from Diamon[15]. After the cleaning process, the crystal is warmed to 1000 K and exposed to 2×10^{-6} Torr of O_2 for 11 minutes 40 seconds. The resulting LEED pattern is 1x1 with extra superstructure diffraction features. These higher-order spots align along the $[1\bar{1}3]$ direction. After the sample preparation, the crystal was still free from carbon or sulfur contamination and will remain so for literally days due to the passivation of the surface by the oxygen. The ARPEFS data were taken on this surface structure at room temperature.

During the data collection the crystal was oriented such that the polarization vector, $\mathcal{E}$, of the synchrotron radiation was along the <001> azimuth. The photoemission spectra were taken at two different angles, normal emission and 45° from normal emission along the <001> azimuth (Figure 4). In the rest of this paper we will describe these directions as normal emission and off-normal emission, respectively.

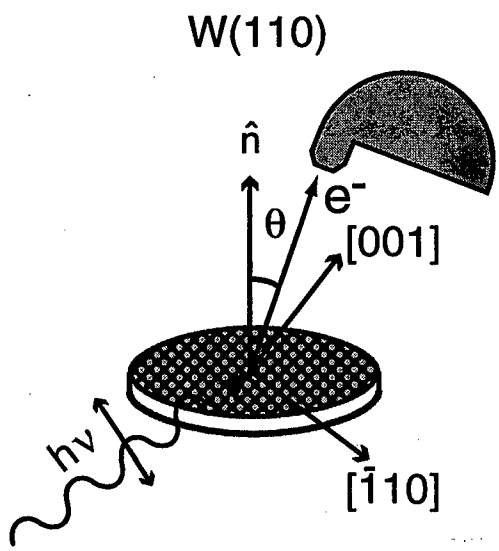

Figure 4. The experimental geometry for the ARPEFS data collection. The radiation polarization vector, $\mathcal{E}$, is aligned along the <001> zone for all data collection. The photoemission spectra were measured at normal emission, $\theta = 0°$, and at 45° off-normal along the <001> azimuth. The [001] direction corresponds to the short axis of the BCC (110) face unit cell. The $[1\bar{1}0]$ direction is along the long axis of the unit cell.

The raw ARPEFS data are two series of O 1s angle-resolved photoemission spectra taken at varying photon energies for the two emission directions described in the paragraph above. For each series, the photon energy is changed so that the kinetic energy of the outgoing photoelectron ranges from 100 eV to 350 eV. This energy range corresponds to a wavevector range from 5 $Å^{-1}$ to 9.5 $Å^{-1}$. The electron wavevector is related to the electron kinetic energy, E_k by the following relation; $k(Å^{-1}) = 0.512\sqrt{E_k(eV)}$. The O 1s data range is truncated from the usual ARPEFS range because the small cross-section and decreased flux at photon energies above 900 eV preclude taking useful spectra with electron kinetic energies greater than 350 eV. The next step in the data reduction was to extract accurate peak areas from each of the spectra in each series. We accomplished this by fitting the O 1s peak with a voigt function, a linear background and a step-function. The voigt function is a convolution between the peak's inherent Lorentzian shape and the instrumental gaussian broadening caused by the monochromator and the electron energy analyzer. The step-like function models the inelastically scatter electrons in the low kinetic energy tail of the spectrum. A sample fit to the O 1s data is shown in Figure 5.

The peak intensity plotted against its position in k-space is denoted as I(k). This function I(k) has two components; a slowly varying, atomic-like portion, $I_0(k)$,

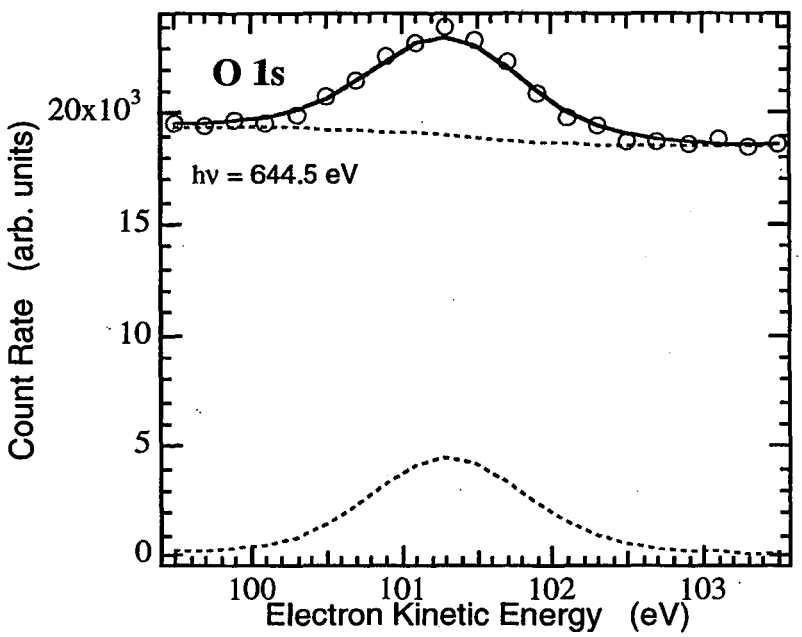

Figure 5. A typical O 1s photoemission spectrum of [O(1x1)/W(110)]x12 for this work. The open circles are the data points, the dashed lines are the deconvolved components of the fit to the data, and the solid line is the total fit.

upon which is superimposed a rapidly oscillating beat pattern that arises from the interference between the primary wave propagating directly to the detector and waves which scatter elastically off nearby atomic potentials before reaching the detector. The experimental and calculated diffraction curves, $\chi(k)$ are obtained by removing the slowly varying $I_0(k)$ portion from I(k).

$$\chi(k) = \frac{I(k) - I_0(k)}{I_0(k)} \tag{1}$$

We construct $I_0(k)$ in two steps. The first step is to create an intermediate $I_0(k)$ consisting of seven points. The first and seventh points are the first and last points of I(k). The five points in between the first and seventh are calculated by dividing I(k) into five sections of equal length in electron wavevector, k. The average value of I(k) in each of these five sections is one of the five points in the intermediate $I_0(k)$. In the second step we set $I_0(k)$ equal to the fit of a cubic spline through the seven points making up the intermediate $I_0(k)$. Additionally, to remove noise from the $\chi(k)$ curves, we Fourier-filtered the experimental the curves removing the high-frequency components. These components are due to noise and to very long path length differences from multiple scattering events. These very long electron paths involve many scattering events and are weak components of the overall $\chi(k)$ curve. Their removal has little effect on the structural information in the $\chi(k)$ curve.

The dynamic range of this experiment, even for the O 1s data, is far too great for the present 100 kHz detector. This limited dynamic range requires that great care to prevent detector saturation during data collection. We checked for saturation affects in the O 1s data by comparing the peak intensity to background intensity for different pass energies at several k-values in the data range. We chose a pass energy where the peak-to-background ratio was constant throughout the ARPEFS data range. This meant that at some photon energies we had to count for several seconds per data point to collect good statistics. The long counting times greatly increase the time required for one data set. The extended data collection time is not a problem for this sample but may be for future systems that are more reactive unless the detector is replaced by one which can handle higher count rates. The O 1s data collection took six to seven hours per emission direction.

III. Fourier Analysis

The auto-regressive linear-prediction based Fourier transform (ARLP-FT) transforms the diffraction data from momentum space to real space[16]. In ARPEFS, the positions of the strong backscattering peaks in ARLP-FT from adsorbate/substrate systems can be accurately predicted using the single-scattering cluster model to-

gether with the concept of strong backscattering from atoms located within a cone centered at 180° from the emission direction. The effective solid angle of this backscattering cone is approximately 30° to 40°, though signals from scattering atoms very close to the source atom may be observable even if the scatters lie outside the nominal backscattering cone.

The ARLP-FT peaks correspond to path-length differences between that component of the wave which propagates directly to the detector and those components which are first elastically scattered by the atomic potentials within this backscattering cone. This scattering takes place within the crystal, which requires that the APREFS data be shifted in energy to account for the effect of the crystal inner potential. In the modeling calculations the inner potential is treated as an adjustable parameter, but for the ARLP-FT analysis we estimate its value as the sum of the work function and the valence band width, which for the present case we take to be 8.0 V. Thus we shifted the ARPEFS data by 8.0 eV to higher kinetic energy before calculating the ARLP-FT.

Analysis of the ARLP-FT provides information about the adsorption site as well as the bonding distance between the oxygen and tungsten atoms. Figure 6 shows the ARLP-FT for each emission direction. The 1x1 LEED structure suggests that O adsorbs to a high-symmetry site on the W(110) surface. Using plane geometry and ignoring phase-shift effects, one can then calculate the path-length differences (PLD) and scattering angles for strong scattering events for each adsorption site geometry. Comparison of the predicted peak positions to the observed peaks in the ARLP-FT usually allows one to determine the adsorption site. In this study we consider the atop, bridge, center and quasi threefold site as possible O adsorption sites. The off-normal ARLP-FT is dominated by one peak at a PLD = 3.5 Å. The strength of this peak immediately suggests a site with very strong backscattering geometry at 45° emission, eliminating the atop site. The normal-emission peaks at 3.1 and 6.7 Å are most consistent with the center or the threefold hollow sites. We cannot distinguish between the center and threefold hollow sites by comparison of the PLD because the scattering geometries are too similar. The Fourier analysis agrees best if the O atom adsorbs in the center or three fold hollow site approximately 1.15 Å above the first-layer tungsten. For this geometry the predicted PLD and the observed ARLP-FT peaks are in good agreement and the relative peak strengths are reasonable for the scattering angles.

IV. Multiple Scattering Calculations

In order to distinguish between the center and threefold sites and to extract more precise structural parameters than determined by the ARLP-FT analysis, we fitted the diffraction data to a full multiple-scattering model. The calculation code for this fitting routine was recently developed by Chen, Wu and Shirley and is based

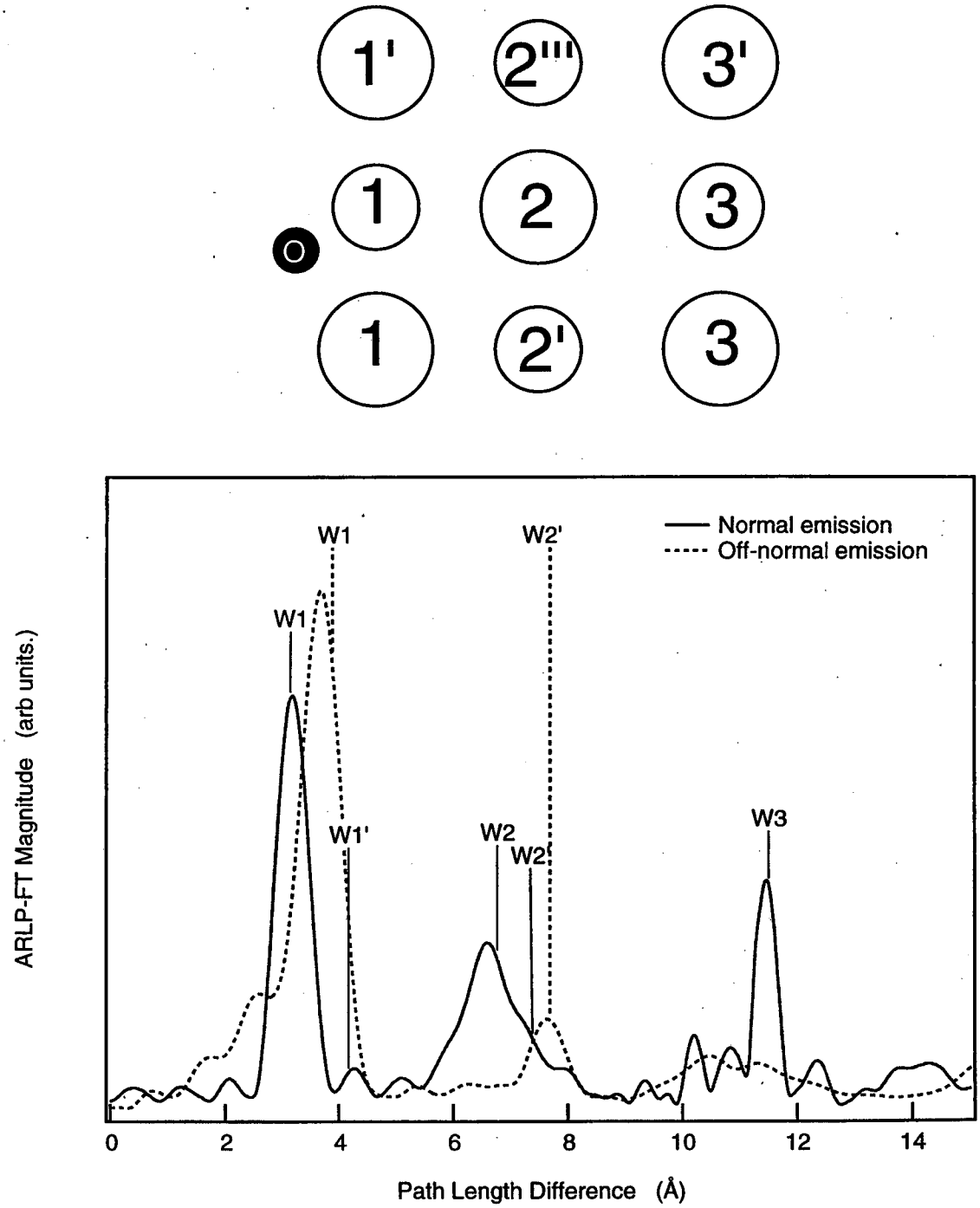

Figure 6. ARLP-FT of the experimental $\chi(k)$ curves for the O 1s normal emission (solid line) and 45° off-normal emission (dashed line). The model indicates the scattering atoms contributing to peaks in the ARLP-FT. In the model the relative size of the W atoms indicates its position relative to the plane of the paper and the O plane. The larger atoms are sticking out of the paper plane and the smaller are into the paper plane.

on the Rehr-Albers formalism[17,18]. This calculation requires both structural and non-structural parameters as input. We used the structural parameters determined by the ARLP-FT analysis as the starting point for the multiple-scattering calculations. The non-structural parameters include the initial-state angular momentum, the atomic scattering phase-shifts, the crystal temperature, the inelastic mean free path, the emission and light-polarization directions, the electron-analyzer acceptance angle, and the crystal's inner potential.

The atomic-scattering phase-shifts were calculated using the atomic potentials tabulated by Moruzzi *et al.*[19]. The emission and polarization directions and the analyzer acceptance angle were set to the experimental values described previously. The inelastic mean free path, λ was included using the exponential damping factor $e^{-\frac{t}{\lambda}}$ where λ was calculated using the formula proposed by Wagner, Davis, and Riggs, $\lambda = kE_k{}^m$[20]. The values for k and m are tabulated from optical data[19-21]. For W we take k = 0.07 and m = 0.716.

We fitted the normal-emission and the off-normal-emission curves simultaneously. We determined the best fit by minimizing the A-factor function defined as

$$A = \frac{\sum(\chi_c - \chi_e)^2}{\frac{1}{2}\sum(\chi_c^2 + \chi_e^2)} \tag{2}$$

The A-factor, more than the conventional R-factor, emphasizes the importance of the structurally sensitive $\chi(k)$ curve periodicity, over the absolute peak intensity. Near the best-fit minimum the A-factor and R-factor analyses are functionally equivalent. However, to be consistent with results reported by other researchers we will report the R-factor as defined by

$$R = \frac{\sum(\chi_c - \chi_e)^2}{\sum\chi_e{}^2} \tag{3}$$

throughout this paper.

We show in Figures 6 and 7 the experimental $\chi(k)$ curves and the best-fits from the MSSW scattering calculation for both emission directions for the threefold and the center sites. For these fits we used a 135-atom cluster and a pathcut of 0.1%. The pathcut is defined as a percentage of the most intense scattering event in the calculation. Scattering events with intensities less than the pathcut value are excluded from the calculation, saving considerable memory and calculation time. Obviously the calculation is more accurate if one includes all scattering events, but we have found that a pathcut of about 0.2% is sufficient for this scattering system. The scat-

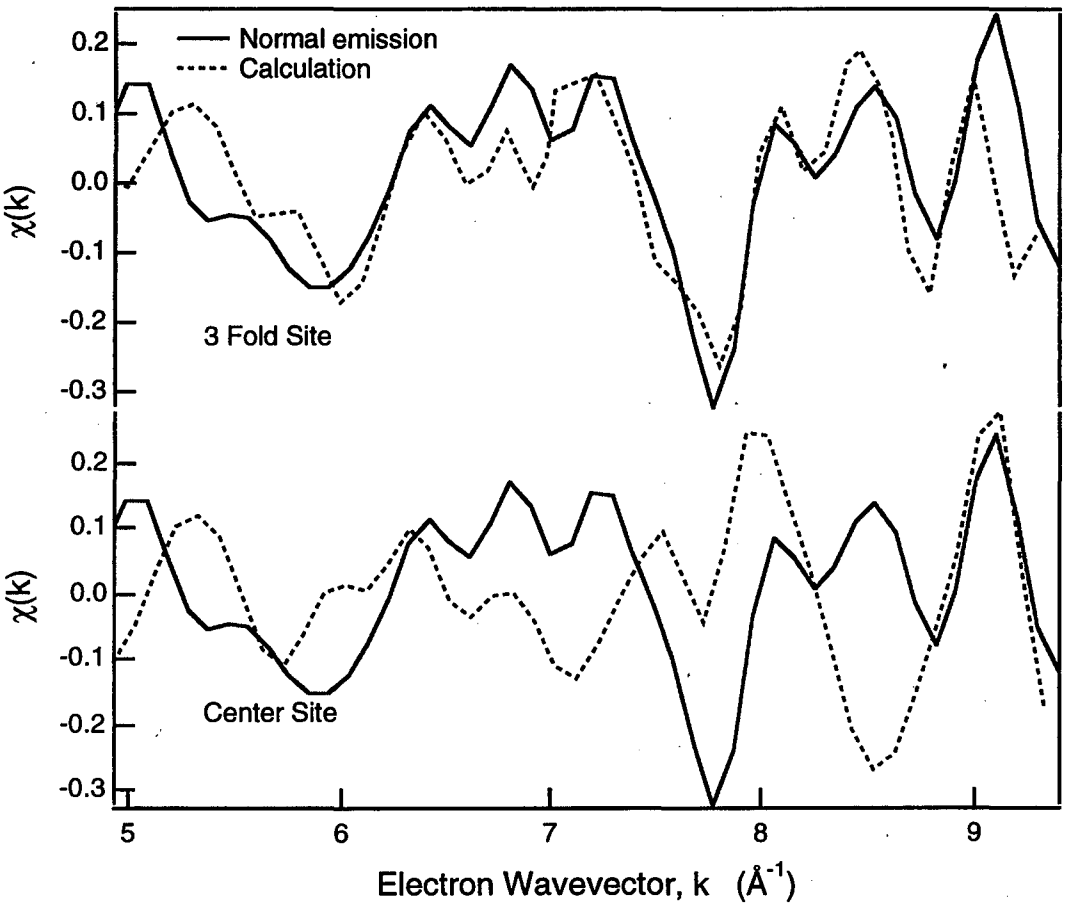

Figure 7. Best-fit calculations to the normal emission O 1s $\chi(k)$ to the threefold hollow and center sites. The normal and off-normal curves were fitted simultaneously. The threefold hollow is the best fit with an R-factor equal to 0.43. The best-fit parameters are O-W1 = 1.21 Å; W1-W2 = 2.19 Å; adsorption site 0.48 Å from center position along $[1\bar{1}0]$.

tering strength of tungsten required the use of such a large cluster and small pathcut. During the fitting routine we allowed the O-W1, the W1-W2, and the O adsorption position along the $[1\bar{1}0]$ direction (the long axis of the unit cell) to float, as well as the inner potential. In a strongly scattering material like W, it is very important to know the emission direction, as accurately as possible. To this end, we used the forward-scattering peaks in the photoelectron hologram to orient crystal surface normal to be parallel with the axis of the analyzer's electron lens.

The threefold hollow site is obviously the best fit to the experimental data with an R-factor equal to 0.43. The best fits determine the O-W1 interlayer spacing to be 1.21 Å, and the W1-W2 spacing to be 2.19 Å. The O-adsorption site is very close to the ideal threefold site, located 0.46 Å from the center of the long axis, along $[1\bar{1}0]$. The true threefold site, equally distant from each of the three W atoms, is 0.56 Å

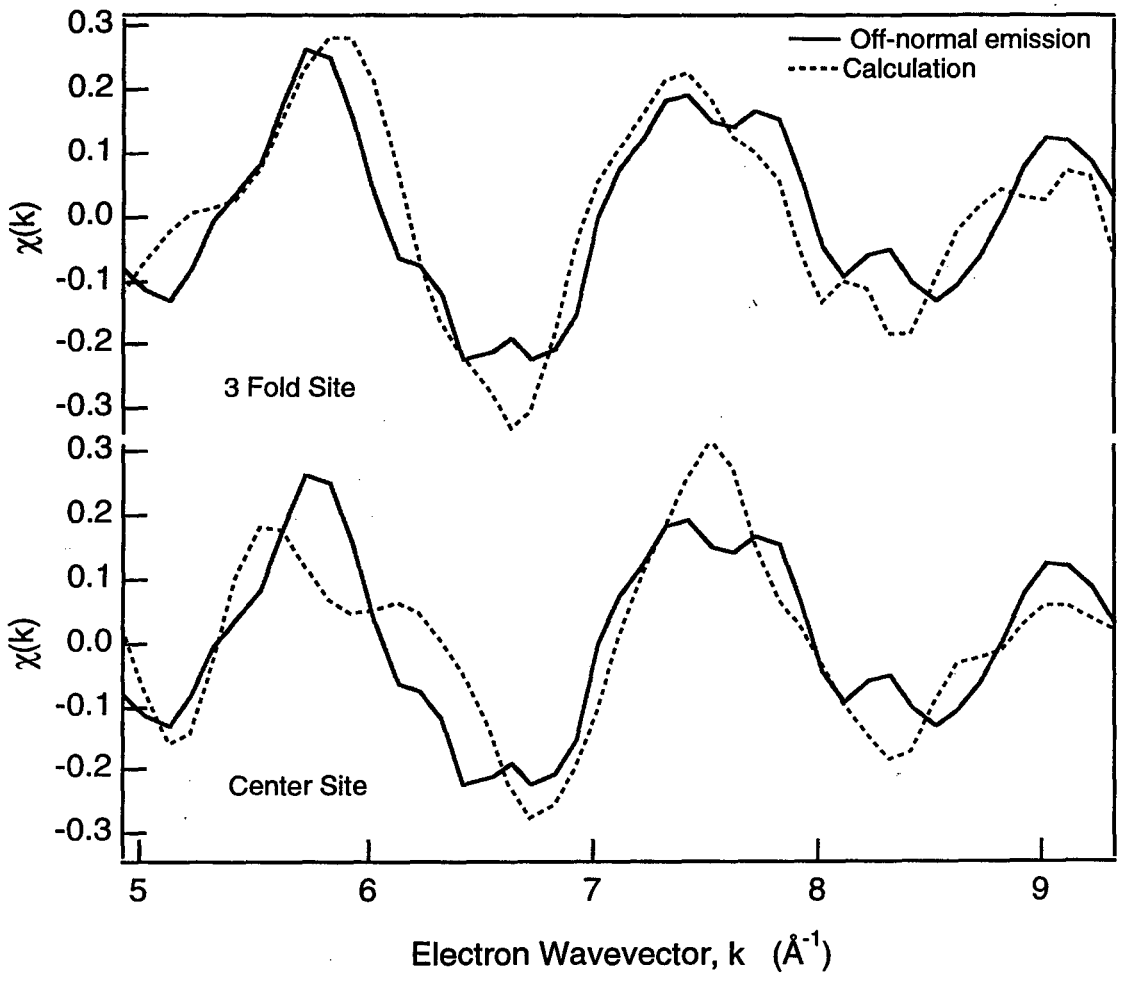

Figure 8. Best-fit calculations to the off-normal emission O 1s $\chi(k)$ to the threefold hollow and center sites. The normal and off-normal curves were fitted simultaneously. The threefold hollow is the best fit with an R-factor equal to 0.43. The best-fit parameters are O-W1 = 1.21 Å; W1-W2 = 2.19 Å; adsorption site 0.48 Å from center position along $[1\bar{1}0]$.

from the center site along the $[1\bar{1}0]$. A surface Debye temperature of 400 K and an inner potential of 8.01 V were found to give the best fit.

To measure the sensitivity of the fitting procedure to the layer spacings and establish error bars we calculated the R-factor for various interlayer spacings. With the inner potential held fixed at the best-fit value of 8.01 eV, the R-factor analyses for the spacing between the oxygen and the first-layer tungsten, the distance between the first- and second-layer tungsten, and the adsorption position along the long axis are shown in Figure 9. Huang discussed the determination of error bars in ARPEFS from the R-factor analysis[22]. Following his treatment we quote error bars of plus or minus one standard deviation. We conclude from the MSSW calculation and the R-factor analysis that the O-W1 spacing is 1.21 ± 0.04 Å, the W1-W2

spacing to be 2.19 ± 0.06 Å, and the position of the oxygen adsorption is 0.46 ± 0.02 from the center site along the $[1\bar{1}0]$ direction.

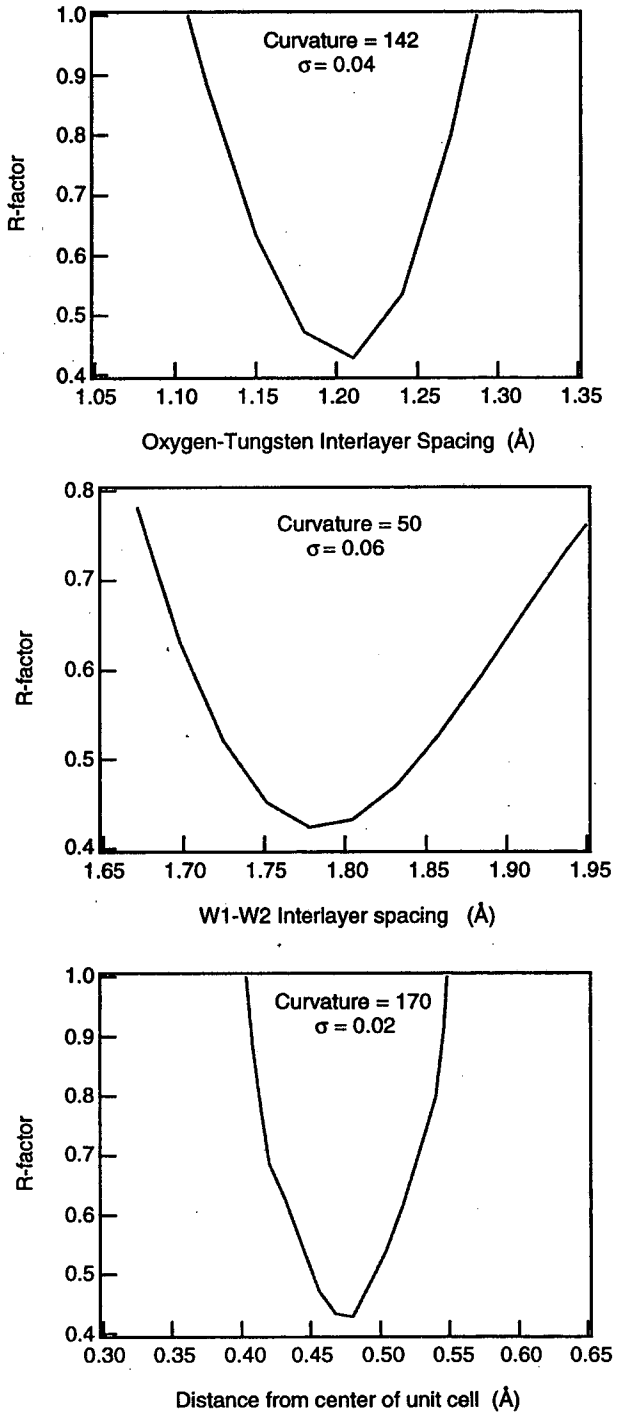

Figure 9. R-factor *vs.* fitted parameter for the O-W1 and W1-W2 interlayer spacing and for the oxygen position from the center position along the $[1\bar{1}0]$ azimuth

V. Discussion

The results of the MSSW calculations are very similar to those found by a previous LEED study on a different O/W(110) phase. These researchers found for the (2x1)O/W(110) phase that the oxygen adsorbs near the threefold site. They reported the distance of the O atoms above the surface to be 1.25 Å. This previous study did not report a value for the distance between the first and second layer tungsten. We find that the local geometry is the same for [(1x1)O/W(110)]x12 phase as for the (2x1)O/W(110) phase independent of the long range order of the oxide layer. We report the oxygen adsorption site to be near the threefold hollow, 1.21 ± 0.04 Å above the surface-tungsten plane.

In order to relate the structure to the bonding involved in the oxide we follow the discussion of Mitchell in analyzing the best-fit bond lengths in terms of the Pauling expression[23, 24]:

$$D(n) = D(1) - 0.6 \log n \tag{4}$$

This expression relates the length of an nth order bond to the single bond length, D(1). Pauling has tabulated values for single-bond radii[23]. For tungsten the single bond length is 1.96 Å. Figure 10 shows the hybrid orbitals for a body centered cubic (BCC) (110) face according to the model of Altmann, Coulson, and Hume-Rothery[25]. The orbitals directed out of the surface at an angle of 54° 44' are the nearest neighbor orbitals whereas those at 45° to the surface are the next-nearest neighbor orbitals. The center site would be the most favored for divalent oxygen if there is complete charge localization at this surface, but that is not possible for hybrids formed entirely from gerade atomic orbitals as discussed by Mitchel and Altmann, Coulson, and Hume-Rothery[24, 25]. A simple average of the resonance structures shown below

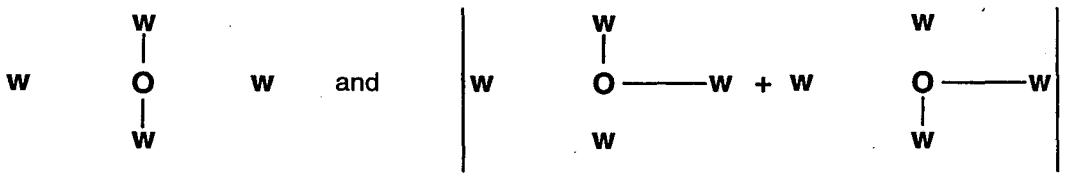

gives two W-O bonds of order 3/4 and length 2.04 Å, and one W-O bond or order 1/2 and length 2.14 Å. The overall average W-O distance is 2.07 Å. This structure requires O to be 1.20 Å above the tungsten surface and displaced 0.47 Å from the center site along the $[1\bar{1}0]$ direction. Note that this is very good agreement with our

results. It is also interesting to note that independent of coverage, the adsorption geometry for oxygen on W(110) is the same.

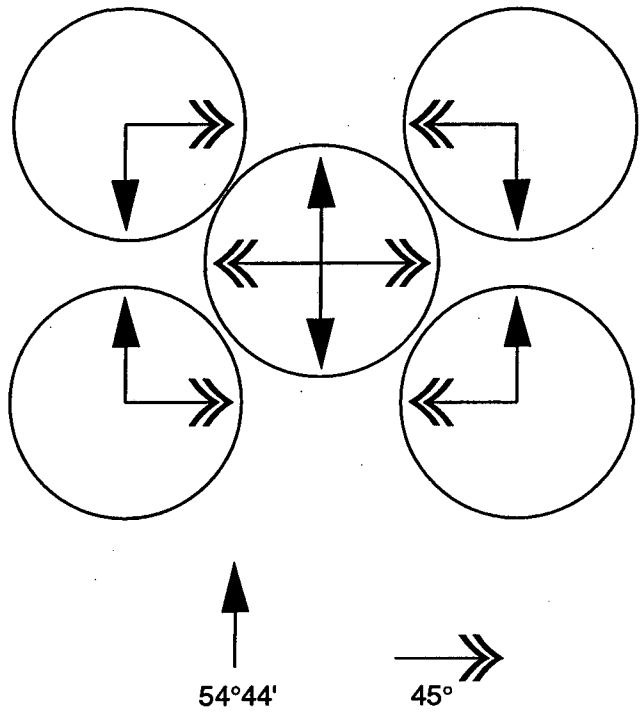

Figure 10. Directions of the hybrid orbitals directed out of the BCC (110) surface according to the model of Altmann, Coulson, and Hume-Rothery.

VI. Conclusion

We have measured the ARPEFS oscillations of the O 1s core-level photoemission peak for the [(1x1)O/W(110)]x12 surface structure and performed multiple-scattering calculations to simulate the ARPEFS. The calculations indicate that the oxygen adsorbs to the quasi-threefold-hollow site on the (110) surface, 1.21 ± 0.04 Å above the tungsten-surface plane. The oxygen adsorbs 0.46 ± 0.02 Å from the center site along the [1$\bar{1}$0] azimuth. The near-surface tungsten layers appear to be unaffected by the surface oxygen as the layer spacing is that of the clean bulk metal. Most interesting, is that the local atomic geometry, as determined by ARPEFS, is independent of the surface-oxygen coverage and long-range surface order.

References:

[1] I. Langmuir, Journal of the American Chemical Society **35**, 105 (1913).

[2] E. Bauer and T. Engel, Surface Science **71**, 695-718 (1978).

[3] T. Engle, H. Niehus, and E. Bauer, Surface Science **52**, 237 (1975).

[4] K. E. Johnson, R. J. Wilson, and S. Chiang, Physical Review Letters **71**, 1055-1058 (1993).

[5] C. S. Fadley, M. A. V. Hove, Z. Hussain, *et al.*, Journal of Electron Sprctroscopy and Related Phenomena **75**, 273-297 (1995).

[6] J. J. Barton, C. C. Bahr, Z. Hussain, *et al.*, Phys. Rev. Lett. **51**, 272-275 (1983).

[7] J. J. Barton, C. C. Bahr, S. W. Robey, *et al.*, Phys. Rev. B **34**, 3807-3819 (1986).

[8] L. J. Terminnello, X. S. Zhang, S. Kin, *et al.*, Physical Review B **38**, 3879-91 (1988).

[9] L.-Q. Wang, A. E. Schach von Wittenau, Z. G. Ji, *et al.*, Physical Review B (Condensed Matter) **44**, 1292-1305 (1991)

[10] L.-Q. Wang, Z. Hussain, Z. Q. Huang, *et al.*, Physical Review B (Condensed Matter) **44**, 13711-19 (1991).

[11] X. S. Zhang, L. J. Terminello, A. E. S. v. Wittenau, *et al.*, (Lawrence Berkeley National Laboratory, 1987).

[12] X. S. Zhang, L. J. Terminello, S. Kim, *et al.*, J. Chem. Phys. **89**, 6538-6546 (1988).

[13] Z. Hussain, W. R. A. Huff, S. A. Kellar, *et al.*, Journal of Electron Spectroscopy and Related Phenomena **80**, 401-404 (1996).

[14] R. X. Ynzunza, Ph.D. Thesis (University of California, Davis, 1997).

[15] H. Diamon, Personal Communication, 1995).

[16] J. J. Barton, Ph.D. Thesis (The University of California, Berkeley, 1985).

[17] Y. F. Chen, W. Wu, and D. A. Shirley, (To be published).

[18] J. J. Rehr and R. C. Albers, Physical Review B **41**, 8139-8149 (1990).

[19] S. Tanuma, C. J. Powell, and D. R. Pen, Surface Interface Anal. **20**, 77 (1993).

[20] C. D. Wagner, L. E. Davis, and W. M. Riggs, Surface Interface Anal. **2**, 53(1980).

[21] C. J. Powell, Surface Interface Anal. **7**, 256 (1985).

[22] Z. Huang, (University of California, Berkeley, 1992).

[23] L. Pauling, *The Nature of the Chemical Bond* (Cornell University Press, Ithaca, NY, 1960).

[24] K. A. R. Mitchell, Surface Science **100**, 225-240 (1980).

[25] S. L. Altmann, C. A. Coulson, and W. Hume-Rothery, Proceedings of the Royal Society **A240**, 145 (1957).

I went out to the hazel wood,
Because a fire was in my head,
And cut and peeled a hazel wand,
And hooked a berry on a thread;
And when white moths were on the wing
And moth-like stars were flickering out,
I dropped the berry in the stream
And caught a little silver trout.

When I had laid it on the floor
I went to blow the fire flame,
But something rustled on the floor,
And some one called me by my name:
It had become a glimmering girl
With apple blossoms in her hair
Who called me by my name and ran
And faded through the brightening air.

Though I am old with wandering
Through hollow lands and hilly lands,
I will find out where she has gone,
And kiss her lips, and take her hands,
And walk along long dappled grass,
And pluck til time and times are done,
The silver apples of the moon,
The golden apples of the sun.

–W.B. Yeats,
"The song of Wandering Aengus"

CHAPTER 5

REDESIGN OF THE ARPES LENS SYSTEM AND POWER SUPPLIES

I. Introduction

The purpose of this redesign of the old angle-resolved photo-emission spectroscopy (ARPES) analyzer lens system and power supplies is to take full advantage of the very small spot size and excellent energy resolution provided by the new third generation synchrotron light sources like the Advanced Light Source(ALS) in Berkeley[1]. For example, beamline 9.3.2 at the ALS has a photon energy resolving power of nearly 10,000 over the energy range from 30 eV to 1500 eV and a photon spot size that is about 500 μm in diameter, while the undulator beamlines have comparable energy resolution and spot sizes on the order of tens of microns[2]. In order to match the analyzer performance to the beamline performance, it was necessary to redesign and build a new lens system and power supplies and to slightly change the configuration and wiring of the analyzer. The goal is to have an analyzer that has an energy resolution of less than 20 meV with a large throughput. We also wanted to have direct control over the len's linear magnification for photoemission microscopy, and angular magnification for angle-resolved studies of valence bands and core levels. Lastly, to truly utilize the brightness at the ALS, we wanted to be able to take spectra on a millisecond time scale for time resolved X-ray photoemission studies. The ALS can provide enough photons to accommodate such count rates, the challenge is to build power supplies that can scan the analyzer voltages quickly enough. In addition of course, there is also a need for detectors that can handle these high count rates without saturation. Such a detector is under construction as a joint project between Lawrence Berkeley National Laboratory (LBNL) and a private firm, Quantar Technology, but I only mention it here and direct those who are

interested to reference[3] Lastly the ARPES system serves as a testbed for these new designs that we then hope to incorporate into larger electron energy analyzers.

This chapter is broken down into the three major steps of the ARPES system retrofit. Section II will briefly describe the original lens system and its limitations, then describe the new lens system and how it solves these problems. This section will include a discussion of the important aspects in matching the photon source to the hemispherical electron energy analyzer system to optimize performance. Section III deals with the new power supplies, Section IV describes the physical changes we made to the existing ARPES system to improve the signal to background ratio and resolution. Finally section V suggests additional improvements to be made in the future. In this thesis, when speaking of electrons, the terms voltage (or potential) and kinetic energy will be used interchangeablely. While this is of course not strictly correct, it is conveinent and I ask the reader's indulgence with this terminology.

II Lens system

The first important step is to match the performance of the lens and analyzer combination to the photon source. The requirements were set to obtain very high and independently variable energy and angular resolution at electron kinetic energies up to 1 keV, while still maintaining a large throughput. As I will show later in this section very high angular resolution is a necessary condition for good energy resolution. Also the smaller the photon spot size the more we win with both resolution and throughput.

If the photon beam is focused to a spot size of diameter w_s on the sample, and as many electrons as possible are to be collected, then the lens system must image this entire spot onto the analyzer entrance aperture, w_a. Ignoring higher-order terms, the resolution of a hemispherical analyzer is given by[4,5]

$$\Delta E = \frac{w_a}{2r_0} E_p \tag{1}$$

where E_p is the pass energy and r_0 is the mean radius of the analyzer. In the present analyzer the radius is fixed at 54 mm. While the radius is fixed by the physical constraints of the vacuum chamber, Eqn. 1 suggests that even with a small radius analyzer one could still obtain the desired resolution by varying the size of the entrance slit or the pass energy with a judicious choice of lens parameters. Unfortunately this is not the case, because the spherical aberrations of the analyzer eventually dominate the absolute resolving power. The electrons enter the analyzer within a cone of half angle, a_a, given by the Helmholtz-Lagrange phase space relation as[6]

$$\alpha_a = \alpha_s \frac{w_s}{w_a} \left[\frac{E_p}{E_k} \right]^{-\frac{1}{2}} \tag{2}$$

where a_s is the angular spread of electrons accepted by the lens and E_k is the kinetic energy of the electrons ejected from the sample. Fig. 1 shows the important lens and analyzer dimensions. If we maintain a constant pass energy and a constant acceptance angle from the sample, then for a given kinetic energy and photon beam spot size, arbitrarily decreasing the size of the analyzer entrance slit, w_a, or the pass energy, E_p, increases the angle at which the electrons enter the analyzer, a_a. The hemispherical analyzer's spherical aberrations increase as the cube of the angle, a_a, so keeping this angle as small as possible allows one to more closely approach the theoretical resolving power given in Eqn 1. This argument applies to the angle that the electrons entering the analyzer make with respect to the dispersion direction. In the non-dispersion direction the requirement on angular resolution is greatly relaxed, and typically the entrance aperture is a slit with the dimension in the non-dispersion direction an order of magnitude larger than in the that in the dispersion direction. Kuyatt and Simpson suggest the following criterion for controlling the spherical aberrations[7]

$$\alpha_a^2 \leq \frac{w_a}{4r_0} \tag{3}$$

With r_0 fixed at 54 mm, there is then a fundamental limit on the lens system demagnification and the ratio of the electron kinetic energy to the pass energy in order to obtain the best possible resolution.

The size of the analyzer entrance slit is chosen to give the desired resolving power, $\Delta E/E$, and at the same time to allow a convenient minimum value in the ratio of the pass energy to kinetic energy, E_p/E_k, while satisfying Eqn. 3. If we set the size of the entrance slit to 500 μm then at a pass energy of 4 eV the theoretical resolution, from Eqn. 1, is less than 20 meV. The focused photon spot size at the endstation of beamline 9.3.2 is, from Huff's thesis, 400 μm x 500 μm so the overall linear magnification, w_a/w_s of the lens system must be negative one[2]. The negative value indicates an inverted image. If we then design the lens to have an angular resolution of $\pm$1.0 degree, the ratio of the pass energy to electron kinetic energy, E_p/E_k must be more than about 0.17 to satisfy Eqn. 3. This means that at the lowest pass energy of 4 eV, the maximum kinetic energy at which we can expect to have the best possible resolution is 240 eV and, at a pass energy of 16 eV the maximum kinetic energy is 960 eV. It is important to appreciate the importance of very high angular resolution in obtaining very high energy resolution. This also means that the smaller photon spot sizes offer either better energy resolution or comparable energy resolution with greater throughput.

The next step in the retrofit was to design a lens system with constant unit magnification between the sample and the analyzer entrance slit over a wide range of

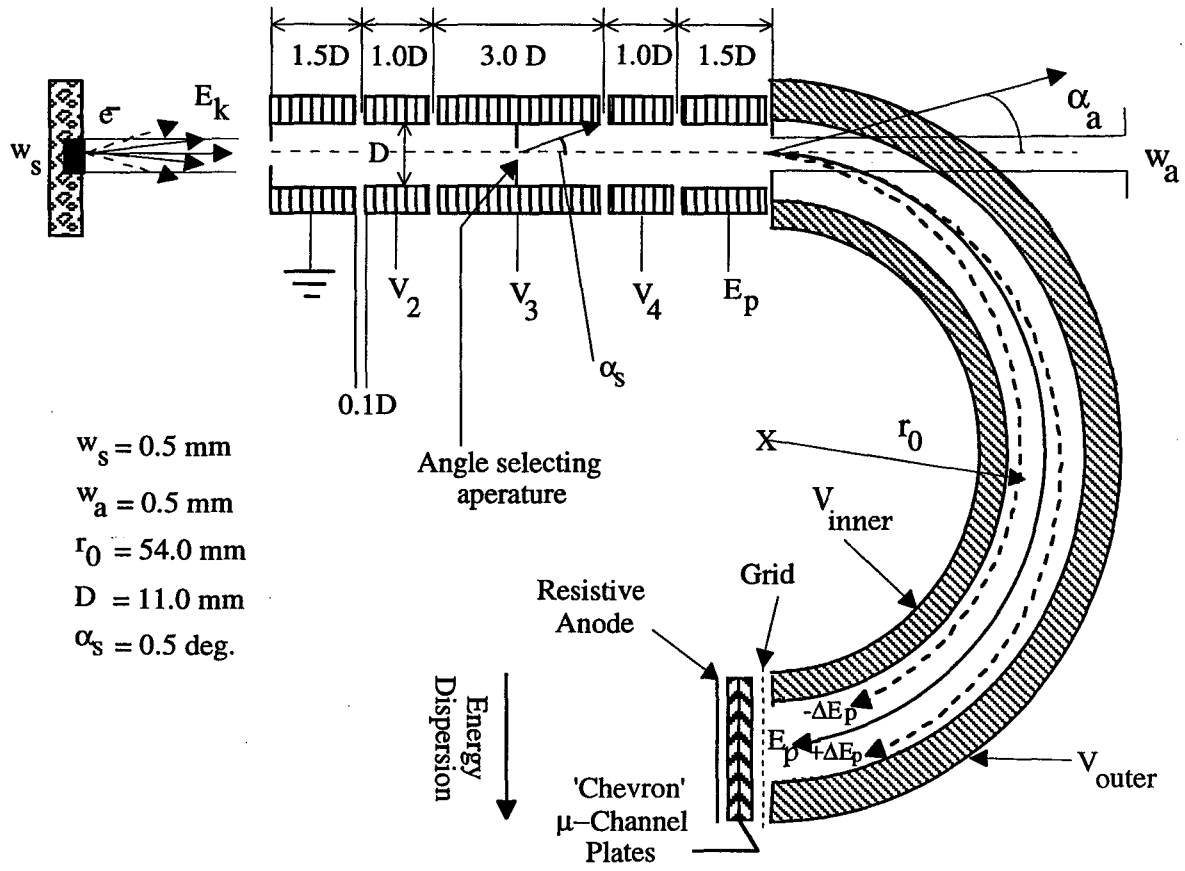

Figure 1. Schematic of the ARPES electron energy analzyer and lens system showing important dimensions referenced in text.

accelerating and retarding ratios. The original design consisted of two, three element einzel lenses in combination with an aperture lens[1]. The voltages for each lens element were supplied by a voltage divider network, which necessitated that the universal focusing curves be approximated as linear. Moreover it was assumed that the focusing curves were the same for every pass energy. This clearly is not the case and the new design allows for each of the four focusing voltages to be independently computer controlled. The original design required the aperture lens to do most of the retardation, operating at 86% of the analyzer mid-plane voltage. This configuration at even moderate retardation ratios, causes a large expansion of the beam inside the lens, so that the filling factor approaches 80%. The filling factor is defined as the ratio of the beam size at the gap between electrodes to the diameter of the lens elements. Read suggests filling factors of less than 50% to keep aberrations to a minimum[8]. Also there is no control over the magnification, so that the lens system does not have constant magnification for each ratio of pass energy to kinetic energy. One method of correcting this problem is to use asymmetric voltage, three element lenses for which Harding and Read have computed and tabu-

lated focal lengths[8]. These lenses can focus and reduce the electron kinetic energy down to the analyzer pass energy. The problem with these lenses is that for retardation ratios greater than 10:1 they have severe aberrations[1,8]. Also, with only two adjustable parameters it is not possible to control the magnification and the retardation value, though it is possible to choose a voltage ratio range where the magnification is constant within ±5%. We decided to use the five element lens first tested and characterized by Heddle which allows independent control of both the linear and angular magnification at arbitrary retardation ratios with smaller aberrations than the three element lens[9].

The lens consists of five, cylindrically symmetric tubes machined from a monolithic piece of aluminum to ensure concentricity of the inner diameters. The tube was then cut and machined to give the 5 elements with the proper length as shown in Fig. 1. The tube inner diameter, D, is 11.05 mm, the spacing between elements is 0.1D, or 1.1 mm. The lengths of each element are as follows: $L_1 = L_5 = 1.5D$, $L_2 = L_4 = 1D$, $L_3 = 3.0D$. The spacers between each element were machined from Macor™ with tolerances of ± 25 μm because the stacking height of the various elements, and the gap size are critical for proper lens performance. See Fig. 1 for a schematic of the lens dimensions. The inside of each element was then coated with Aerodag™, a colloidal suspension of graphite in isopropyl alcohol dispensed from an aerosol can. The graphite coating is important for maintaining a constant work function and therefore a constant field throughout the lens and analyzer system. Bare Aluminum and bare stanless steel in particular, are undesireable becuase they are known to exhibit large 'patch' affects. These patch affects are caused by surface cyrstallites with differring crystal orientations producing inhomogeneos fields because of their differing work functions. The graphite coating produces a uniform work fucntion and field throughout the lens and analzyer.

For a five-element lens with these dimensions Trager-Cowan *et al.* developed a parameterization to calculate the focusing potentials given the overall voltage ratio and the desired linear magnification[10]. For this parameterization all voltages are measured from the cathode potential, or that voltage at which the photoelectrons emitted from the sample would have zero kinetic energy. V_1 is the electron kinetic energy, E_k, and the first element is then held at ground potential to avoid an further acceleration of the electron. V_5 is the pass energy, which is the energy that an electron must have to follow the mean radius through the analyzer. The voltage on the long, intermediate element, V_3, is always maintained at $\sqrt{V_5/V_1}$, or $\sqrt{E_p/E_k}$. With three of the five voltages predetermined by the experimental conditions, the two remaining voltages, V_2 and V_4 are used to set the magnification. The parameterization is a function of the overall retardation ratio of the lens, E_p/E_k, and the magnification, M. It is this ratio that as mentioned before must be more than ~0.17 for the analyzer to work at the highest possible energy resolution. The two equations for the parameterization follow:

$$V_2/E_k = P(E_p/E_k)(R\sin\theta)^{-E(E_p/E_k)} \tag{4}$$

$$V_4/E_p = \frac{1}{P(E_p/E_k)}(R\cos\theta)^{-E(E_p/E_k)} \tag{5}$$

Where E_p/E_k is the retardation ratio, R is a scaling parameter which for the dimensions of this lens described above and in Fig. 1 is 5.55, and q is given by

$$\mathrm{Tan}\theta = \mathrm{Tan}\Phi^{E(E_p/E_k)} \tag{6}$$

$$\Phi = 1.2\log(-M) + \varphi(E_p/E_k) \tag{7}$$

M is linear magnification. The curves for the functions $\varphi(E_p / E_k)$, $E(E_p / E_k)$, and $P(E_p / E_k)$ are taken from Trager-Cowan and reproduced in Fig. 2[10]. Using these curves and Eqns. 4-7 we can find the focusing voltage curves for both V_2 and V_4. These curves are shown in Fig. 3 for the pass energies 4,8,16, 32, and 64 eV.

The accuracy of these curves was then tested with the electron ray tracing program, SIMION[11]. I used a 3200 x 205 point potential array with cylindrical symmetry for these calculations. When using SIMION it is important to check that one has a large enough grid point density to make the calculations meaningful. To ensure that I met this requirement, I ran several calculations with the same initial electron and lens voltage parameters doubling the size of the potential array for each successive calculation until the electron trajectories were the same for two potential arrays. For the final ray tracings I used the largest of these arrays, 3200 x 205 points.

I tested the overall magnification of the lens at each pass energy for 10 different electron initial kinetic energies, using an energy range that was appropriate for the pass energy. The ray tracings showed that the Trager-Cowan parameterization is quite accurate. Where the overall magnification differed from unity, I altered the potential on the V_4 element until the magnification was again -1. An example of these small corrections is shown in Fig. 4 for the E_p = 4 eV case. Using these corrected voltages we constructed curves for each pass energy that were then fit with a cubic spline to determine the necessary voltages while scanning that particular lens element voltage during the data collection.

Fig. 5 shows examples of the ray tracing calculations for both the old and new lens systems. The ray tracings represent three different initial experimental conditions for the electron kinetic energy and pass energy. The electron source size for all calculations is 1 mm and the same size potential array and scaling are used for both the old and new lens calculations. Panel (a) shows the trajectories for electrons with an initial kinetic energy of 40 eV and a pass energy of 4 eV ; in panel (b) E_k = 160 eV and E_p = 32 eV; and in panel (c) E_k = 32 eV and E_p = 16 eV. Obviously the

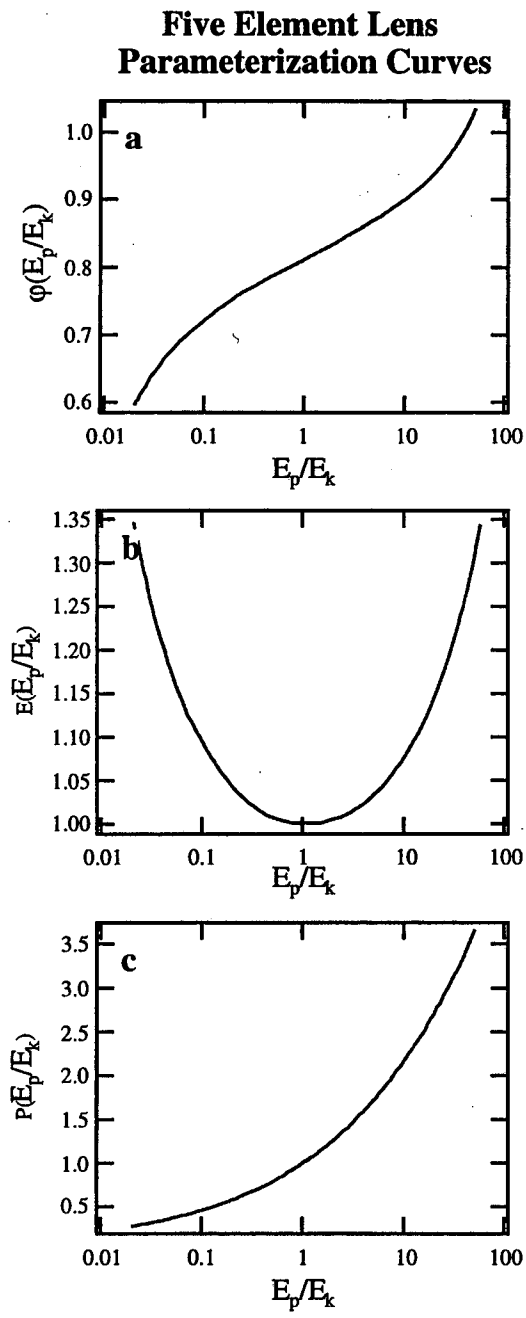

Figure 2. Trager-Cowan *et al.* curves used in the parameterization determining the lens voltage ratios V2/Ek and V4/Ep. a) j(Ep/Ek), b) E(Ep/Ek), and c) P(Ep/Ek) From Trager-Cowan *et al*[10]

magnification for the old lens is never constant while, for the new lens it is very close to unity over a wide range of experimental conditions. Also the ray tracings show that in the new lens the filling factor is less than 30%, which is also much better performance than the original lens.

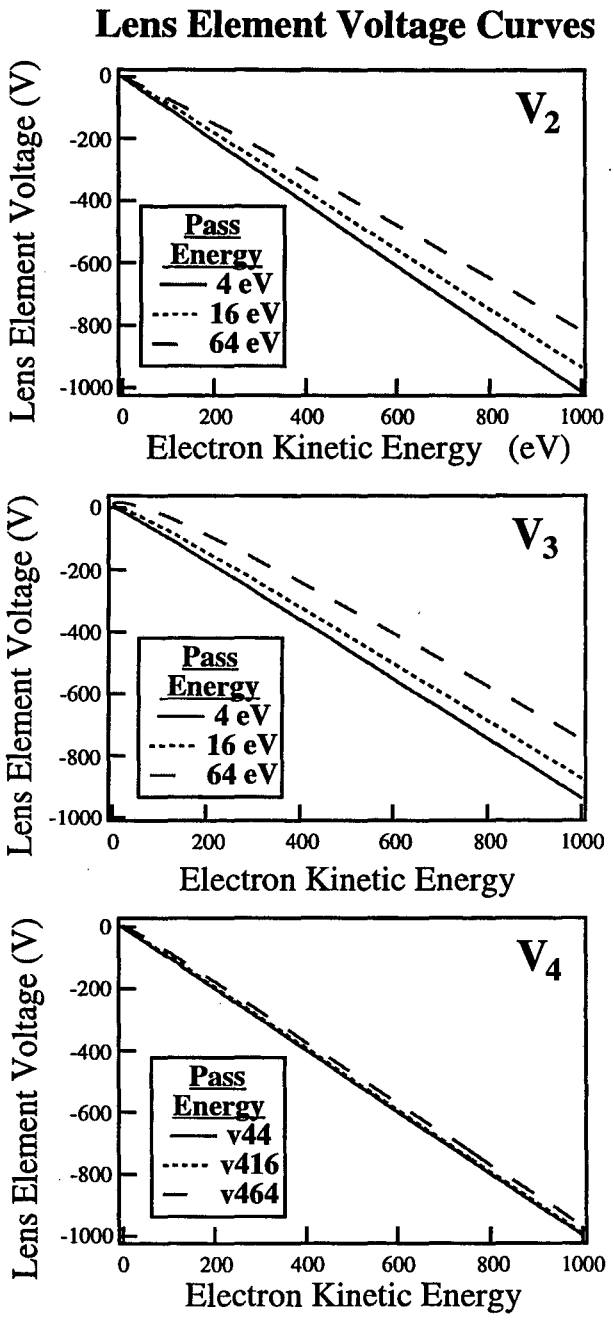

Figure 3. The voltage curves for lens elements 2, 3, and 4 at constant linear magnification, M = -1, plotted as a function of electron kinetic energy, E_k, for five pass energies (4, 8, 16, 32, and 64 eV)

Another attractive feature of this five element lens design is that one can operate it at constant angular magnification. This constant angular magnification is especially important for valence band studies and when using the angle-resolved photoemission fine structure (ARPEFS) technique which is discussed and used in

detail in this thesis. The Trager-Cowan parameterization does not consider the angular magnification, to determine the focusing curves for this mode one uses the original Heddle paper and his Fig. 9 reproduced here as Fig. 6[9]. This diagram shows lines of constant linear, constant angular, and overall voltage ratio of the five element lens. The values for the ratios of V_2/E_k and V_4/E_k are read off for any combination of two of the three parameters. Fig. 7 shows the linear magnification required to produce unit angular magnification, M_a, for a given retardation value[9]. Using these two curves I calculated the focusing curves for elements 2 and 4 as a function of electron kinetic energy for $M_a = -1$. These lens element voltage curves are shown in Fig. 8. The lens can be operated in a mode where the angular acceptance is always ±1.0 degree. The range over which the lens can be used in this mode

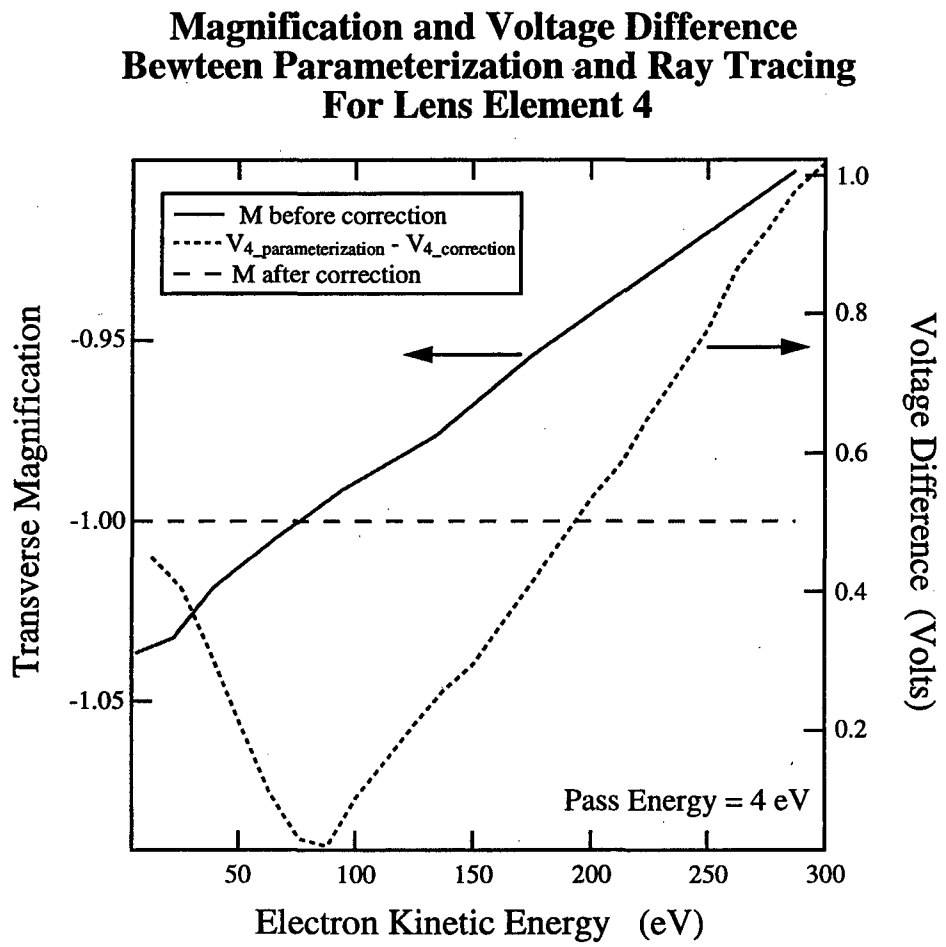

Figure 4. The voltage on lens element 4 determined from the Trager-Cowan parameterization and the correction to that voltage determine by ray tracing with SIMION. This is the V_4 curve for a pass energy of 4 eV. This shows that the requirements on the power supply performance is very high.

is limited however. As Fig. 9 shows, for smaller pass energies the useful kinetic energy range is small, less than 300 eV. The reason for this is that the parameterization (Eqn 6) involves Tan θ which blows up near $\theta = \pi/2$. Also, as the dashed lines in Fig. 8 indicate, the value for linear magnification where one can have constant angular magnification is limited by the lens aberations, especially for lenses working in redardation regions. These limitations, however are not necessarily severe. When one wishes to have constant angular magnification for valence band studies usually one is also working at maximum resolution, that is at a pass energy equal to 4 eV, and one rarely needs to take spectra at kinetic energies greater than 100 eV. For ARPEFS studies, resolution is generally not a major concern so that one can

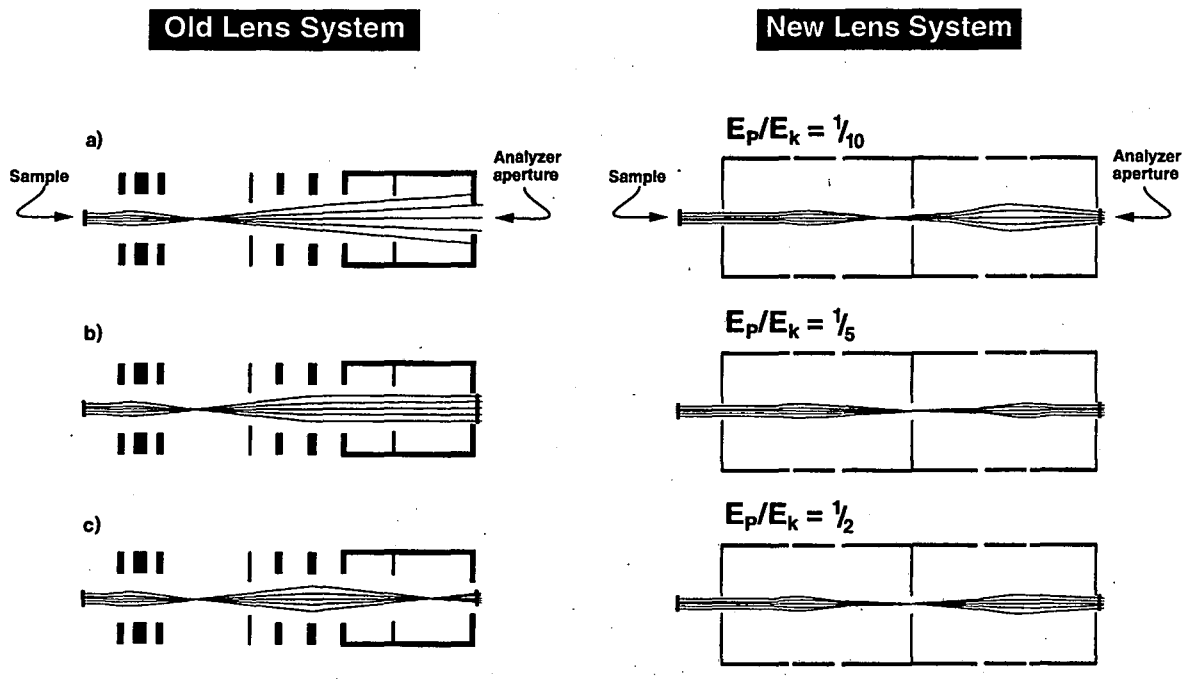

Figure 5. SIMION ray tracing of the old and new lens systems depicting the transverse magnification for three initial experimental conditions. a) Ek = 40 eV, Ep = 4 eV b) Ek = 160 eV, Ep = 32 eV c) Ek = 32 eV, Ep = 16 eV. The intial spot size for all ray tracings is 1 mm.

operate the analyzer at pass energies of 32 eV and larger in order to cover the typical ARPEFS energy range (approximately 500 eV) with constant angular magnification.

III. Power Supplies

The power supplies were designed with several criteria in mind.

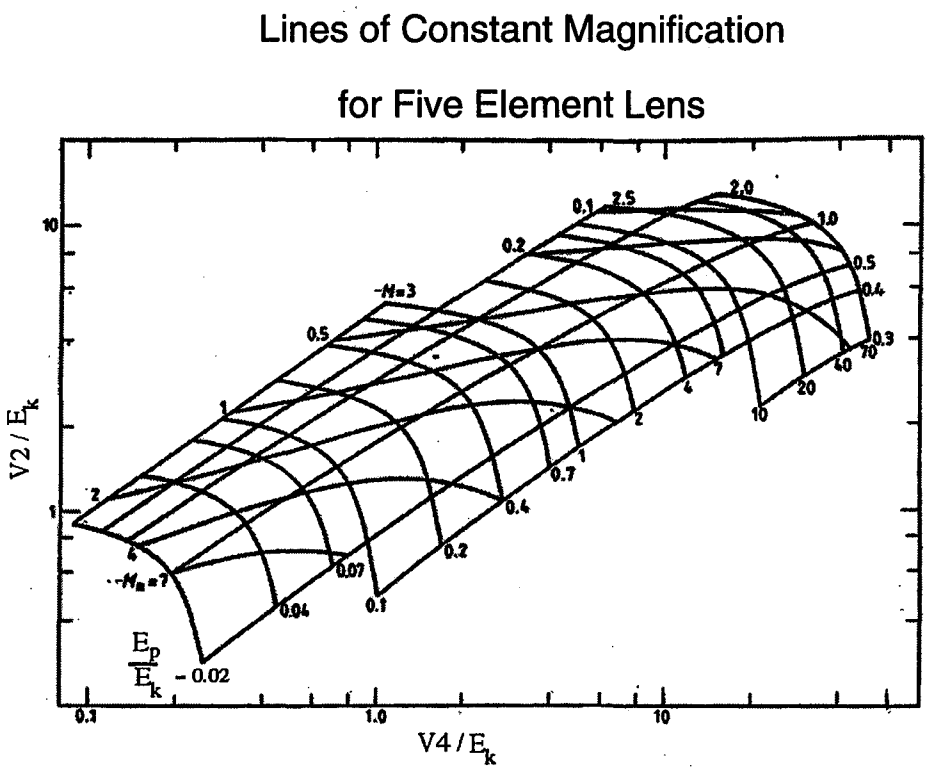

Figure 6. Lines of constant transverse magnification, constant angular magnification, and overall voltage ratio, E_p/E_k, for the five element lens. Value of V_2/E_k and V_4/E_k can be read off for any chosen combination of two of the three parameters. From Heddle[9]

1) Computer Control: The supplies should be computer controlled with at least 16 bit resolution so that focusing voltage curves could be followed accurately and the minimum step size is about one tenth the expected resolution of the analyzer.

2) Stability and Linearity: The output voltage should have no more than 1ppm of AC ripple over the full range of the supply (up to 1 kV), and the linearity over the voltage range should also be 1ppm.

3) Reproducibility: The supplies need to be setable to better than 10 ppm from day to day.

4) Fast Scan Rate. Unfortunately, the last requirement works against attaining the others, but we wish to be able to scan the supplies on the order of 1 msec. That is their settling time should be less than 10 msec.

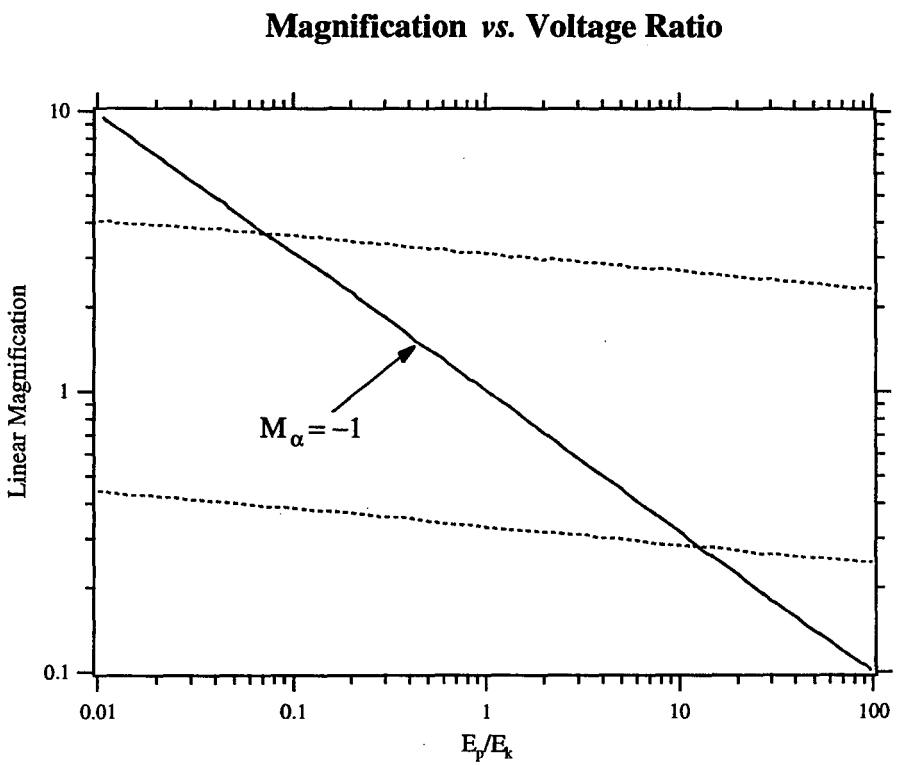

Figure 7. Linear Magnification plotted as a function of the overall voltage ratio, E_p/E_k. The dashed lines are the upper and lower limits Heddle suggests to control aberrations. The solid line shows the linear magnification required to give unit angular magnification. From Heddle[9].

5) Thermal Stability: The supplies are stable to thermal fluctuations to 1.5 ppm/degree C.

A schematic of the power supply system is shown in Fig. 9. The figure shows the four computer controlled output voltages, V_1, V_2, V_3, V_4 arranged into four groups. Each of these output voltages is the sum of a high resolution (Hi Res) and a low resolution (Low Res) component. For each output voltage there is one, two sided 16 bit Digital to Analog converter (DAC). One side of each DAC is for low resolution, with 16 bits or 1/65535 spanning the entire range of the supply. V_1 ranges from range -2.3 to -850 V so the minimum step size is 13 mV. The other half of the DAC is the Hi Res side with a gain ten times that of the low resolution side. So for V_1 the minimum step size of the Hi Res DAC is 1.3 mV. This gives us approximately 19 bit resolution on the output voltage for all the computer controlled supplies. The true output voltage is the sum of the Hi Res and the Low Res components. This minimum step size is important not only for high resolution spectra, but also because the supplies stack the previous supply to produce the voltage for the next voltage element. It is critical that the error in this stacking be as small as possible for correct focusing of the lens.

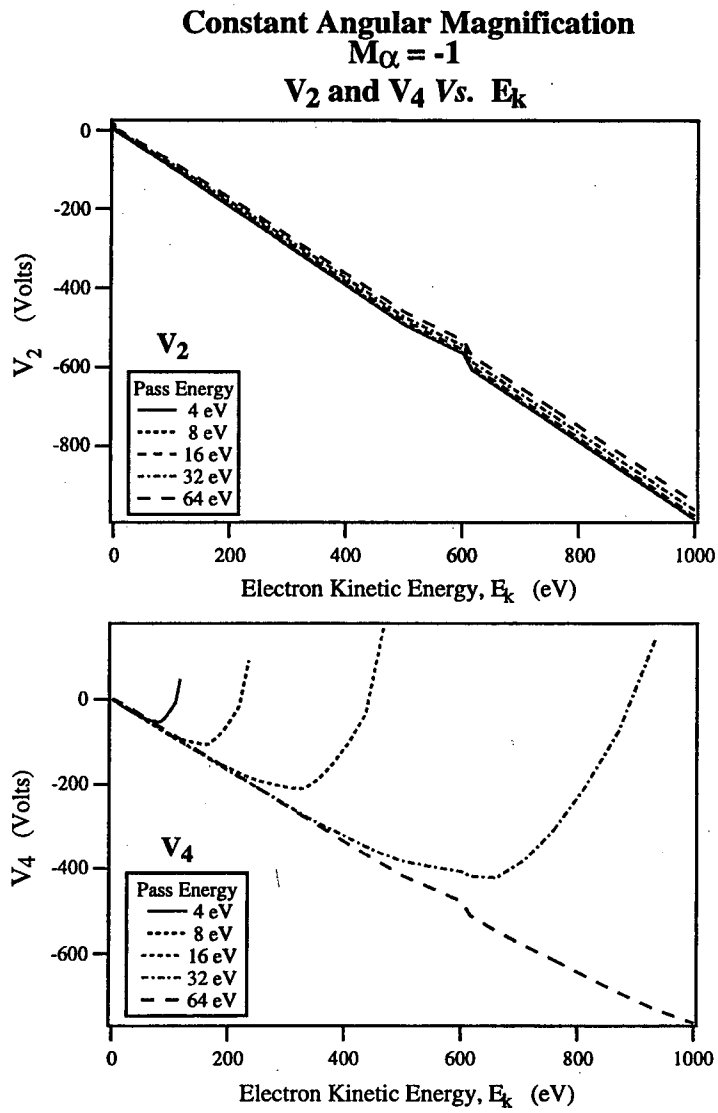

Figure 8. V_2 and V_4 voltage curves for constant angular magnification, $M_a = -1$. The curve for V_3 is the same as for constant linear magnification.

The analyzer voltages are produced by one of four power supply groups, numbered 0 -3. (Figs. 9 and 10) As Fig. 10 shows, each group has its own floating, isolated supply that provides the DC power for the op-amps that produce that group's voltages. The supplies and isolation transformers are segregated into a separate chassis from the analyzer voltage supplies to prevent any magnetic coupling. Only DC voltages come out of the first chassis as input for the op-amps in the analyzer voltge chassis. This second chassis houses the DACs and op-amps for each analyzer and lens voltage. The voltages are controlled by a 24 bit word from a Macintosh computer equipped with a digital I/O (input/ouput) board. To avoid ground loops and other noise sources the computer is optically isolated from the

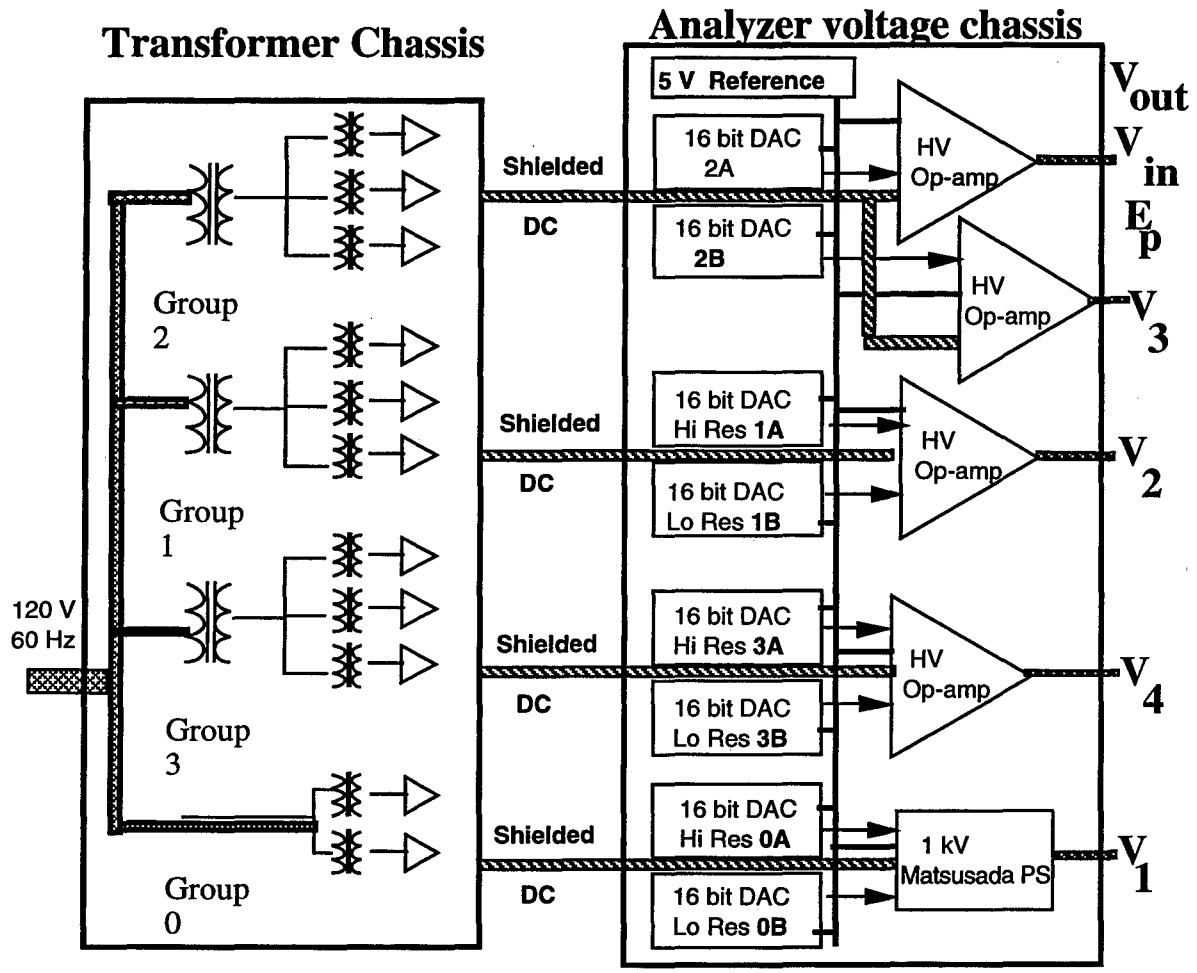

Figure 9. Schematic layout of the power supply groups and output voltages.

supplies. This 24 bit word consists of 16 bits for the voltage value and 8 bits to designate which voltage to set and at what resolution level (high or low).

The settling time, t_{RC} of the supplies is less than one millisecond, and the time necessary for the supplies to settle to the 16 bit level is ~$5t_{RC}$, about one msec. Of course, if we plan to scan at 1 kHz rates, resolution is probably not a great concern and therefore it would not necessary to wait the full $5t_{RC}$ before stepping to the next voltage. In order to obtain this rapid settling time all the voltages which are computer controlled are provided by op amps instead of divider strings. While the op amps allow for a faster supply, for accurate voltages they require a very accurate and quite reference voltage. We chose to use Analog Devices A3383 chip as the reference voltage supply[12]. It's specifications are for less than six μV peak to peak

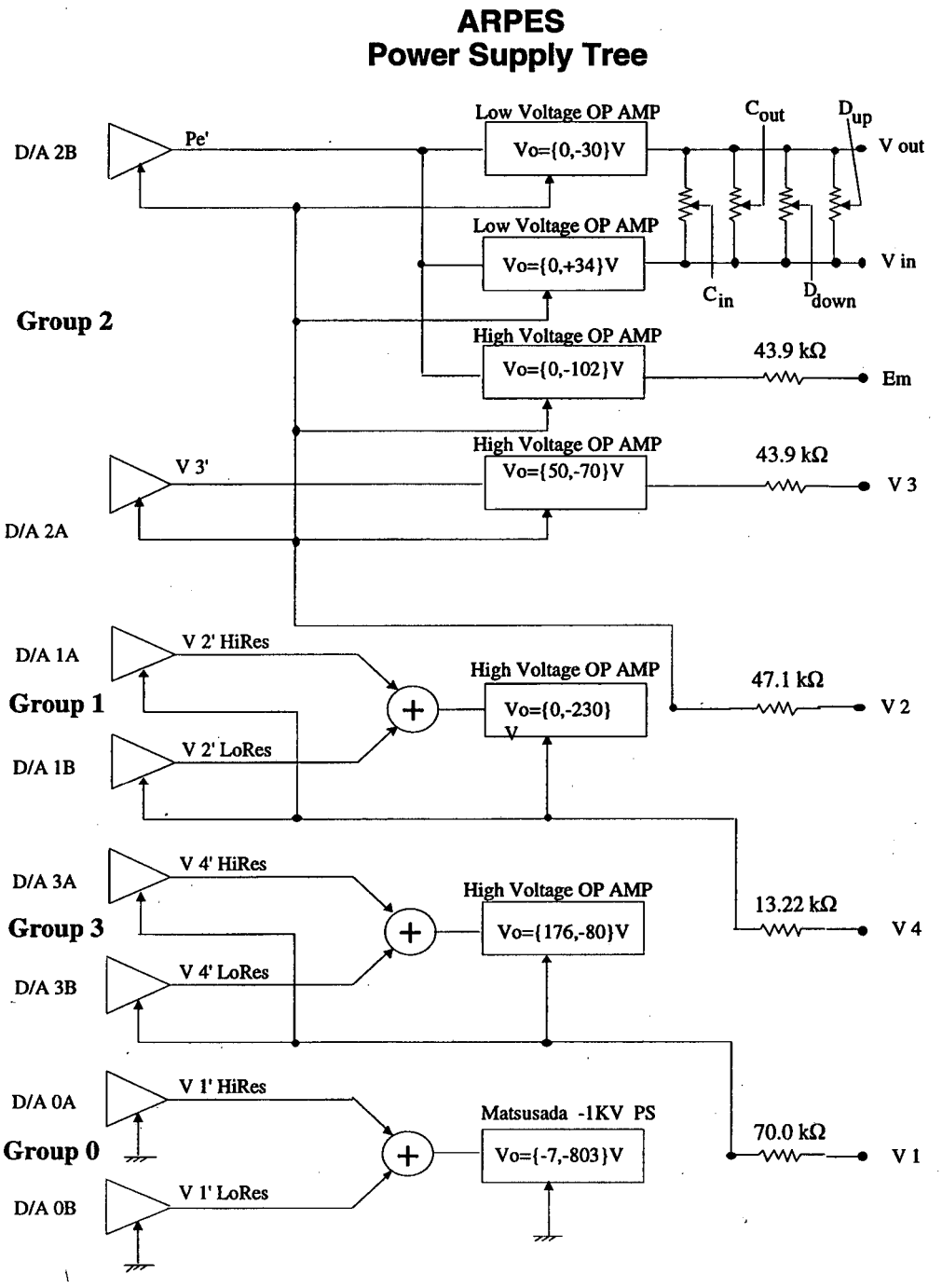

Figure 10. New APRES Power supply Tree

noise at five volts or less than 1ppm rms ripple. This is important because any noise here is amplified in the same proportion as the voltage coming out of the op-amp so a little noise can become significant. This supply is also used as the DAC reference to assure the voltage linearity. One other concern with using op-amps is

that they are often unstable when used with only capacitive loads, as is the case here. Much care was taken to smooth and filter the output below the 1ppm ripple level. Also, the internal resistance for supplies is kept as low as possible to enable the scan rates around 1 kHz. This small impedance is only a problem when calibrating the supplies.

Once the supplies were built the next step was to calibrate them. We measured the output voltage as a function of DAC step with a temperature calibrated voltmeter with 10 MΩ internal resistance, however because the power supplies can source so little current even this load was sufficient to cause the supplies to sag. We converted the measure voltage, V_m, to the true open circuit voltage, V_{oc} using Eqn. 4. R_m and R_i are the internal resistance of the meter and supply respectively.

$$V_{oc} = V_m \frac{R_m + R_i}{R_m} \tag{8}$$

The open circuit voltage surface is shown in Fig. 11 as a function of the Hi Res DAC (x scale) and the Low Res DAC (y scale). This figure shows a 'knee', where slope of the voltage *vs.* DAC step curve is flat, at the extreme edges of the DAC range. In practice, we stay away from these edges when scanning the lens and analyzer element voltages.

This voltage surface is divided into 15 slices equally spaced in Low Res DAC steps. The spacing for these slices was chosen to be slightly less than half of the range of the Hi Res DAC. This scheme allows us to cover the entire voltage surface with high resolution steps. When taking spectra then the computer code selects the appropriate Low Res DAC slice and then scans the Hi Res DAC to take spectra. If the desired kinetic energy range of the spectra is greater than the range available from the Hi Res DAC, the scanning stops, the computer switches the Low Res DAC to the next slice and resumes scanning with the Hi Res DAC.

IV. Analyzer Changes

A number of small physical changes was made to the old analyzer to improve the signal to background ratio and the resolving power.

1) The most significant of these was the removal of the field termination strips. These were 5 copper wires isolated from each other and from the analyzer hemispheres by an alumina spacer, see Kevan's thesis for a picture. The strips were used to maintain, as closely as possible, the spherical field at the exit plane of the analyzer. However, after considerable discussion, we were convinced that the perfect spherical field was not a necessary condition for high resolution and that the ce-

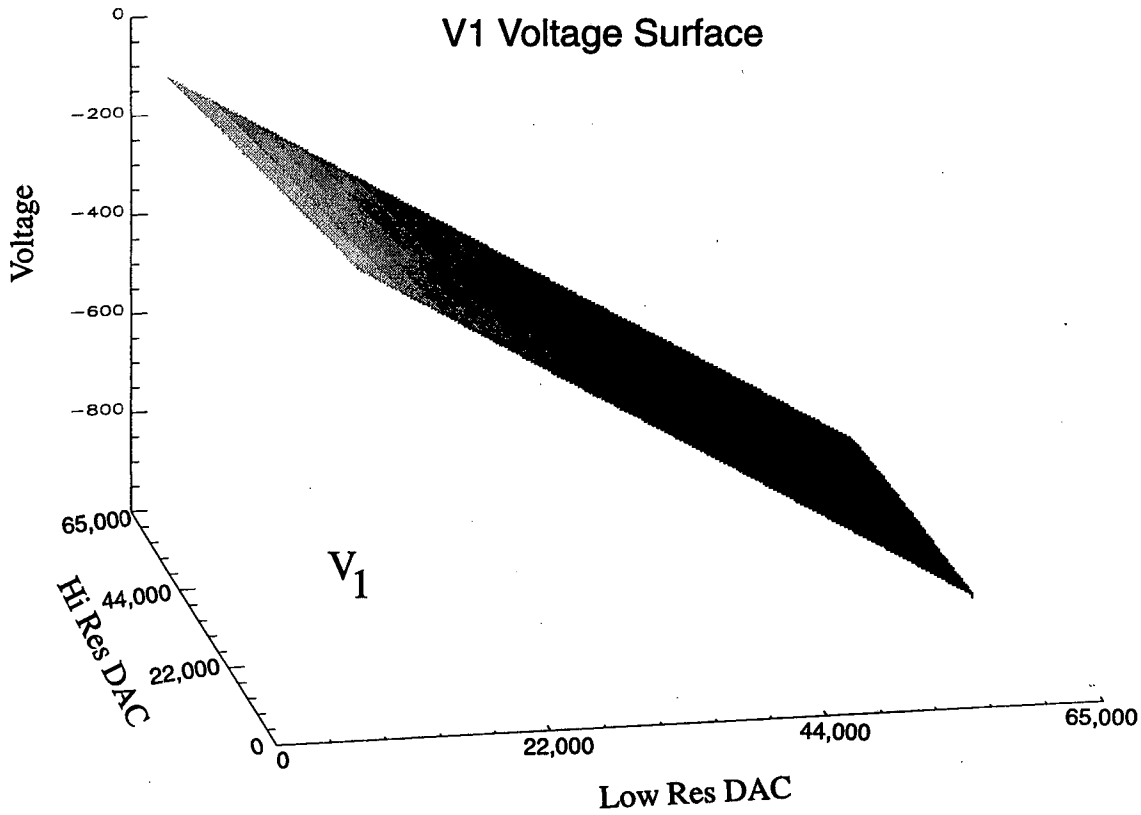

Figure 11. V_1 voltage surface plotted as a function of the Low and Hi Resolution DACs. The DACs range from 0 to 65535 steps.

ramics and wires served as an unwanted source of scattered electrons, increasing the background signal[13, 14].

2) Baltzer *et al* demonstrated that it is not necessary to perfectly maintain this spherical field at the exit plane if one has the ability to alter the electrons trajectory in the analyzer[13]. To be able to change the path of the electrons, I moved two of the termination strips to just behind the entrance slit. The potential on these was then controlled by two, ten-turn pots on the front of the power supplies, labeled C_{in} and C_{out}. Their voltage is a variable fraction of the pass energy. One can then dial in voltages to push the analyzer's focal plane out to the detector plane. Quite generally this method can correct many other manufacturing imperfections in the analyzer, such as a misalignment of the hemispheres.

3) The original entrance slit to the analyzer was straight. The analyzer produces a curved image of this straight slit on the detector plane, thereby degrading the resolution because the multichannel detection scheme assumes a linear dispersion

Contour and Image plot of the V_1 Voltage Surface

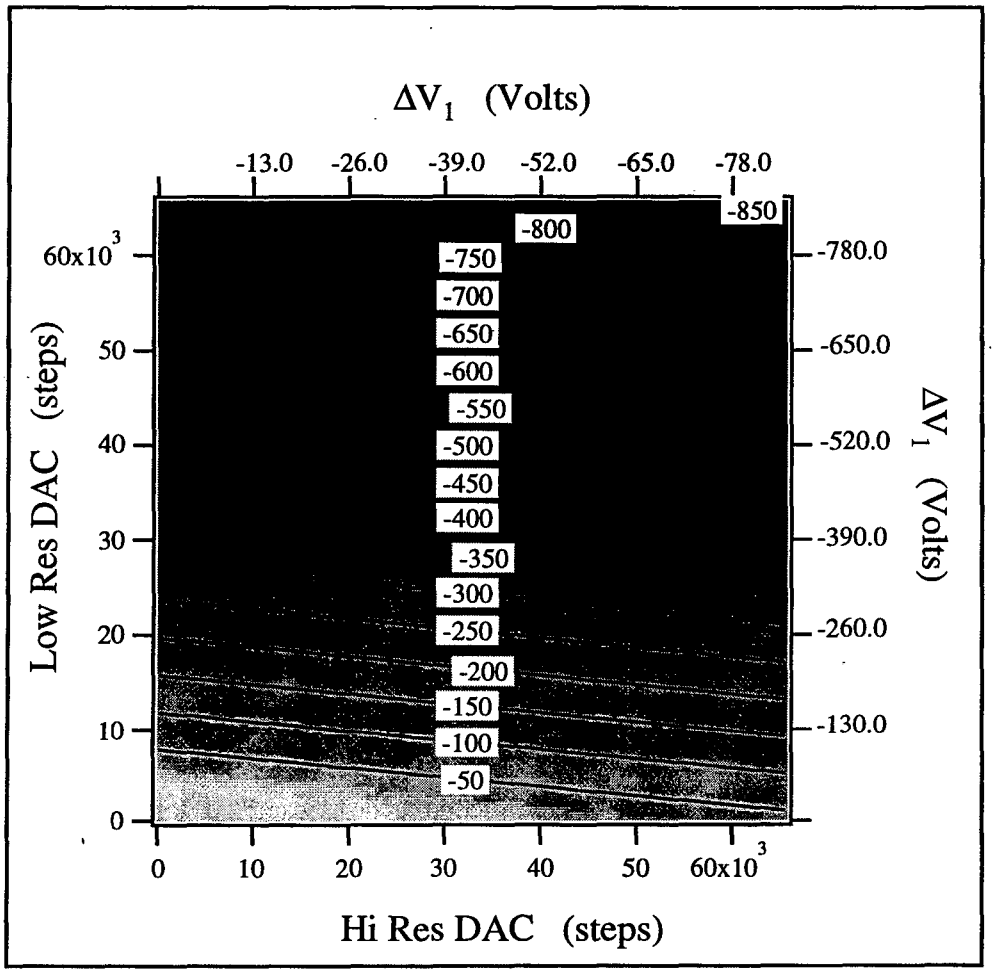

Figure 12. Contour and Image plot of the V_1 voltage surface vs Hi and Low Res DAC steps. The contour lines represent the slices through the surface at contant Low Res DAC setting about which the Hi Res DAC is scanned during data collection.

on the resistive anode[5]. We replaced this with a curved slit of 25 mm radius, so as to have a straight line imaged onto the detector.

4) In the past, the electrons coming out of the analyzer were accelerated between the back of the analyzer and the front channel plate. This acceleration led to an increased background because it collects all the secondary, scattered electrons produced by electron impact inside the hemispheres and at the exit plane. Now the electrons coming out of the back of the analyzer are retarded down to about 10 eV kinetic energy. This retardation has two positive results. First we lower the background by throwing away secondaries, and secondly we increase the detection

efficiency of the channel plates. The channel plates are most efficient for electrons at impinging at kinetic energies of 10-20 eV[13, 15].

V Future Improvements

The most obvious future improvement is to replace the fixed analyzer entrance aperture with a turntable fixture that allows for the selection of one slit from several available slits in vacuum. Such a device will make the analyzer system more portable from one beamline to another where the photon spot size may be an order of magnitude smaller than that on beamline 9.3.2. Also, such an assembly will allow one to trade off resolution for intensity in many experiments where very high resolution is not important and the sample is dilute or the photoemission signal is otherwise weak.

The second major improvement is in the lens system. The careful reader will realize that with the five element lens it should in principle be possible to control three important experimental parameters at the same time, the retardation ratio, the linear magnification and the angular magnification. While there is no parameterization available with these three parameters as variables, Trager-Cowan *et al.* calculate and tabulate matrix elements for a two-cylinder lens with a gap equal to 10% of the diameter. Assuming that the effect of each inter-electrode gap does not depend on the conditions at neighboring gaps one can treat the four interelectrode gaps of the five element lens as four independent, two element lenses. This assumption should be valid as long as the length of each element is greater than one diameter. Following the matrix methods outlined by Trager-Cowan it is doubtful one could produce a simple parameterization that is a function of all three of the above parameters, however one could eventually produce a set of voltage curves for each pass energy which would satisfy the desired criteria of constant transverse and angular magnification for each retardation value.

Lastly, in the future it would be much more convenient and simple to control the power supplies with a single 19 or 20 bit DAC, eliminating the need for both a high and low resolution section for each programmable voltage. This design with both high and low resolution DACs summing to produce one voltage introduces some uncertainty and error into the calibration which would be best to be avoided in the future.

References

[1] S.D. Kevan, Ph.D. Thesis (University of California, Berkeley, 1980).

[2] W.R.A. Huff, Ph.D. Thesis (University of California, Berkeley, 1996).

[3] J. Zaninovich, Personal Communication , 1996.

[4] S.D. Kevan, Review of Scientific Instruments **54**, 1441-1445 (1983).

[5] J. Osterwalder, M. Sagurton, P.J. Orders, C.S. Fadley, B.D. Hermsmeier, and D.J. Fried man, Journal of Electron Spectroscopy and Related Phenomena **48**, 55-99 (1989).

[6] A.B. El-Kareh. and J.C.J. El-Kareh, *Electron Beams, Lenses, and Optics* (Academic Press, New York, 1970).

[7] C.E. Kuyatt and J.A. Simpson, Review of Scientific Instuments **38**, 103 (1967).

[8] E. Harting and F.H. Read, *Electrostatic Lenses* (Elsevier, Amstrdam, 1976).

[9] D. Heddle and N. Papadovassilakis, Journal of Physics E: Scientific Instruments **17**, 599-605 (1984).

[10] C. Trager-Cowan, S.M. Kay, D.W.O Heddle, Measurment Science and Technology **1**, 747-50 (1990).

[11] D.A. Dahl, SIMION 3D, Idaho Falls, ID, 1995.

[12] Analog Devices, catalogue, 1994.

[13] P. Baltzer, Ph.D. Thesis (Uppsalla University, 1989).

[14] P. Baltzer,Personal Communication, 1994.

[15] Galileo Inc., catalogue, 1993.

He said, "They are feeding on drowned yellow stone flies."

I asked him, "How did you think that out?"...

"All there is to thinking," he said, "is seeing something noticeable which makes you see something you weren't noticing which makes you see something that isn't even visible."

I said to my brother, "Give me a cigarette and say what you mean."

Norman Maclean, A River Runs Through it

CHAPTER 6

CONCLUSIONS

In this last chapter I want to highlight what I feel are the important aspects, the 'take home messages', from this work. This will include a review of the structural studies presented herein, hints as how to conduct these experiments more efficiently in the future, and a look at future applications of the photoelectron diffraction technique.

I. Summary

This dissertation extends the ARPEFS techniques to atomic structural studies using electron diffraction with electrons originating from non-s core levels. This extension is important in that it enables one to study transition metal overlayers, especially ultra-thin films of magnetic materials. The ability to efficiently calculate the diffraction patterns from non-s initials states and compare them to the experimental diffraction curves in a fitting routine was been made possible by a new calculation code developed by our group. Dr. Yu Feng Chen is primarily responsible for this advancement. Next I will review the specific examples of non-s initial state ARPEFS studies in this thesis.

The Fe/Au(100) is an interesting case in that the one monolayer of the substrate Au atoms migrates to the top of the growing Fe layers. This Au monolayer seems to act as a surfactant, allowing the layer-by layer growth of the high surface free energy Fe layer. We found that the Fe grows in a very uniform manner, closely resembling the BCC lattice of the bulk material. The Au monolayer sits in the fourfold hollow sites of the surface-Fe layers, 1.67 ±0.02 Å above the surface plane. Several researchers have expressed interest in this system because the single Fe layers represent nearly perfect two dimensional structures which should exhibit quantum confinement effects. Additionally the thin Fe layers are expected to have enhance magnetic moments.

The studies of the Mn surface alloys of Ni and Cu, show how the complimentary information from ARPEFS and photoelectron holography can be used to elucidate the precise structure and the quality of thin films. Mn forms highly corrugated surface alloys with Ni(001) and Cu(001). These alloys exhibit a c(2x2) LEED

pattern and represent 1/2 monolayer coverage. We have confirmed the corrugation of the surface layer and report that it is 0.24 ±0.02 Å and 0.30 ± 0.04 Å for the Ni(001) and Cu(001) substrates respectively. For the Ni, the second layer shows a contraction from the bulk value of 4% while the Cu retains the bulk spacing. The photoelectron-holography data clearly shows that there is no leakage of the adsorbate Mn into the bulk Ni, while the presence of the forward-focusing peaks indicates that a significant amount of Mn is present in the second Cu layer. Additionally using the angular position of the peaks in the Mn/Cu(001) case we can confirm the large corrugation of the surface layer.

In the tungsten oxide study, we find that inspite of the very different long range order, as measured with LEED, the [(1x1)O/W(110)]x12 and the (2x1)O/W(110) phases of oxygen on W(110) show the same local atomic structure. The oxygen adsorbs into the quasi threefold-hollow site on the W(110) surface 1.21 ± 0.04 Å above the surface plane. The oxygen adsorption site is 0.46 ± 0.02 Å from the center of the unit cell along the $[1\bar{1}0]$ azimuth. The near-surface W layers maintain bulk spacing.

In the last chapter I describe instrumental improvements to the electrostatic electron-lens system used with the hemispherical electron-energy analyzer. This new lens system is capable of maintaining constant transverse or angular magnification through a wide range of pass energy to kinetic energy ratios. The new lens system and power supplies will allow us to take full advantage of the small photon spot sizes and high photon energy resolution available at third-generation synchrotron sources, like the ALS.

II. The Present

Photoelectron diffraction, ARPEFS in particular, has reached the point of being a mature, well-understood technique. The use of ARPEFS to determine the atomic structure of adsorbates and the substrate near-surface region is now nearly routine. The structural studies of the Mn surface alloys, represents perhaps the state-of-the-art in photoelectron diffraction experiments. The collection time for each ARPEFS data set was 30 minutes, while the holography data required less than 45 minutes. Fitting the ARPEFS data to extract the peak intensities was similarly fast, less than one hour. In less than two hours then, one can obtain diffraction curves with which to determine the local surface structure to better than one-tenth of an Angstrom. The theoretical calculations and fitting procedure for the Mn/Cu(001), Mn/Ni(001), as well as the Fe/Au(001) and the O/W(110) data, were all carried out on a Macintosh computer. The fact that these complex calculations can be done in a reasonable time on readily available personal computers speaks highly of the advancements in computer hardware, as well as the intelligence and efficiency of the scattering code developed by Chen, Wu, and Shirley. This code is now available to other researchers, and will run on the Mac, PC, or Unix platforms.

III. Experimental Considerations

This section will highlight the important experimental aspects that one must attend to in order to successfully perform a photoelectron diffraction experiment. The most important aspect is that the surface structure has at least short-range order. Diffraction is not a suitable technique for studying incommensurate surfaces which exhibit long-range order in the LEED patterns. The number of differing scattering geometries will severely attenuate the diffraction oscillations and make a structure determination impossible. That being said, systems without long-range order, but with local order, are excellent choices for diffraction experiments and are inaccessible to LEED. Liquids and gasses which have local order may also be studied with the ARPEFS technique. Indeed, Moler has suggested that such systems would be excellent tests of electron scattering theory.

The second important experimental consideration, is exact knowledge of the emission direction in ARPEFS data. For non-s initial states and strong scatters it is very important to know as accurately as possible the true emission direction. Alignment of the crystal is best accomplished with the forward-focusing peaks in a high-energy hologram. Photoelectron holography is the best way to determine this alignment because it is internally consistent. That is, one determines the surface normal with the same experimental geometry that will be used to collect the ARPEFS data. If one doesn't collect the entire hologram, one should at least orient the crystal in vacuum with polar angle scans, again using the strong forward-focusing features as guides.

The vibration of the substrate and adsorbate atoms about their equilibrium position acts to attenuate the size of the ARPEFS oscillations, especially at large k-values. Therefore, cooling the sample well below the bulk Debye temperature will greatly enhance the signal to noise ratio in the experimental ARPEFS curves and simplify the fitting process. Because surface-Debye temperatures of many materials are as little as 60% of the bulk, cooling is especially important for adsorbate studies. Cooling is also most important for ARPEFS studies, because ARPEFS relies on the long path-length differences associated with back scattering. High-energy photoelectron holography is not affected as much by the relative motion of the substrate atoms because this technique emphasizes forward scattering.

Once, not so long ago, an ARPEFS experiment might require upwards of 12 hours to collect the data along one emission direction. Things have changed considerablely, as the Mn/Cu(001) and Mn/Ni(001) studies show. Now a full ARPEFS data set takes only half an hour. With the drastically increased data rates, one can consider reproduciblity of the data a necessity, instead of a luxury as in the past. A complete ARPEFS should, in the future, repeat, at least once if not twice, each emission direction so as to increase one's confidence in the data set. Also, k-space point density finer than the 0.1 $\AA^{-1}$ step size that is now typical, should be a goal of the new ARPEFS experiments with such large data rates.

Lastly, one must think about the symmetry of the sample when deciding upon the experimental geometry. The tungsten oxide study is illustrative. We chose the light polarization $\mathcal{E}$ vector and the off-normal emission direction to lie along the <001> azimuth to take advantage of the surface symmetry. Otherwise, the scattering simulation code would require averaging of two different geometries because the tungsten atoms at either end of the long axis of the unit cell would be in different scattering geometries.

III. The Future

The future for photoelectron holography is bright. With the number of synchrotron light sources increasing world wide, improvements in instrumentation, and improved scattering simulation codes available, photoelectron diffraction should soon be available to non-experts for surface structure determinations. The future also holds a number of exciting new experimental possibilities, two of which are spin-polarized-photoelectron holography, and single domain photoelectron diffraction.

Spin polarized photoelectron diffraction: It should be possible to separately measure the diffraction profiles of spin up and spin down photoelectrons, and thus determine the short-range magnetic order around the emitter. The multiplet splittings in ferromagnetic metals, the Fe 3s line for example) are one source of polarized electrons that are readily available experimentally, because of the difference in binding energies of the spin-up and spin-down components. Additionally, there is the possibility of extracting spin-polarized diffraction curves by combining an electron spin detector with a large-radius, hemispherical electron-energy analyzer and an undulator beamline. Because of the inefficiencies of spin detectors, a tremendous photon flux and a high-throughput analyzer will be needed to accomplish such an experiment.

Single-domain photoelectron diffraction: Under construction at the ALS is a beamline which will have a one μm spot size with photon flux of 3×10^{10} photons per second. The small spot size and large flux are made possible by the small emittance of the electron beam at the ALS storage ring. Such beamline performance will enable one to do a photoelectron diffraction experiment on a single sample domain. This ability would be very exciting for atomic structural studies of magnetic materials where the domain size is typically 10 μm.

...We cut ourselves off, I think, from a source of wisdom. We sometimes mistake a rude life for a rude mind; raw meat for barbarism; lack of conversation for lack of imagination. ...A wisdom is to be found in the people. And once in a great while an *isumataq* becomes apparent, a person who can create the atmosphere in which wisdom shows itself.

This is a timeless wisdom that survives failed human economies. It survives wars. It survives definition. It is a nameless wisdom esteemed by all people. It is understanding how to behave properly toward people and toward the land.

Barry Lopez, Arctic Dreams

APPENDIX A

Gold Polishing

I am including this appendix on polishing gold single crystals not so much because it contains anything new, but because it is so difficult to gather all the "Black Magic" into one place when one wishes to prepare difficult samples. This section will mostly deal with the electropolishing method I learned from Nennad Markinovich. To my knowledge this electropolishing recipe has not been published previously. First I will give some general principles for mechanically polishing gold, which is among the most difficult metal crystals to prepare.

When dealing with gold one must remember that it is extremely soft and that the more pure it is the softer it is. The Mohs hardness for 24 kt gold is 2.5, but single crystals that are 99.999% pure are much softer. This softness dictates every action concerning the crystal preparation and great care must be taken to avoid any mechanical shock to the crystal. The first step is to orient the boule. The boule end is often so damaged as to make it impossible to obtain quality Laue picture. One must first slice of a small portion of the boule to get to expose a single crystal face. Spark cutting is by far the preferred method for cutting soft metals. Cutting the boule with a low speed diamond saw causes a very deep damage layer that must be removed to achieve a single crystal surface. The spark cutting method is very gentle; so gentle in fact, that it is possible to take Laue X-ray backscattering photographs directly from the surface of the spark cut crystal without further preparation.

The boule should be mounted a holder which permits the boule to be oriented and the desired crystal to be spark cut from the same holder. After one has the oriented single crystal slab, one polishes it with the six μm and one μm diamond paste. Never use any abrasive larger than 600 grit sand paper otherwise the resulting damage layer is too deep and requires a very long time to remove. The last mechanical polishing step is with a 0.05 μm CeO_2 slurry in the Vibratron machine. It is important to realized that because gold is so soft one can never remove

all of the surface scratches. In the end one has to trade off scratch removal with pitting. The pitting makes the surface look like an orange peel, and is caused by the polishing grit digging into the surface and rotating within this small area instead of moving across the surface. If pitting occurs one has to go back to much larger grit abrasive and start over.

Once the mechanical polishing steps are complete one has to prepare the crystal for the electropolishing steps. The first step is to affix a large copper wire to the back of the crystal with conducting, silver epoxy. The silver epoxy requires a long time to cure at room temperature, but heating with a heat gun speeds up this process considerably. Care should be taken though not to heat the epoxy too rapidly otherwise it will fail. After the epoxy is cured, I paint the copper wire, the epoxy and the back and sides of the crystal with clear fingernail polish. Several coats of polish are required to achieve a effective insulating layer.

The electropolishing solutions are made from doubly de-ionized (DI) water and then purged for several hours with dry nitrogen to displace as much of the dissolved oxygen as possible. The polishing solution is made form 40 g of KCN and 70 g of KNa-tartarate dissolved in one liter of water. The next step removes CN^- ions from the gold surface. This reducing solution is 1M $HClO_4$, for those non-chemists, 88.2 ml of concentrated acid dissolved in 1 liter of water. In between the two steps the crystal and wire should be washed with copious amounts of DI water. As these polishing steps use cyanide salts and acid in close proximity one must be careful not to mix the acid and cyanide as this will produce gaseous HCN. Needless to say one must do this procedure in a fume hood.

The working electrode in all the polishing steps is the gold crystal. The counter electrode is a gold wire. A 1 mm thick gold wire gasket works well. The current density for the polishing step is, $i = +1.0 - 1.3\ A/cm^2$, depending on the surface quality. One should apply the potential to both electrodes before submerging the crystal any of the solutions. There should be O_2 evolution from the crystal surface once the polishing has started. This gas evolution can be quite vigorous, and may be disturbing at first, but it is normal. This is the step that actually removes the gold metal from the surface of the crystal. One should see the dissolved gold from the crystal plate out on to the counter electrode after a couple of minutes. The polishing step should take five to eight minutes.

After the polishing step wash the crystal very well in deionized water and then apply the voltage before dunking the crystal in the reducing path. This step is intended to remove the leftover CN^- ion. The current density for the reduction step is $i = -0.2\ A/cm^2$. Note that the polarity for this step is opposite that in the polishing step, so there should be H_2 evolution from the gold crystal now. Let the crystal stay in the reduction bath for one to two minutes. Then remove and rinse the crystal with DI water. Table I summarizes the polishing method.

Table I. Summary of gold electropolishing procedure.

Polish		
SOLUTION	CURRENT	TIME
40 g KCN 70 g KNa-tartarate /liter	+ 1.0 - 1.3 A/cm^2	5 to 8 minutes
Reduction		
1 M $HClO_4$	- 0.2 A/cm^2	1 to 2 minutes

If the crystal is destined to be used in UHV where it can be annealed then the process outside vacuum is finished. However to study the crystal without subsequent UHV annealing it is best to anneal it in a H_2 flame.

Remove the crystal from the copper wire by dissolving the conducting epoxy in Methyl Ethyl Ketone. Acetone will also work eventually, but care should be taken not to let the acetone dry on the surface, such a film is nearly impossible to remove without returning to the mechanical polishing steps.

The flame annealing step removes and remaining organics from the surface and allows the surface to relax. After the annealing process the surface is bulk terminated, not the usual 5x20 reconstruction that is seen in after annealing in vacuum. Heat the crystal in the H_2 flame for 5-10 minutes once it has turned a dull orange color. It may be necessary to turn off the lights to see the crystal color. After finishing the annealing process immediately quench the crystal in DI water.

Ernest Orlando Lawrence Berkeley National Laboratory
One Cyclotron Road | Berkeley, California 94720

Prepared for the U.S. Department of Energy under Contract No. DE-AC03-76SF00098